

HARVARD UNIVERSITY  
Graduate School of Arts and Sciences



DISSERTATION ACCEPTANCE CERTIFICATE

The undersigned, appointed by the

Department of Physics

have examined a dissertation entitled

Studies of Strongly Correlated Systems: From First Principles  
Computations to Effective Hamiltonians and Novel Quantum Phases

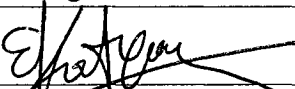
presented by

Ryan Lee Barnett

candidate for the degree of Doctor of Philosophy and hereby  
certify that it is worthy of acceptance.

Signature  \_\_\_\_\_

Typed name: Professor Eugene Demler, Chair \_\_\_\_\_

Signature  \_\_\_\_\_

Typed name: Professor Efthimios Kaxiras \_\_\_\_\_

Signature  \_\_\_\_\_

Typed name: Professor Michael Tinkham \_\_\_\_\_

Date: May 4, 2006



**Studies of strongly correlated systems: from first  
principles computations to effective hamiltonians  
and novel quantum phases**

A dissertation presented

by

Ryan Barnett

to

The Department of Physics

in partial fulfillment of the requirements

for the degree of

Doctor of Philosophy

in the subject of

Physics

Harvard University

Cambridge, Massachusetts

May 2006

UMI Number: 3217673

Copyright 2006 by  
Barnett, Ryan

All rights reserved.

### INFORMATION TO USERS

The quality of this reproduction is dependent upon the quality of the copy submitted. Broken or indistinct print, colored or poor quality illustrations and photographs, print bleed-through, substandard margins, and improper alignment can adversely affect reproduction.

In the unlikely event that the author did not send a complete manuscript and there are missing pages, these will be noted. Also, if unauthorized copyright material had to be removed, a note will indicate the deletion.

**UMI**<sup>®</sup>

---

UMI Microform 3217673

Copyright 2006 by ProQuest Information and Learning Company.

All rights reserved. This microform edition is protected against unauthorized copying under Title 17, United States Code.

ProQuest Information and Learning Company  
300 North Zeeb Road  
P.O. Box 1346  
Ann Arbor, MI 48106-1346

©2006 - Ryan Barnett

All rights reserved.

Thesis advisor

Author

Eugene Demler

Ryan Barnett

**Studies of strongly correlated systems: from first principles  
computations to effective hamiltonians and novel quantum  
phases**

**Abstract**

In this thesis we derive minimal effective hamiltonians from more detailed theories which are used to predict novel quantum phases of solid state and atomic and molecular systems. We consider the solid state systems of transition metal dichalcogenides, strands of stretched poly(CG)-poly(CG) DNA, and carbon nanotubes. The cold atomic and molecular systems we consider are alkali atoms in the  $F = 2$  hyperfine state and dipolar molecules in an optical lattice.

# Contents

Title Page . . . . .	i
Abstract . . . . .	iii
Table of Contents . . . . .	iv
Citations to Previously Published Work . . . . .	vii
Acknowledgments . . . . .	ix
<b>1 Introduction</b>	<b>1</b>
1.1 Outlook: the central challenge . . . . .	1
1.2 Overview of methods used to derive effective hamiltonians . . . . .	7
1.2.1 Density-functional theory . . . . .	7
1.2.2 Scattering lengths in atomic and molecular systems . . . . .	9
1.3 Overview of systems . . . . .	11
1.3.1 Solid state systems . . . . .	11
1.3.2 Atomic and molecular systems . . . . .	18
<b>2 Electronic properties of the 2H transition metal dichalcogenides</b>	<b>26</b>
2.1 Coexistence of gapless excitations and commensurate charge-density wave in the 2H-transition metal dichalcogenides . . . . .	26
2.1.1 Introduction . . . . .	26
2.1.2 Calculating the Wannier functions from first-principles . . . . .	28
2.1.3 Minimal model for the CDW state . . . . .	31
2.1.4 Theoretical ARPES spectra . . . . .	35
2.1.5 Conclusion . . . . .	38
2.1.6 Acknowledgements . . . . .	38
2.2 The temperature dependence of the electronic self-energy . . . . .	39
2.2.1 Introduction . . . . .	39
2.2.2 Simple model . . . . .	40
2.2.3 Realistic Computation . . . . .	43
2.3 Fourier STM analysis . . . . .	47
2.3.1 Formalism . . . . .	47
2.3.2 Results and discussion . . . . .	49

<b>3</b>	<b>Electronic properties of DNA</b>	<b>52</b>
3.1	Introduction . . . . .	52
3.2	Constructing the tight-binding hamiltonian from the maximally localized Wannier states . . . . .	54
3.3	Electronic localization in the presence of disorder . . . . .	60
3.4	Conclusion . . . . .	65
<b>4</b>	<b>Superconductivity and charge-density wave instabilities in carbon nanotubes</b>	<b>66</b>
4.1	Introduction . . . . .	66
4.2	Extraction parameters of the effective Fröhlich hamiltonian from the first principles calculations . . . . .	72
4.2.1	Band structure . . . . .	72
4.2.2	The phonon modes . . . . .	73
4.2.3	The electron-phonon coupling vertices . . . . .	74
4.2.4	Phonon frequencies . . . . .	76
4.3	Results for representative nanotubes . . . . .	80
4.3.1	(5,0) nanotube . . . . .	80
4.3.2	(6,0) nanotube . . . . .	86
4.3.3	(5,5) nanotube . . . . .	88
4.4	Instabilities of the electron-phonon system . . . . .	90
4.4.1	Charge-density wave order . . . . .	90
4.4.2	Superconductivity . . . . .	91
4.5	Role of the Coulomb interaction . . . . .	94
4.5.1	Coulomb interaction potential . . . . .	95
4.5.2	Modification of CDW instability due to Coulomb interaction . . . . .	96
4.5.3	Phonon vertex renormalization through screening . . . . .	98
4.5.4	Modification of superconducting instability due to Coulomb interactions . . . . .	99
4.5.5	Summary of Coulomb effects . . . . .	101
4.6	Discussion . . . . .	102
4.6.1	Comparison to other carbon based materials . . . . .	102
4.6.2	Beyond mean field theory . . . . .	105
4.6.3	Experimental Implications . . . . .	106
4.7	Summary and Conclusions . . . . .	109
4.8	Acknowledgements . . . . .	111
<b>5</b>	<b>Quantum magnetism with dipolar molecules and spin two bosons in an optical lattice</b>	<b>112</b>
5.1	Spin two bosons in an optical lattice . . . . .	112
5.1.1	Hyperfine interaction . . . . .	112
5.1.2	From the two-body scattering interaction to the onsite interaction	113



5.1.3	Effective spin interaction for one boson per site . . . . .	115
5.1.4	Phase diagram . . . . .	115
5.1.5	Characterizing the phases . . . . .	118
5.1.6	The phase diagram with fixed magnetization with quadratic Zeeman splitting . . . . .	120
5.2	Dipolar molecules in an optical lattice . . . . .	124
5.2.1	Introduction . . . . .	124
5.2.2	Hamiltonian definition/discussion . . . . .	126
5.2.3	The Mott Insulating state . . . . .	129
5.2.4	The superfluid state . . . . .	132
5.2.5	Conclusion . . . . .	135
5.2.6	Acknowledgements . . . . .	135
<b>A</b>	<b>Appendices for Chapter 2</b>	<b>136</b>
A.1	The electron-phonon coupling vertices . . . . .	136
A.2	Isotropic Eliashberg equations in 1D . . . . .	138
A.3	Incorporating $q \approx 0$ scattering from acoustic phonons in the Eliashberg equations. . . . .	143
A.4	Limitations of non self-consistent method . . . . .	145
A.5	Derivation of Eq. (4.31) . . . . .	148
	<b>Bibliography</b>	<b>151</b>

# Citations to Previously Published Work

Publications for thesis work relating to particular chapters are as follows:

## Chapter 2:

- R. Barnett, A. Polkovnikov, E. Demler, W. Yin, and W. Ku, “Coexistence of gapless excitations and commensurate charge-density wave in the 2H-transition metal dichalcogenides,” *Phys. Rev. Lett.* **96**, 026406 (2006).

## Chapter 3:

- R. Barnett, A. Turner, P. Maragakis, and E. Kaxiras, “Electronic localization in overstretched DNA,” in preparation.
- P. Maragakis, R. Barnett, E. Kaxiras, M. Elstner, and T. Frauenheim, “Electronic structure of overstretched DNA,” *Phys. Rev. B* **66**, 241104(R) (2002).

## Chapter 4:

- R. Barnett, E. Demler, and E. Kaxiras, “Charge-density wave and superconducting instabilities in ultrasmall-radius carbon nanotubes,” *Solid State Commun.* **135**, 335 (2005).
- R. Barnett, E. Demler, and E. Kaxiras, “Electron-phonon interaction in ultrasmall-radius carbon nanotubes,” *Phys. Rev. B* **71**, 035429 (2005).
- S. B. Cronin, R. Barnett, S. G. Chou, O. Rabin, A. K. Swan, S. Unlu, B. B. Goldberg, M. S. Dresselhaus, and M. Tinkham, “Electrochemical gating of

individual carbon SWNTs observed by transport measurements and resonant confocal micro-raman spectroscopy,” *Appl. Phys. Lett.* **84**, 2052 (2004).

- A. Z. Hartman, M. Jouzi, R. L. Barnett, and J. M. Xu, “Theoretical and experimental studies of carbon nanotube electro-mechanical coupling,” *Phys. Rev. Lett.* **92**, 236804 (2004).

### Chapter 5:

- R. Barnett, A. Turner, and E. Demler, “Novel phases of spin two bosons in an optical lattice,” in preparation.
- R. Barnett, D. Petrov, E. Demler, and M. Lukin, “Quantum magnetism with two-component polar molecules in optical lattices,” *cond-mat/0601302*.

# Acknowledgments

I have many people to thank for making my years of graduate school enjoyable and rewarding.

First, I would like to thank Eugene Demler who has been a truly wonderful thesis advisor and has given me unwavering support over the years. The amount that I have learned from him is difficult to quantify. From the classes that I took from him school to our numerous discussions about research, being his student has been a truly great honor and privilege.

I would also like to thank Efthimios (Tim) Kaxiras who has served as a co-advisor on many of the projects in which I was involved. I also had the privilege to learn solid state physics from him from another point of view. He has always provided me with sound advice and good ideas. I should also mention that I have really enjoyed the true sense of community, support, and friendliness that has been present in his research group over the years.

Other faculty at Harvard and elsewhere that I have greatly benefitted from interacting with are Bertrand Halperin, Wei Ku, Mikhail Lukin, Michael Tinkham, and Jingming Xu.

There have also been many fellow graduate students and post docs that I have had the chance to interact with, learn from, and sometimes collaborate with. Among them are Ehud Altman, Nick Choly, Steve Cronin, Adam Hartman, Adilet Imambekov, Gang Lu, Paul Maragakis, Hatem Mehrez, Dmitry Petrov, Daniel Podolsky, Anatoli Polkovnikov, Jiang Qian, Gil Refael, Ari Turner, Daw-Wei Wang, and Wei-Guo Yin.

I would like to thank my good friends Ania Bleszynski, Bola George, Steve Lin, Scott Nguyen, Ari Turner, and Wesley Wong for keeping me sane. We all met in the

halls of Perkins when we were first year students, and have continued to hang out over the years. I already have many fond memories of things we have done together like drinking beer in bars, having long late-night conversations, and playing basketball.

Finally, for their loving support, I would like to thank my parents, Lee and Mary Ann, and my sister, Annsley. I remember my mother volunteering to help out in my first grade class to keep an eye on me and make sure I was doing ok. My father has provided me with wise, humorous, and often quotable words of wisdom over the years. I am very fortunate to have had the upbringing they provided.

# Chapter 1

## Introduction

### 1.1 Outlook: the central challenge

The central paradigm used to make predictions in this thesis, and, indeed, in condensed matter physics is illustrated in Fig. 1.1. The idea is to start with the general many body hamiltonian which is typically intractable for systems of interest. Thus, instead of trying to directly solve this most general hamiltonian we make approximations to arrive at a minimal effective hamiltonian which has enough information to describe the central physics that we are interested in but not much more. We refer to this as step (a). The next step is to solve (or solve approximately) this effective hamiltonian so that predictions can be made, which we refer to as step (b). Sometimes step (a) is the bottleneck, while at other times it is step (b).

This method is perhaps best understood through a few examples. For the first example, we will take an electron phonon system, described by the Fröhlich hamiltono-

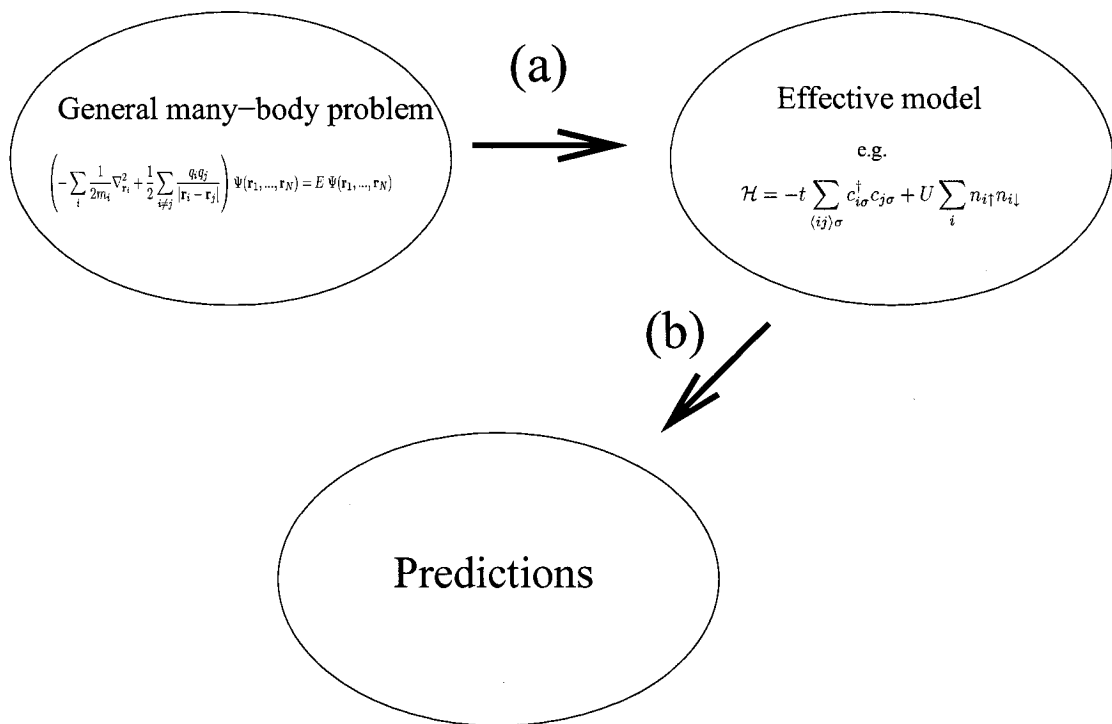


Figure 1.1: The process of starting with the most general many-body hamiltonian which will describe all properties of a solid. Unfortunately it is intractable, so in step (a) simplifying approximations are made to derive an effective hamiltonian having enough detail to explain the desired physics but little more. Then analysis of this effective hamiltonian is performed in step (b) so that predictions can be made.

nian

$$\begin{aligned}
\mathcal{H} = & \sum_{\mathbf{k}\sigma} \varepsilon_{\mathbf{k}} c_{\mathbf{k}\sigma}^\dagger c_{\mathbf{k}\sigma} + \sum_{\mathbf{k}} \Omega_{\mathbf{k}}^0 \left( a_{\mathbf{k}}^\dagger a_{\mathbf{k}} + \frac{1}{2} \right) \\
& + \sum_{\mathbf{k}\mathbf{k}'\sigma} g_{\mathbf{k}\mathbf{k}'} c_{\mathbf{k}\sigma}^\dagger c_{\mathbf{k}'\sigma} (a_{\mathbf{k}-\mathbf{k}'} + a_{\mathbf{k}'-\mathbf{k}}^\dagger) \\
& + \sum_{\mathbf{k}\mathbf{k}'\mathbf{q}\sigma\sigma'} V_{\mathbf{k}\mathbf{k}'} c_{\mathbf{k}+\mathbf{q}\sigma}^\dagger c_{\mathbf{k}'-\mathbf{q}\sigma'}^\dagger c_{\mathbf{k}'\sigma'} c_{\mathbf{k}\sigma}.
\end{aligned} \tag{1.1}$$

This describes a band of electrons created by  $c_{\mathbf{k}\sigma}^\dagger$  coupled to phonons created by  $a_{\mathbf{q}}^\dagger$ . For the sake of illustration here we consider only one electronic band and one phonon mode. Step (a) consists of deriving this model from first principles and coming up with realistic parameters for the hamiltonian Eq. (1.1). A considerable industry in this has been established during the 1980s and 90s [29] motivated by the desire to predict the properties of superconducting materials from first principles. The main tool used is density-functional theory (DFT) which approximately solves the many-body equations within the so-called local-density approximation [122]. The single particle electron quasiparticle energies  $\varepsilon_{\mathbf{k}}$  are typically taken from the metallic band computed using DFT. The energy of the normal phonon modes  $\Omega_{\mathbf{q}}$  can be computed by evaluating the energy difference (again, using DFT total energy calculations) of the equilibrium and distorted lattice structures; the lattice distortions corresponding to the normal phonon modes can typically be obtained from the symmetry of the crystal. The electron phonon coupling vertices  $g_{\mathbf{k}\mathbf{k}'}$  can be computed by using the Kohn-Sham eigenstates  $\psi_{\mathbf{k}}(\mathbf{r})$  to evaluate matrix elements (for more details on this, see Appendix A.1). Finally, coming up with a realistic expression for the Coulomb interaction has proven to be the most difficult aspect of the process. This is partly due to the fact that DFT already includes an amount of the electron-electron interaction (through, for instance, the Hartree term), so writing a term that is not accounted



for in DFT is difficult. Thus, there is a bit of an art to correctly accounting for the Coulomb interaction; we will not go through all of the details here. This completes step (a).

Once we have a reliable Fröhlich hamiltonian, we can perform step (b) to make predictions. An important area where step (b) has been applied is in predicting the transition temperature of “conventional” superconductors (i.e. superconductors described by the BCS theory). The method used here is to derive the so-called Migdal-Eliashberg equations (see, for instance, [3]) which are self-consistent equations in terms of the superconducting gap. The superconducting transition temperature will be the temperature at which a nonvanishing solution for the gap appears. This method has been used over the years to calculate the transition temperature of real materials. One success of the method was the prediction that silicon will become superconducting under pressure [31] which was later verified experimentally. More recently, the method has been applied to the superconducting compound  $\text{MgB}_2$  where the superconducting gap structure was analyzed.

The Fröhlich hamiltonian also can describe the charge-density wave transition (and predict the temperature at which it occurs), which is endemic to one-dimensional systems. We described a method based on the random phase approximation (RPA) in Chapter 4 which we apply to carbon nanotubes.

Our next example has become somewhat dubious in recent years, and is an excellent paradigm of strongly correlated physics where there is competition between kinetic and potential energy. Despite appearing simple, we will see that the two-step process is quite difficult for this case. The Hubbard model on a square lattice is

defined by

$$\mathcal{H} = -t \sum_{\langle ij \rangle \sigma} c_{i\sigma}^\dagger c_{j\sigma} + U \sum_i n_{i\uparrow} n_{i\downarrow} \quad (1.2)$$

where  $c_{i\sigma}$  obey fermionic commutation relations and  $n_{i\sigma} = c_{i\sigma}^\dagger c_{i\sigma}$  is the number operator at site  $i$ . This model has been central to condensed matter physics during recent years, primarily because of its suspected connection with the high temperature cuprate superconductors. We will start with considering step (b). When  $U = 0$ , the ground state is simply a filled Fermi sea of noninteracting electrons. The physics is similar when  $t \gg U$ ; one can perform perturbation theory in  $U/t$ . This will yield electrons that are dressed by a polarization cloud, but, for the most part, they will have similar properties to the original undressed electron. More precisely, it is said that one can adiabatically transform the electron into the quasiparticle without encountering any phase transitions (the essence of Fermi liquid theory). On the other hand, when  $U$  is of the same order as  $t$  or larger, the ground state is not (even qualitatively) known. This regime is referred to as the strongly correlated regime where the perturbation theory in the interaction strength fails. The question of whether or not this Hubbard model has a superconducting ground state in this strongly correlated regime is of central importance and is still not completely resolved. Thus step (b) is quite difficult for the Hubbard model.

On the other hand, perhaps an even more important question is whether or not the Hubbard model is the appropriate minimal model for describing the physics of the high temperature superconductors (step (a)). For instance, suppose that someday someone was able to unambiguously determine that the ground state of the Hubbard model in the strongly correlated regime is a  $d$ -wave superconductor. Then this alone

would not be sufficient to serve as a complete understanding of the superconductivity in these materials. An impetus would certainly follow to more carefully determine if the Hubbard is indeed the correct minimal model to capture the physics of the cuprates. There are many ingredients that the Hubbard model does not contain which are present in these materials. Whether or not these missing ingredients are relevant or not is the central question. For instance, there are three bands at the Fermi energy in the cuprates, while our model only has one. Other quantities present in the material but not explicit in the model are impurities, phonons and electron-phonon interactions, and the long-range Coulomb interaction. On the other hand, including these effects would certainly make our model even less tractable.

There is a growing class of models which exhibit strongly correlated physics thought to be relevant for real materials which are difficult to solve. On the other hand, it is often the case that it is uncertain whether or not these models are correct for describing the material under consideration. This has been a fundamental difficulty (and challenge) in strongly correlated physics.

The burgeoning field of optical lattices has provided new insights into the solution of model hamiltonians, thus helping to resolve this central difficulty in strongly correlated physics. What makes these systems particularly interesting is that step (a) can be carefully, and correctly done. That is, there is little doubt that the effective hamiltonian neglects any important terms. This enables, in principle, direct realization (and solution) of such model hamiltonians in the laboratory.

In Chapters 2, 3, and 4 we consider the *solid state* systems of the transition metal dichalcogenides, DNA, and carbon nanotubes. Crudely speaking steps (a) and (b)

are of similar difficulty in these systems. In Chapters 5 we consider cold atoms and molecules in optical lattices. As said before, there is little doubt that we are dealing with the correct models here, and the impetus is placed on solving the model and predicting novel quantum phases.

## 1.2 Overview of methods used to derive effective hamiltonians

### 1.2.1 Density-functional theory

A starting point that we use in most (Chapters 2,3,4 but not Chapter 5) is the band structure computed from the density-functional theory (DFT). This theory involves the solution of the Kohn-Sham equations [87, 67, 88] which read

$$\left(-\frac{1}{2m}\nabla^2 + V_{\text{ion}}(\mathbf{r}) + V_{\text{H}}(\mathbf{r}) + V_{\text{XC}}(\mathbf{r})\right)\psi_i(\mathbf{r}) = \epsilon_i\psi_i(\mathbf{r}) \quad (1.3)$$

where

$$V_{\text{H}}(\mathbf{r}) = \int d^3r' \frac{n(\mathbf{r}')}{|\mathbf{r} - \mathbf{r}'|} \quad (1.4)$$

is the Hartree potential, and  $V_{\text{XC}}(\mathbf{r})$  is the exchange-correlation potential. The Hartree and exchange-correlation potentials are typically solved self-consistently in terms of the electronic density such that

$$n(\mathbf{r}) = \sum_i |\psi_i(\mathbf{r})|^2 f(\epsilon_i) \quad (1.5)$$

where  $f$  is the Fermi-function. The purpose of the exchange-correlation potential is to capture contributions to the total energy which are not accounted for in the

Hartree approximation. The most common way to describe such a term is through the so-called local-density approximation [88] which is typically viewed as the most common source of error in the method. More details of the Kohn-Sham equations and density-functional theory are contained in the review article [122] and the book by Kaxiras [84].

Density-functional theory has been wildly successful in accurately describing the properties of conventional (i.e. not strongly correlated) solids. In addition, there has been a recent push to capture the behavior of strongly correlated systems using extensions of the conventional DFT methods. One ambitious extension which accounts for quantum fluctuations is to augment DFT with dynamical mean field theory (DMFT) [51], which is referred to now as DFT+DMFT [89]. It will be very interesting to see how successful this method will prove to be in describing such materials.

The results from density-functional theory have been the starting point for many of the studies in this thesis. A summary of the usage of DFT will now be given. In Chapter 2 we use an all-electron code which uses a plane-wave basis set called Wien 2K [14] to compute the band structure of 2H-TaSe<sub>2</sub>. From this, the Wannier functions centered on a single Ta atom are computed. These Wannier functions are used to compute the magnitude of the hoppings between neighboring atoms. Comparisons of these calculations are made with a simple minimal model throughout. In Chapter 3 a fairly similar approach is used. A method called Density-Functional Tight Binding (DFTB) [47] was used. This uses a tight-binding method, but computes the charge density self consistently. The results of this are used to compute the maximally localized Wannier functions which are located on single bases. As in the previous chapter,

these localized functions are used to compute the hopping between neighboring bases. Finally, in Chapter 4 we use the Naval Research Laboratory Tight-Binding (NRLTB) method [110]. This method is fit to reproduce the more accurate *ab-initio* methods, and has the advantage that it takes relatively little computer time. With NRLTB, we compute the input parameters of the Fröhlich hamiltonian for various carbon nanotubes. This involves computing the band structure, the electron-phonon coupling matrix elements, and the phonon frequencies using the frozen-phonon approximation.

### 1.2.2 Scattering lengths in atomic and molecular systems

The method of obtaining a microscopic hamiltonian for an optical lattice system or a dilute gas of weakly interacting bosons is significantly easier than what we described in the previous section. The crucial ingredient that we need (either from experiment or from detailed quantum mechanical calculations) is the scattering length (see, for instance, the book by Pethick and Smith [125]). Atoms typically interact with a van der Waals interaction which decays as  $1/r^6$ . This is much easier to deal with than the case of the  $1/r$  Coulomb interaction because it is short-ranged. For a sufficiently dilute (the average interparticle spacing being much larger than the scattering length) and weakly interacting gas, the upshot of the method [125] is that the interatomic interaction can be replaced by the point interaction

$$V_{\text{int}}(\mathbf{r} - \mathbf{r}') = \frac{4\pi a}{m} \delta(\mathbf{r} - \mathbf{r}'). \quad (1.6)$$

where  $a$  is the  $s$ -wave scattering length. This form of the interaction makes the effective hamiltonian typically easy to derive from first principles.

In an optical lattice system, standing waves are made by reflecting a set of laser

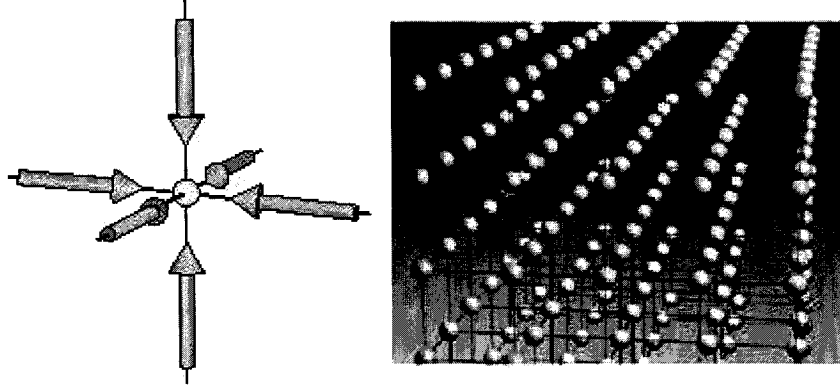


Figure 1.2: A schematic representation of an optical lattice [17].

beams back upon itself. This will give for the lattice interaction

$$V(\mathbf{r}) = V_0 \left( \sin^2(kx) + \sin^2(ky) + \sin^2(kz) \right) \quad (1.7)$$

for the particular example of a square lattice where  $k = 2\pi/\lambda$  is the wave vector of the laser light. For a schematic of the optical lattice, see Fig. 1.2.

With the lattice potential and the atom-atom interaction potential, we are now in a position to derive the microscopic Hamiltonian. We expand the boson field operator in a basis of Wannier states so that

$$\Psi(\mathbf{r}) = \sum_i \phi_i(\mathbf{r}) a_i \quad (1.8)$$

where  $a_i^\dagger$  creates an atom on site  $i$  and  $\phi_i(\mathbf{r})$  is the corresponding localized Wannier state at this site. Then, the noninteracting portion of our many-body hamiltonian is

$$\mathcal{H}_0 = \int d^3r \Psi^\dagger(\mathbf{r}) \left( \frac{-1}{2m} \nabla^2 + V(\mathbf{r}) \right) \Psi(\mathbf{r}) = \epsilon_0 \sum_i a_i^\dagger a_i - J \sum_{\langle ij \rangle} a_i^\dagger a_j \quad (1.9)$$

where  $J$  is the hopping integral between nearest neighbors

$$J = \int d^3r \phi_i^*(\mathbf{r}) \left( \frac{-1}{2m} \nabla^2 + V(\mathbf{r}) \right) \phi_j(\mathbf{r}). \quad (1.10)$$

For the interaction portion of the hamiltonian we get

$$\mathcal{H}_{\text{int}} = \frac{1}{2} \int d^3r d^3r' V_{\text{int}}(\mathbf{r} - \mathbf{r}') \Psi^\dagger(\mathbf{r}) \Psi^\dagger(\mathbf{r}') \Psi(\mathbf{r}') \Psi(\mathbf{r}) = \frac{U}{2} \sum_i n_i (n_i - 1) \quad (1.11)$$

where  $n_i = a_i^\dagger a_i$  and the onsite repulsion is given by

$$U = \frac{4\pi a}{m} \int d^3r |\phi(\mathbf{r})|^4. \quad (1.12)$$

Thus, we have constructed the Bose Hubbard hamiltonian

$$\mathcal{H}_{\text{BH}} = -J \sum_{\langle ij \rangle} a_i^\dagger a_j + \frac{U}{2} \sum_i n_i (n_i - 1) \quad (1.13)$$

(note we have dropped the unimportant term containing  $\epsilon_0$  which can be absorbed into the chemical potential). Moreover, we have essentially exact expression for  $J$  and  $U$  in terms of known quantities. We remark that the above procedure is straightforward to generalize to more complicated systems of, for instance, molecules in an optical lattice and multicomponent atoms (see Chapter 5), and mixtures of atomic species [5].

## 1.3 Overview of systems

Now an overview will be provided of the systems studied in this thesis within the general framework discussed in the previous sections.

### 1.3.1 Solid state systems

The first three systems are solid state systems where we study correlated electrons. To derive the effective hamiltonians in each case we use DFT-based methods.



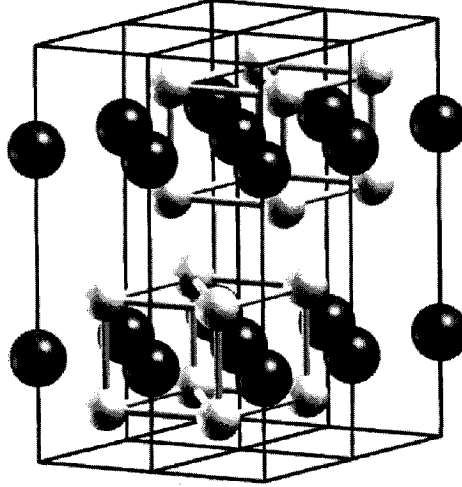


Figure 1.3: The lattice structure of 2H-TaSe<sub>2</sub>. The dark spheres correspond to Ta atoms while the light spheres correspond to the Se atoms [79].

### Transition metal dichalcogenides

The 2H transition metal dichalcogenides (TMDs) were one of the first materials shown to exhibit a charge-density wave transition at sufficiently low temperatures [166]. Examples of these materials are NbSe<sub>2</sub> and TaSe<sub>2</sub>, and the lattice structure is shown in Fig. 1.3. As can be seen, these materials consist of layers containing a triangular lattice of transition metal atoms sandwiched between two layers triangular lattices of chalcogen atoms.

The basic chemistry of these materials is as follows. Four of the valence electrons of the transition metal atoms (Ta or Nb) are transferred to the chalcogen layers, giving two extra electrons per chalcogen atom, filling their  $p$  shell. This then leaves one electron per transition metal atom of approximately  $d_{z^2}$  character which forms

the metallic band. Indeed, detailed DFT calculations reveal that the band(s) at the Fermi energy primarily have  $d_{z^2}$  symmetry.

Many of the properties of the transition metal dichalcogenides have defied simple explanation over the years. For instance, in the original CDW work [166], no sharp increase in the resistivity was found as the temperature was lowered through the CDW transition, which is what one typically finds for the typical CDW materials. Instead, the resistivity seems to decrease, and the presence of the CDW was revealed through electron diffraction studies.

Later high precision ARPES measurements were used to map out the Fermi surface of the TMDs [172, 100, 147, 101, 154, 158, 133, 157]. These reveal a hexagonal Fermi surface centered at  $\Gamma$  which seems to be well nested. Moreover, the nesting vectors seem to correspond to the direction and period of the charge-density wave distortion. However, from these ARPES measurements in the CDW state, there was no clear evidence for a gap opening on this Fermi surface, which is not what one would expect from the standard CDW picture.

Another strange feature seen in recent ARPES measurements [158] is found from extracting the electronic self-energy. In TaSe<sub>2</sub>, kinks in the electron quasiparticle dispersions close to the Fermi energy were observed, which is a typical effect from the electrons coupling to some bosonic mode. Interestingly, these kinks shift further away from the Fermi energy as the temperature is lowered, where the magnitude of the shift is too large to be explained by phonons alone, suggesting perhaps some more exotic bosonic coupling.

In Chapter 2 we attempt to provide an explanation to these two puzzles in the

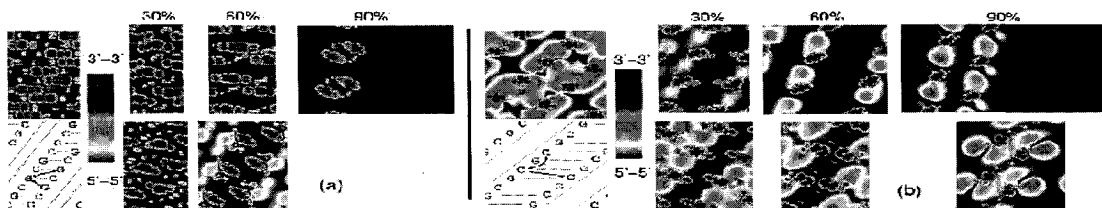


Figure 1.4: Cylindrical contour map of the highest valence (a) and the lowest conduction (b) band electron density, for the poly(CG)·poly(CG) DNA (top left) and the 30%, 60%, and 90% overstretched forms (right). The bottom left panel of each figure shows a drawing of the CG base pairs along the cylinder; the arrows indicate bases with the largest couplings. In Fig. (a) the 90 % overstretched 5'-5' form is not shown because the highest valence band mixes with the lower bands. The vertical axis covers a fixed region corresponding to 10 base pairs in the unstretched form. The horizontal axis runs from 0 to  $2\pi$ . The radius of the cylinder follows the guanine C5 atom in (a), and the cytosine C6 in Fig. (b). The cylinder surface unit element is kept fixed: this results in a variation of the length of the horizontal axis, proportional to the cylinder radius. The color coding (shown in the color bar between the unstretched and stretched graphs) is fixed between different structures and covers 5 orders of magnitude [106].

TMDs. To do this, we use detailed DFT calculations to motivate a minimal model which is then used to study these effects.

## DNA

Chapter 3 deals with the electronic properties of DNA. It has been over half a century since Watson and Crick deduced the atomic structure of DNA [163]. Recently, there has been a significant drive towards characterizing the electronic structure which is motivated on both biological and technological fronts (for a recent review of these endeavours, see [48]).

Only recently have detailed quantum mechanical calculations (e.g. density-functional theory) been able to be performed on a strand of DNA containing several base pairs, which are composed of hundreds of atoms [48]. It is intriguing that these calculations

reveal that the states closest to the Fermi energy (and therefore most relevant from an electronic point of view) reside precisely on the bases (see Fig. 1.4). More specifically, the valence states (just below the Fermi energy) reside on the purine bases (Adenine and Guanine) while the conduction states (just above the Fermi energy) reside on the pyrimidine bases (Cytosine and Thiamine). This gives the promise of sequencing DNA by purely electronic means [26].

In our study, the electronic structure of poly(CG)-poly(CG) DNA which is stretched up to 90% of its natural length is computed. Based on these results, we argue that such stretching plays an important role in electronic transport experiments [106] which are typically performed on a substrate. Next, we take the results from the detailed calculations and derive accurately parameterized tight-binding models for different stretching magnitudes. With these, we show that as the molecule is stretched, the electronic states which were originally delocalized across thousands of base pairs become localized with a modest amount of disorder (in line with that of the dipole moment of stray water molecules attached to the backbone).

### **Carbon nanotubes**

Since their discovery in 1991 by Ijima [72], carbon nanotubes have received continual attention. In addition to having much promise for technological applications, carbon nanotubes are also interesting to study from the purely physical point of view. For instance, they constitute a clean one-dimensional electron system. Therefore, the concomitant physics of Luttinger liquids is expected to arise [52]. Additionally, electron-phonon coupling in one dimensional systems typically will lead to the charge-

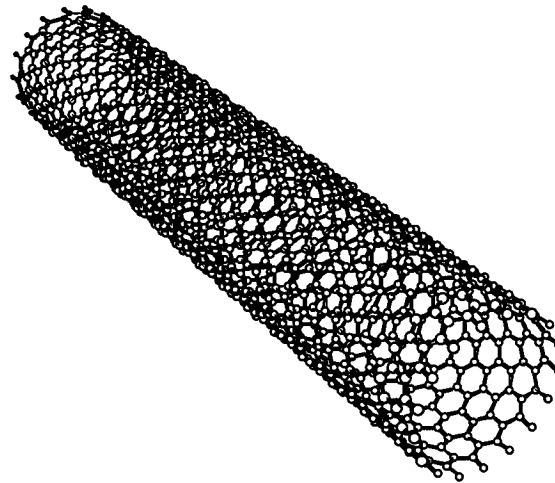


Figure 1.5: The lattice structure of a typical carbon nanotube.

density wave state [61].

Carbon nanotubes have the geometry of a rolled up sheet of graphene (see Fig. 1.5). To understand the electronic band structure of a carbon nanotube, it is often sufficient to start with that of a single sheet of graphene. A carbon atom has six electrons. Two of these electrons occupy the  $1s$  state and are unimportant as far as the bonding properties are concerned, leaving four electrons in the outer shell.

The atomic structure of a sheet of graphene is given by the lattice vectors

$$\mathbf{a}_1 = \frac{\sqrt{3}}{2}\hat{\mathbf{x}} + \frac{1}{2}\hat{\mathbf{y}} \quad ; \quad \mathbf{a}_2 = \frac{\sqrt{3}}{2}\hat{\mathbf{x}} - \frac{1}{2}\hat{\mathbf{y}} \quad (1.14)$$

and basis vector

$$\mathbf{t} = \frac{1}{2}\hat{\mathbf{x}}. \quad (1.15)$$

With this hexagonal lattice, every atom has four nearest neighbors. Three of the electrons in this outer shell will form  $sp_2$  bonds with the neighboring atoms, leaving one electron per carbon atom which is in the  $p_z$  state. Thus as a first approximation,

we should be able to describe the metallic band in graphene by using a tight-binding model on a hexagonal lattice at half filling. Doing this, keeping only nearest-neighbor hopping, we find

$$\epsilon_{\mathbf{k}}^{\pm} = \pm t |1 + e^{i\mathbf{k}\cdot\mathbf{a}_1} + e^{i\mathbf{k}\cdot\mathbf{a}_2}| \quad (1.16)$$

where we have set the Fermi energy equal to zero. From this, one sees why graphene is considered to be a semimetal; from Eq. (1.16) we see that there is zero band gap, but also zero density of states at the Fermi energy.

The reciprocal lattice vectors of Eq. (1.14) are given by

$$\mathbf{b}_1 = 2\pi \left( \frac{1}{\sqrt{3}} \hat{\mathbf{x}} + \hat{\mathbf{y}} \right) \quad ; \quad \mathbf{b}_2 = 2\pi \left( \frac{1}{\sqrt{3}} \hat{\mathbf{x}} - \hat{\mathbf{y}} \right). \quad (1.17)$$

The first Brillouin zone will correspond to a hexagon that has corners at  $\pm \frac{\mathbf{b}_1 - \mathbf{b}_2}{3}$ ,  $\pm \frac{2\mathbf{b}_1 + \mathbf{b}_2}{3}$ , and  $\pm \frac{\mathbf{b}_1 + 2\mathbf{b}_2}{3}$ . These corners are the so-called  $K$ -points and correspond to where  $\epsilon_{\mathbf{k}}^{\pm} = 0$ . Expanding about one of these points, we find that

$$\epsilon_{\mathbf{k}}^{\pm} = \pm t \frac{\sqrt{3}}{2} |\mathbf{k}|, \quad (1.18)$$

the so-called Dirac cone.

The vector  $\mathbf{C} = n\mathbf{a}_1 + m\mathbf{a}_2$  defines the axis about which the nanotube is rolled. This will place a periodicity condition on the wave vectors in the band structure of graphene:  $\mathbf{k} \cdot \mathbf{C}$  must be an integer multiple of  $2\pi$ . Requiring  $\mathbf{k}$  to be at one of the  $K$  points of the first Brillouin zone, we find that  $\mathbf{K} \cdot \mathbf{C}$  being an integer multiple of  $2\pi$  is equivalent to  $n - m$  being divisible by 3. Thus, according to this, a nanotube is metallic if and only if  $(n - m)/3$  is an integer.

Obtaining the band structure of a nanotube from the band structure of graphene in such a way is known as the zone-folding method [135]. It has one obvious drawback: it

does not take into account the curvature effects of the nanotube since it uses the band structure of graphene. It turns out that such a method works well for nanotubes of sufficiently large diameter, but eventually breaks down. That is, eventually curvature will make the  $sp_2$  bonds mix with the  $p_z$  states, which of course is not taken into account in our simple model.

Chapter 4 largely deals with nanotubes for which the zone-folding method breaks down. This study is motivated by observations of superconductivity in such small-radius nanotubes. Experimentally, superconductivity was found in ropes of single-walled nanotubes [86], small-radius nanotubes embedded in a zeolite matrix [152], and multiwall carbon nanotubes [151]. Small-radius nanotubes have significantly enhanced electron-phonon coupling strengths. This will raise the charge-density wave and superconducting transition temperatures to observable temperatures as we will argue in Chapter 4.

### 1.3.2 Atomic and molecular systems

#### Background

After two decades of developing the technology of trapping and cooling alkali atoms by lasers, Bose-Einstein condensation was achieved in 1995 first in Rb [6], and soon after in Na [33] and Li [10]. This added to superfluid helium and superconducting metals another interesting system exhibiting macroscopic occupation of a single quantum state.

On the other hand, since the standard BEC of alkali atoms are dilute and *weakly interacting*, developing a theory to describe the quantum state of the condensate

turns out not to be particularly demanding. More specifically, using the Gross-Pitaevskii equation [126, 60] has proved to be very successful in describing the ground state properties as well as the dynamics in the condensed state. The only two important parameters to make such predictions are the  $s$ -wave scattering length and the atomic mass. Moreover, quantum corrections not taken into account in the Gross-Pitaevskii equation can be accounted for by using the Bogoliubov theory [18].

Within recent years, cold atomic systems have entered the *strongly interacting* regime with the advent of optical lattices. Being theoretically discussed in 1998 [77], such systems were realized in 2002 [57]. Using optical lattices, many topics in strongly correlated physics are now being explored. We should also remark that another route to strong interactions in an atomic system is through the use of a Feshbach resonance [125] which allows the scattering lengths to be controllably tuned with the use of an external magnetic field. When the magnetic field is tuned close to the resonance the scattering lengths can be made to be quite large having either positive or negative sign.

Examples of strongly interacting physics in atomic systems studied with the use of an optical lattice and/or a Feshbach resonance are becoming numerous. Some examples are (the references are not comprehensive) quasi one-dimensional physics [120, 85], the insulator-superfluid transition [57], pairing in imbalanced populations of atoms [175, 121], and the BEC-BCS crossover [131].

Now it is appropriate to give a short overview of the Bose Hubbard model which exhibits the insulator-superfluid transition, since it is essential background for Chapter 5. For convenience, we reproduce the model derived in the previous section 1.2.2,



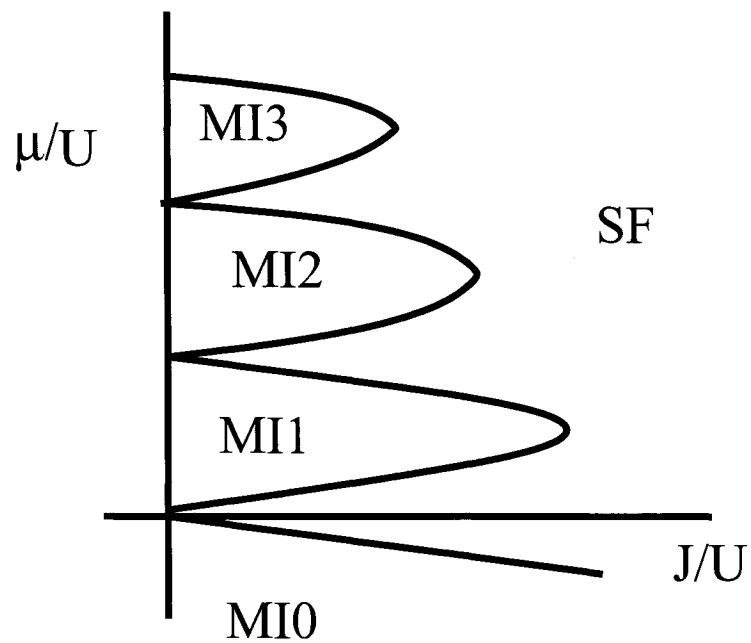


Figure 1.6: The phase diagram of the Bose Hubbard model.  $MI1$ ,  $MI2$ , ... correspond to the Mott insulating states with 1,2, ... bosons per site. In the MI state we have  $\langle a \rangle = 0$  while in the superfluid state (SF) we have  $\langle a \rangle \neq 0$ .

and include a chemical potential term

$$\mathcal{H}_{\text{BH}} = -J \sum_{\langle ij \rangle} a_i^\dagger a_j + \frac{U}{2} \sum_i n_i(n_i - 1) - \mu \sum_i n_i \quad (1.19)$$

which is the Bose Hubbard model for spinless bosons. This model is amenable to a mean field treatment applied to the hopping term. Assuming translational invariance, this leads to the single site mean field hamiltonian

$$\mathcal{H}_{\text{MF}} = -J \left( a^\dagger \langle a \rangle + \langle a^\dagger \rangle a - \langle a^\dagger \rangle \langle a \rangle \right) + \frac{U}{2} n(n - 1) - \mu n. \quad (1.20)$$

This equation then needs to be solved self-consistently in terms of  $\langle a \rangle$ . One method to do this is through numerical iteration. The resulting phase diagram is shown in Fig. 1.6. It is seen that large regions of the phase diagrams are pinned at an integer number of bosons per site (labeled MI1, MI2, ...). In these regions, we have  $\langle a \rangle = 0$ . The superfluid state (labeled SF), on the other hand, has  $\langle a \rangle \neq 0$ .

It should also be pointed out that the Bose Hubbard model has an exact solution in one dimension for hard core bosons (i.e. when  $U = \infty$ ). In this regime, the bosons behave exactly like fermions, and through a series of transformations, the Bose Hubbard hamiltonian can be mapped to the simple tight-binding model for fermions in one dimension

$$\mathcal{H}_{\text{tb}} = \sum_k (-2t \cos(k) - \mu) c_k^\dagger c_k \quad (1.21)$$

which, of course, can be solved exactly. Here, the filled band  $\mu > 2t$  corresponds to the vacuum state, the empty band  $\mu < -2t$  corresponds to the Mott insulating state with one boson per site, while the partially filled band  $-2t < \mu < 2t$  corresponds to the SF state.

## Multicomponent atoms and molecules in optical lattices

Chapter 5 will be devoted to considering how the simple phase diagram of the Bose Hubbard model shown in Fig. 1.6 will be modified for multicomponent systems.

### *Spin two bosons*

We first consider spin two bosons in an optical lattice which corresponds to a hyperfine state of an alkali atom (having nuclear spin  $I = 3/2$  and electronic spin  $S = 1/2$ ). When considering scattering between two such atoms, we have to consider three different scattering lengths ( $a_0$ ,  $a_2$ , and  $a_4$ ) because the two atoms can combine to be in a state with total spin 0, 2, or 4 (odd spins are not allowed because the wavefunction of the two particles must be symmetrical under interchange of particles).

This will modify the onsite Hubbard interaction to read

$$\mathcal{H}_U = \frac{1}{2}U_0n(n-1) + \frac{1}{2}U_1\mathcal{P}_0 + \frac{1}{2}U_2(F^2 - 6n) \quad (1.22)$$

where  $\mathcal{P}_0$  is the projection operator into the spin zero state. The onsite interaction parameters are given by  $U_0 = \frac{\alpha}{7}(4a_2 + 3a_4)$ ,  $U_1 = \frac{\alpha}{7}(7a_0 - 10a_2 + 3a_4)$ , and  $U_2 = \frac{\alpha}{7}(a_4 - a_2)$  where  $\alpha$  is a constant depending on the shape of the onsite Wannier functions. Note that when the scattering lengths are all equal, we will have  $U_1 = U_2 = 0$ , and our system is described by the spinless hamiltonian.

Now we consider the example of one boson per site in the Mott insulating state. Deep in the Mott insulating state, when there is no hopping between adjacent sites ( $J = 0$ ) there will be a macroscopic degeneracy where the effective spins on any site can point in any direction. Turning on finite  $J$  will remove this degeneracy by the second order process of virtual hopping. First we consider the case of equal

scattering lengths where  $U_1 = U_2 = 0$ . It can be seen that such an interaction favors the ferromagnetic state

$$\psi = \prod_i \left( \sum_{\alpha=-2}^2 A_\alpha |\alpha\rangle \right) \quad (1.23)$$

where  $|\alpha\rangle$  are the eigenkets of  $F_z$ :  $F_z |\alpha\rangle = \alpha |\alpha\rangle$  and the coefficients are normalized  $\sum_\alpha A_\alpha^* A_\alpha = 1$ . Despite removing the original macroscopic degeneracy, there is still a fairly large degeneracy: the 8 free parameters from the  $A_\alpha$  coefficients (10 real numbers minus one normalization condition and an overall phase factor). We will show in the first part of Chapter 5 that with finite  $U_1$  and  $U_2$  this latter degeneracy will be lifted in interesting ways.

### *Dipolar molecules*

Another system which exhibits interesting spin ordering are dipolar molecules in an optical lattice. Two classical dipoles  $\mathbf{d}_1$  and  $\mathbf{d}_2$  at positions  $\mathbf{r}_1$  and  $\mathbf{r}_2$  will interact through the anisotropic potential

$$V(\mathbf{r}_1, \mathbf{r}_2) = \frac{\mathbf{d}_1 \cdot \mathbf{d}_2}{|\mathbf{r}_1 - \mathbf{r}_2|^3} - 3 \frac{\mathbf{d}_1 \cdot (\mathbf{r}_1 - \mathbf{r}_2) \mathbf{d}_2 \cdot (\mathbf{r}_1 - \mathbf{r}_2)}{|\mathbf{r}_1 - \mathbf{r}_2|^5}. \quad (1.24)$$

On the other hand, for quantum molecules the situation will not be quite so simple. That is, a dipolar molecule in any particular rotational eigenstate will always have average dipole moment of zero:  $\langle \mathbf{d} \rangle = 0$ . Such molecules will therefore not interact as in Eq. (1.24).

One method to induce dipolar interactions between molecules is to use a strong external electric field, which will align all of the molecules to point along a common axis. The resulting ordering for a gas of cold molecules has been considered in the literature [169, 137, 37, 56, 117, 111].

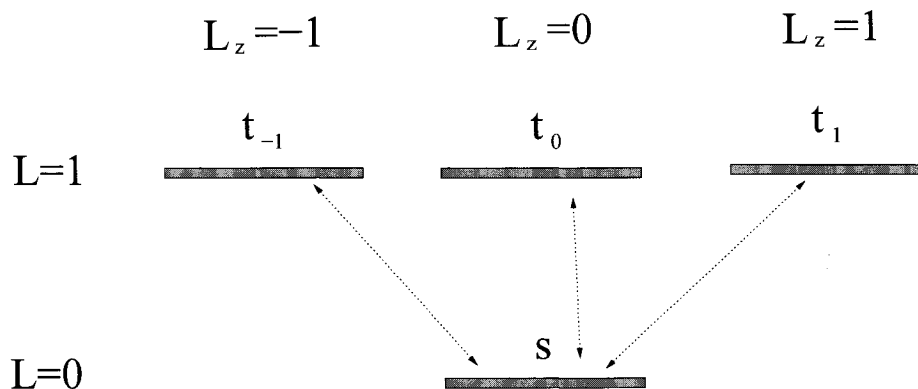


Figure 1.7: The lowest rotational levels of a diatomic molecule.

In this work, we consider an alternative mechanism which is shown schematically in Fig. 1.7. The idea is to create a mixture of molecules in the  $L = 0$  and  $L = 1$  states by controlling the relative populations with an external microwave field. We use the notation that  $s^\dagger$  creates a molecule in the  $L = 0, L_z = 0$  state while  $t_{-1,0,1}^\dagger$  creates molecules in the  $L = 1, L_z = -1, 0, 1$  states. Then taking the following linear combinations

$$t_x^\dagger = \frac{1}{\sqrt{2}} (t_1^\dagger + t_{-1}^\dagger) \quad ; \quad t_y^\dagger = \frac{1}{i\sqrt{2}} (t_1^\dagger - t_{-1}^\dagger) \quad ; \quad t_z = t_0 \quad (1.25)$$

allows us to write the dipole moment operators within this subspace as

$$d_\alpha = s^\dagger t_\alpha + t_\alpha^\dagger s \quad (1.26)$$

where  $\alpha = x, y$ , or  $z$ . Note that, as stated before, states that are rotational eigenstates give  $\langle d \rangle = 0$ . On the other hand, states that are formed from superpositions of the  $s$  and  $t$  operators such as  $|\psi\rangle = \frac{1}{\sqrt{2}}(s^\dagger + t_x^\dagger)|0\rangle$  will have nonzero dipole moment.

Our expression for the dipole moment operators 1.26 can now be inserted into Eq. (1.24). This gives an extra term in to our original Bose Hubbard model. The

resulting dipolar ordering will be discussed in the latter portion of Chapter 5.

# Chapter 2

## Electronic properties of the 2H transition metal dichalcogenides

### 2.1 Coexistence of gapless excitations and com- mensurate charge-density wave in the 2H-transition metal dichalcogenides

#### 2.1.1 Introduction

Charge-density waves (CDWs) in solids has been a topic of central interest in condensed matter physics for many years [61]. Recent scanning tunneling microscopy experiments showing a periodic modulation in the local density of states in cuprate superconductors [68], has reinvigorated such interest. Despite being one of the earliest discovered class of materials which exhibit a CDW at low temperatures (for a

review, see [165]), many properties of the 2H-transition metal dichalcogenides (2H-TMDs) are still not understood, leading to much recent theoretical [132, 25, 156] and experimental [172, 100, 147, 101, 154, 158, 133, 157] research effort (for a review, see Ref. [[167]]). Two key issues concerning the CDW phase in these materials deserve the most attention. First, controversy exists between different experimental groups on the driving mechanism of CDW originating from quantitative differences between the angle-resolved photoemission spectroscopy (ARPES) data. While some experimental results [100, 147, 101, 154] suggest that the hexagonal Fermi surfaces around the  $\Gamma$  point are consistent with the CDW nesting vector, others [158, 133, 157] indicate that this Fermi surface is too large to give the correct nesting vector. Second, and of a more qualitative nature, ARPES measurements [100, 147, 101, 154, 158, 133, 157] find no evidence of a gap opening on the hexagonal Fermi surface, in direct contrast with traditional wisdom of CDW materials.

Here, we focus on the latter issue and suggest a simple picture for why such gapless excitations are permitted in the CDW phase. Using density-functional theory, the electronic structure of prototype 2H-TMD, 2H-TaSe<sub>2</sub>, is analyzed with a newly developed Wannier function approach [91, 58], and a striking feature is revealed: the low-energy bands near Fermi surfaces, which governs the physics of CDW, is dominated by hopping between second-nearest neighbors. This special nature of hopping, in combination with the triangular lattice vectors, effectively splits the system into three weakly coupled triangular sublattices. Since the CDW state gives distortion of only two of the sublattices, whose stability is illustrated with a simple model, such unique electronic structure naturally leaves the bands associated with the undistorted



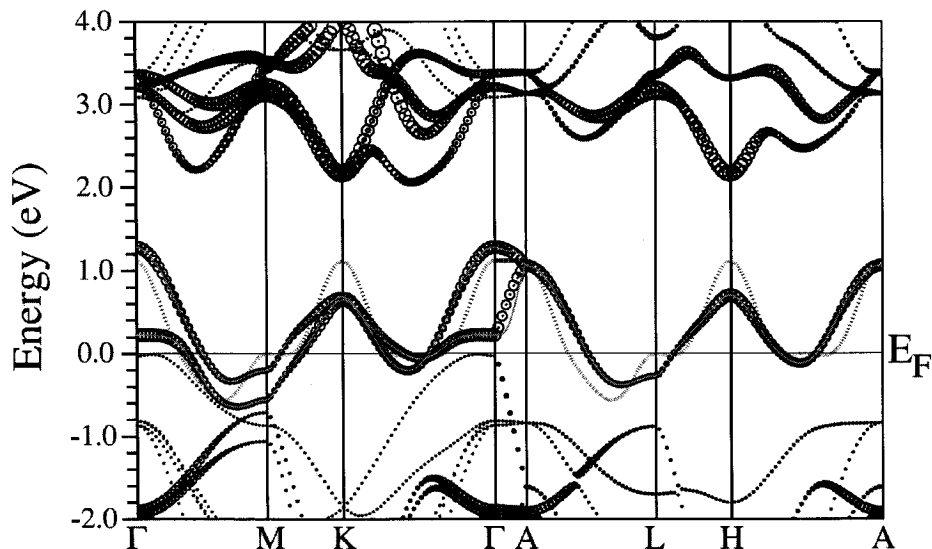


Figure 2.1: First-principles band structure (dots) with the  $d_{z^2}$  (black circles) and  $d_{xy}/d_{x^2-y^2}$  (blue circles) characters shown. The bands below  $-0.7$  eV are mainly Se  $p$  bands. Also shown are the bands constructed from low-energy WFs (green solid lines) and a 2D ‘nesting’ model (red dotted line; see text).

sublattice ungapped in this CDW phase, resolving the puzzle of the observed gapless excitations along the nested regions of the Fermi surface.

### 2.1.2 Calculating the Wannier functions from first-principles

The lattice structure of 2H-TMDs consists of stacked layers of 2D-triangular lattices of transition metals (e.g. Ta or Nb) sandwiched between layers of chalcogen atoms (e.g. S or Se). Rough estimation of the ionization leads to the  $\text{Ta}^{4+}\text{Se}^{2-}$  configuration with one valence  $5d_{z^2}$  electron left per Ta atom that forms the metallic bands at the Fermi level. We applied the WIEN2k [15] implementation of the full potential linearized augmented plane wave method in the local density approximation of density functional theory with the crystallographic data [115]. The basis size was determined by  $R_{mt}K_{max} = 7$  and the Brillouin zone was sampled with a regu-

lar mesh containing 99 irreducible  $k$ -points to achieve energy convergency of 1 meV. The band structure from our first-principles calculations (see Fig. 2.1) shows a strong  $d_{z^2}$  character in the two metallic bands corresponding to two weakly coupled TaSe<sub>2</sub> sandwiches per unit cell. Unexpectedly, little Se  $p$  characters are found in these two bands. The calculated low-energy bands agree well with experiments, except that the saddle bands on the  $\Gamma K$  and AH lines are not as flat and close to the Fermi level as reported [100, 101].

Based on the first-principles ground state, the low-energy Hilbert space can be accurately extracted via local WFs (see Fig. 2.2), which we constructed by extending recently developed energy-resolved method [91, 58] to incorporate desired symmetry [90]. As expected, the WF located at each Ta site has strong  $d_{z^2}$  symmetry near the center, before extending its unusual tails of  $d_{xy}/d_{x^2-y^2}$  symmetry to the nearest neighboring Ta sites due to strong hybridization with the  $d_{xy}/d_{x^2-y^2}$  orbitals near the  $K$  and  $H$  points (see Fig. 2.1). This particular shape of the WF results in an intriguing feature in the hopping integral (evaluated via  $t_{\mu\nu} = \langle \mu | h^{DFT} | \nu \rangle$  with density functional theory Hamiltonian,  $h^{DFT}$ , and Wannier states  $|\mu\rangle$  and  $|\nu\rangle$ ). That is, the second neighbor hopping,  $t_2 = 115$  meV, overwhelms the first neighbor hopping,  $t_1 = 38$  meV, due to remarkable phase cancelation in the latter case (to be discussed in more detail below). In addition, interlayer hoppings are found to be comparable to first-neighbor in-plane hopping with  $t_{\perp,1} = 29$  meV and  $t_{\perp,2} = 23$  meV.

A simple microscopic picture for the unexpected dominance of second-neighbor hopping can be obtained from the symmetry of the WFs. As shown in Fig. 2.2(c) and (d), the contributions to the hopping parameters between neighboring WFs come

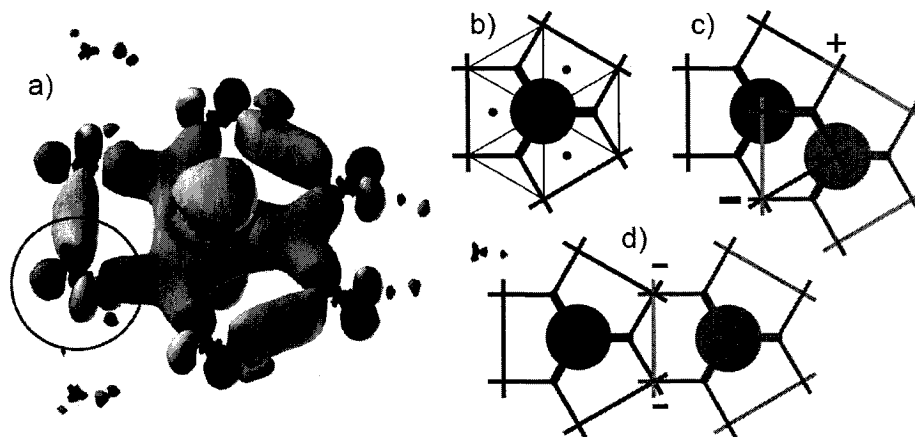


Figure 2.2: Low-energy WF centered at Ta sites with  $a_g$  ( $d_{z^2}$ ) symmetry, colored to show its gradient from positive (red) to negative (blue). Notice the local  $d_{xy}/d_{x^2-y^2}$  symmetry in the hybridization tail (circled) located at neighboring Ta sites. b) Schematics of the WF in the layer of the Ta triangular lattice, with a similar color scheme giving the sign of the WF and three small dots marking the positions of Se atoms in the next layer. c) and d) Schematics of phase interference in hopping to first and second nearest neighbors, respectively.

mainly from overlap of their hybridization tails, since the tail-center ( $d_{z^2} - d_{xy}/d_{x^2-y^2}$ ) overlap gives negligible contribution due to its odd parity. While the first-neighbor hopping suffers seriously from the phase cancellation (illustrated by the *opposite* sign in Fig. 2.2(c)), the second-neighbor hopping benefits greatly from the phase coherence (the same sign in Fig. 2.2(d)) of the overlap. Such symmetry consideration should hold for all 2H-TMDs of the same class, due to their similar local environment around the transition metal sites.

Specifically in 2H-TaSe<sub>2</sub>, this unusual electronic structure provides a plausible intuitive resolution to the puzzling experimental observation of gapless excitations in the CDW phase. Indeed, with the dominating second neighbor hopping in a triangular lattice, the system effectively splits into *three* weakly coupled sublattices. As we discuss below, one of the sublattices remains undistorted in the CDW phase

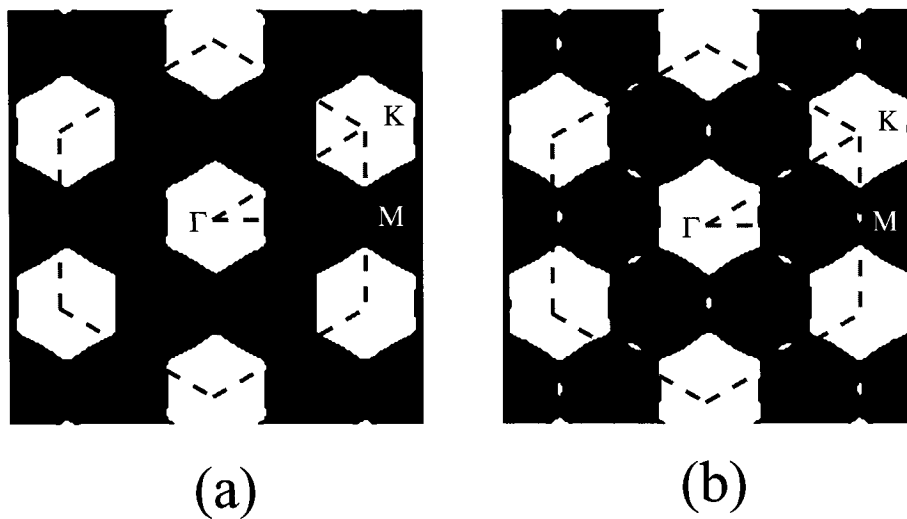


Figure 2.3: (a) The Fermi surface from the tight-binding band structure. White indicates unoccupied states and black indicates occupied states. (b) The Fermi surface for a slightly smaller chemical potential showing the extended saddle bands (small white regions). The first Brillouin zone is the hexagonal cell formed by the red dashed lines.

(see Fig. 2.4) and therefore the bands associated with it are ungapped.

### 2.1.3 Minimal model for the CDW state

With the dominance of the second neighbor hopping established, we now move on to construct a minimal , nesting model which captures the essential physics of the gapless CDW in 2H-TMDs. We start with the simple 2D tight-binding energies given by

$$\varepsilon_{\mathbf{k}}^0 = \sum_{\mathbf{R}} t_{|\mathbf{R}|} \cos(\mathbf{k} \cdot \mathbf{R}) \quad (2.1)$$

where  $\mathbf{R}$  runs over the triangular lattice defined by lattice vectors  $\mathbf{a}_1 = a(\sqrt{3}/2, 1/2)$  and  $\mathbf{a}_2 = a(\sqrt{3}/2, -1/2)$ . In addition to  $t_2$ ,  $t_6 = t_2/3$  (all other hoppings neglected) is introduced to produce the Fermi surface of an almost perfectly nested “hexagonal

checkerboard” pattern similar to the recent ARPES data with extended saddle bands (very close to but below the Fermi energy for extended regions along  $\Gamma K$ ) [100, 147, 101, 154], as shown in Fig. 2.3. The corresponding band (with  $t_2$  adjusted to 140 meV) compares reasonably well with the first principles results (see Fig. 2.1; the two metallic bands are degenerate in the 2D model). As we show below, even with such a perfect Fermi surface nesting, no gap is opened upon the formation of CDW.

Continuing the development of our minimal model, we next consider the CDW lattice distortions. The detailed neutron diffraction experiments of Moncton *et al.* [115] have determined that the ionic displacements have  $\Sigma_1$  symmetry, which corresponds to longitudinal motion of the Ta atoms in the basal plane with amplitude given by experiment. However, the fitting procedure to the measured geometric structure factors was insensitive to the overall phase  $\varphi$  of the distortions. Following this work, the atomic displacements having  $\Sigma_1$  symmetry corresponding to the triple period CDW in the 2H-TMDs are given by

$$\delta\mathbf{R} = \sum_{\mathbf{Q}} u \cos(\mathbf{Q} \cdot \mathbf{R} + \varphi) \hat{\mathbf{Q}}. \quad (2.2)$$

Here  $u$  is the amplitude and the sum runs over the vectors  $\mathbf{Q}_1 = \mathbf{b}_1/3$ ,  $\mathbf{Q}_2 = \mathbf{b}_2/3$ , and  $\mathbf{Q}_3 = -(\mathbf{b}_1 + \mathbf{b}_2)/3$ , where the reciprocal lattice vectors are given by  $\mathbf{b}_1 = \frac{2\pi}{a}(1/\sqrt{3}, 1)$  and  $\mathbf{b}_2 = \frac{2\pi}{a}(1/\sqrt{3}, -1)$ . The above atomic displacements also splits the lattice into three independent sublattices, where one of these sublattices does not experience displacements for any  $\varphi$ . We will determine the overall phase factor  $\varphi$  by minimizing the total energy. It can be seen that the magnitude of the displacements given by Eq. (2.2) will not depend on  $\varphi$ . Thus the elastic energy of the system will not depend on the phase of the CDW for this model system and our problem is reduced to finding

the phase that minimizes the energy of the conduction band. Expanding the crystal potential to first order in  $\delta\mathbf{R}$  given by Eq. (2.2) leads to the perturbation

$$\mathcal{H}' = \sum_{\mathbf{k}, \mathbf{Q}} \Delta_{\mathbf{k}}^{\mathbf{Q}} c_{\mathbf{k}}^{\dagger} c_{\mathbf{k}+\mathbf{Q}} + \text{h.c.} \quad (2.3)$$

where the wave vector  $\mathbf{k}$  is summed over the first Brillouin zone. For simplicity, we assume that the change in the hopping parameters due to the lattice distortion is proportional to the change in the absolute distance between neighboring atoms:  $\delta t_{\mathbf{R}\mathbf{R}'} \propto (\delta\mathbf{R} - \delta\mathbf{R}') \cdot (\mathbf{R} - \mathbf{R}')$ . Then

$$\Delta_{\mathbf{k}}^{\mathbf{Q}} = -ue^{-i\varphi} \sum_{\mathbf{R}} \gamma_{|\mathbf{R}|} (e^{-i\mathbf{Q}\cdot\mathbf{R}} - 1) e^{-i\mathbf{k}\cdot\mathbf{R}} \hat{\mathbf{Q}} \cdot \hat{\mathbf{R}} \quad (2.4)$$

where the lattice vector  $\mathbf{R}$  is summed over the *second* nearest neighbors to the atom at the origin and  $\gamma_{|\mathbf{R}|=2} > 0$  is the electron-phonon coupling constant in the unit of energy/distance. Since the unit cell of the distorted lattice contains nine sites of the original lattice, the renormalized energies  $\varepsilon_{\mathbf{k}}^{(n)}$  are given by the eigenvalues of the  $9 \times 9$  matrix

$$\tilde{\varepsilon}_{\mathbf{k}} = \begin{pmatrix} \varepsilon_{\mathbf{k}} & \Delta_{\mathbf{k}}^{\mathbf{Q}_1} & \Delta_{\mathbf{k}}^{\mathbf{Q}_2} & \Delta_{\mathbf{k}}^{\mathbf{Q}_3} & \Delta_{\mathbf{k}-\mathbf{Q}_1}^{\mathbf{Q}_1*} & \Delta_{\mathbf{k}-\mathbf{Q}_2}^{\mathbf{Q}_2*} & \Delta_{\mathbf{k}-\mathbf{Q}_3}^{\mathbf{Q}_3*} & 0 & 0 \\ \Delta_{\mathbf{k}}^{\mathbf{Q}_1*} & \varepsilon_{\mathbf{k}+\mathbf{Q}_1} & 0 & 0 & \Delta_{\mathbf{k}+\mathbf{Q}_1}^{\mathbf{Q}_1} & \Delta_{\mathbf{k}+\mathbf{Q}_1}^{\mathbf{Q}_3} & \Delta_{\mathbf{k}+\mathbf{Q}_1}^{\mathbf{Q}_2} & \Delta_{\mathbf{k}+\mathbf{Q}_1-\mathbf{Q}_2}^{\mathbf{Q}_2*} & \Delta_{\mathbf{k}+\mathbf{Q}_2-\mathbf{Q}_1}^{\mathbf{Q}_3*} \\ \Delta_{\mathbf{k}}^{\mathbf{Q}_2*} & 0 & \varepsilon_{\mathbf{k}+\mathbf{Q}_2} & 0 & \Delta_{\mathbf{k}+\mathbf{Q}_2}^{\mathbf{Q}_3} & \Delta_{\mathbf{k}+\mathbf{Q}_2}^{\mathbf{Q}_2} & \Delta_{\mathbf{k}+\mathbf{Q}_2}^{\mathbf{Q}_1} & \Delta_{\mathbf{k}+\mathbf{Q}_1-\mathbf{Q}_2}^{\mathbf{Q}_3*} & \Delta_{\mathbf{k}+\mathbf{Q}_2-\mathbf{Q}_1}^{\mathbf{Q}_1*} \\ \Delta_{\mathbf{k}}^{\mathbf{Q}_3*} & 0 & 0 & \varepsilon_{\mathbf{k}+\mathbf{Q}_3} & \Delta_{\mathbf{k}+\mathbf{Q}_3}^{\mathbf{Q}_2} & \Delta_{\mathbf{k}+\mathbf{Q}_3}^{\mathbf{Q}_1} & \Delta_{\mathbf{k}+\mathbf{Q}_3}^{\mathbf{Q}_3} & \Delta_{\mathbf{k}+\mathbf{Q}_1-\mathbf{Q}_2}^{\mathbf{Q}_1*} & \Delta_{\mathbf{k}+\mathbf{Q}_2-\mathbf{Q}_1}^{\mathbf{Q}_2*} \\ \Delta_{\mathbf{k}-\mathbf{Q}_1}^{\mathbf{Q}_1} & \Delta_{\mathbf{k}+\mathbf{Q}_1}^{\mathbf{Q}_1*} & \Delta_{\mathbf{k}+\mathbf{Q}_2}^{\mathbf{Q}_3*} & \Delta_{\mathbf{k}+\mathbf{Q}_3}^{\mathbf{Q}_2*} & \varepsilon_{\mathbf{k}-\mathbf{Q}_1} & 0 & 0 & \Delta_{\mathbf{k}-\mathbf{Q}_1}^{\mathbf{Q}_3} & \Delta_{\mathbf{k}-\mathbf{Q}_1}^{\mathbf{Q}_2} \\ \Delta_{\mathbf{k}-\mathbf{Q}_2}^{\mathbf{Q}_2} & \Delta_{\mathbf{k}+\mathbf{Q}_1}^{\mathbf{Q}_3*} & \Delta_{\mathbf{k}+\mathbf{Q}_2}^{\mathbf{Q}_2*} & \Delta_{\mathbf{k}+\mathbf{Q}_3}^{\mathbf{Q}_1*} & 0 & \varepsilon_{\mathbf{k}-\mathbf{Q}_2} & 0 & \Delta_{\mathbf{k}-\mathbf{Q}_2}^{\mathbf{Q}_1} & \Delta_{\mathbf{k}-\mathbf{Q}_2}^{\mathbf{Q}_3} \\ \Delta_{\mathbf{k}-\mathbf{Q}_3}^{\mathbf{Q}_3} & \Delta_{\mathbf{k}+\mathbf{Q}_1}^{\mathbf{Q}_2*} & \Delta_{\mathbf{k}+\mathbf{Q}_2}^{\mathbf{Q}_1*} & \Delta_{\mathbf{k}+\mathbf{Q}_3}^{\mathbf{Q}_3*} & 0 & 0 & \varepsilon_{\mathbf{k}-\mathbf{Q}_3} & \Delta_{\mathbf{k}-\mathbf{Q}_3}^{\mathbf{Q}_2} & \Delta_{\mathbf{k}-\mathbf{Q}_3}^{\mathbf{Q}_1} \\ 0 & \Delta_{\mathbf{k}+\mathbf{Q}_1-\mathbf{Q}_2}^{\mathbf{Q}_2} & \Delta_{\mathbf{k}+\mathbf{Q}_1-\mathbf{Q}_2}^{\mathbf{Q}_3} & \Delta_{\mathbf{k}+\mathbf{Q}_1-\mathbf{Q}_2}^{\mathbf{Q}_1} & \Delta_{\mathbf{k}-\mathbf{Q}_1}^{\mathbf{Q}_3*} & \Delta_{\mathbf{k}-\mathbf{Q}_2}^{\mathbf{Q}_1*} & \Delta_{\mathbf{k}-\mathbf{Q}_3}^{\mathbf{Q}_2*} & \varepsilon_{\mathbf{k}+\mathbf{Q}_1-\mathbf{Q}_2} & 0 \\ 0 & \Delta_{\mathbf{k}+\mathbf{Q}_2-\mathbf{Q}_1}^{\mathbf{Q}_3} & \Delta_{\mathbf{k}+\mathbf{Q}_2-\mathbf{Q}_1}^{\mathbf{Q}_1} & \Delta_{\mathbf{k}+\mathbf{Q}_2-\mathbf{Q}_1}^{\mathbf{Q}_2} & \Delta_{\mathbf{k}-\mathbf{Q}_1}^{\mathbf{Q}_2*} & \Delta_{\mathbf{k}-\mathbf{Q}_2}^{\mathbf{Q}_3*} & \Delta_{\mathbf{k}-\mathbf{Q}_3}^{\mathbf{Q}_1*} & 0 & \varepsilon_{\mathbf{k}+\mathbf{Q}_2-\mathbf{Q}_1} \end{pmatrix}. \quad (2.5)$$

We can now write the total energy as a function of the amplitude and phase of the distortion as

$$E_{\text{tot}}(u, \varphi) = \int_{-\infty}^{\mu} \varepsilon \rho(\varepsilon) d\varepsilon + E_{\text{el}}(u) \quad (2.6)$$

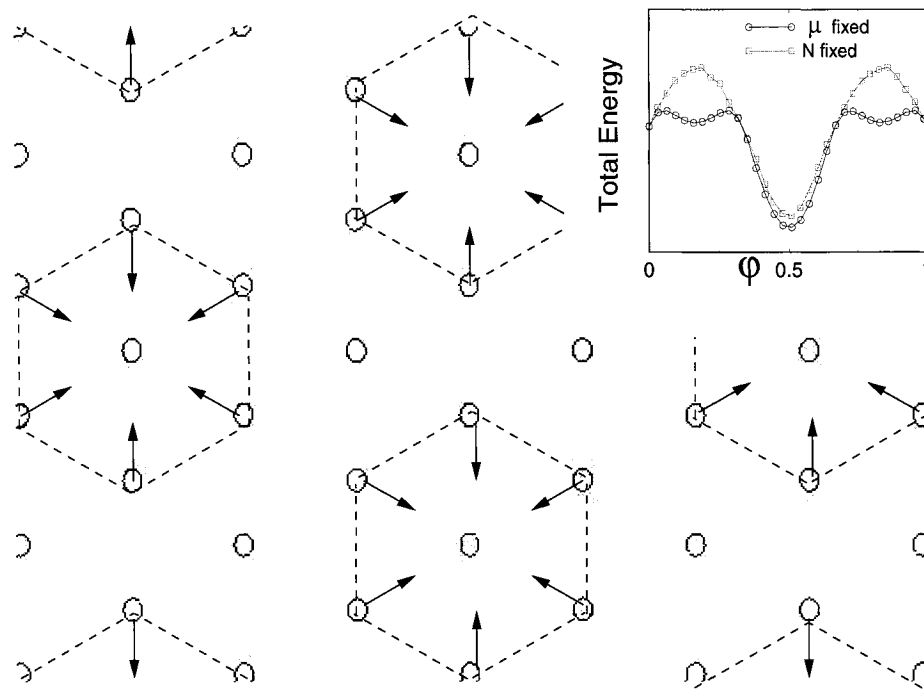


Figure 2.4: Atomic displacement pattern corresponding to the phase  $\varphi = \pi/2$  in Eq. (2.2). The inset shows the total energy of the CDW state as the function of phase  $\varphi$  where the total energy units are arbitrary and the phase is in units of  $\pi$ .

where  $\rho(\varepsilon) = \sum_{\mathbf{k},n} \delta(\varepsilon - \varepsilon_{\mathbf{k}}^{(n)})$  is the density of electronic states and  $E_{\text{el}}(u)$  is the elastic energy which, as we noted before, is independent of the phase of the distortion. The  $\mathbf{k}$ -integration is performed by using a fine Monkhorst-Pack mesh and corresponding weights [116] in the irreducible Brillouin zone of the triangular lattice. We determine the chemical potential  $\mu$  by considering two extreme cases: (i) Fixed particle number  $N$ , which corresponds to an isolated metallic band at the Fermi energy. (ii) Fixed  $\mu = 0$ , which corresponds to significant spectral weight from the other bands at the Fermi energy. The realistic situation, with two metallic bands at the Fermi energy arising from the multi-layer structure should reside somewhere between these two extremes. We find that the unanimous minimum for both extreme cases occurs when  $\varphi = \pi/2$ . This minimum will become more pronounced with increased electron-phonon coupling constant. In Fig. 2.4 we show the corresponding atomic displacement pattern, which is consistent with the charge maxima seen in scanning tunneling microscopy experiments [142, 30]. Furthermore, to check the robustness of this result, we have performed the same calculation, but with  $t_6$  set to zero, and have found that the minimal total energy still occurs at  $\varphi = \pi/2$ .

#### 2.1.4 Theoretical ARPES spectra

Now that the phase of the CDW has been determined we will analyze the renormalized quasiparticle dispersion in the presence of the CDW. The energy spectrum from the undistorted sublattice is shown in Fig. 2.5(a) and that from distorted sublattices is shown in Fig. 2.5(b) along the  $\Gamma\text{M}$  direction, which is along the nested region of the  $\Gamma$ -centered hexagonal Fermi surface. Clearly, those associated with



the undistorted sublattice do not change [Fig. 2.5(a)]. Thus, the corresponding subbands remain metallic in the CDW phase. On the other hand, the bands originating from the two distorted sublattices are doubly degenerate and we find a gap opens at the Fermi energy [Fig. 2.5(b)]. Moreover, to make comparison with experiment more direct, in Fig. 2.5(c) and Fig. 2.5(d) we present theoretical ARPES spectra  $A(\mathbf{k}, \omega) = \frac{1}{\pi} f(\omega) \text{Im}G(\mathbf{k}, \omega)$  where  $G(\mathbf{k}, \omega)$  is the single particle Green's function and  $f(\omega)$  is the Fermi distribution function for wave vectors in a small region of the nested portion of the Fermi surface. To emulate experimental data, we have chosen a broadening of  $\eta = 40$  meV of the spectral density function. In Fig. 2.5(b) both the gapped and ungapped bands are visible (for an account of the weightings of satellite bands in CDW materials, see Voit *et al.* [159]). The most direct comparison between experimental data is with the work of Valla *et al.* [158] where there is a plot similar to Fig. 2.5(a). It is also shown in this paper that no gap opens along  $\Gamma K$ , being consistent with Fig. 2.5(b).

A question that naturally follows is, how robust this result is when the finite first neighbor interaction—which mixes all bands and thus destroys the exact decoupling into the three independent sublattices—is taken into account. We examine this issue, switching on the first-neighbor electron-phonon coupling constant  $\gamma_1$  in Eq. (2.4), up to a third of the value of  $\gamma_2$  as suggested by the first principles results:  $t_1 \simeq t_2/3$ . As expected, we find that the degeneracy of the bands originating from the distorted sublattices shown in Fig. 2.5(b) is lifted. In addition, the triple degeneracy originating from the undistorted sublattice shown in Fig. 2.5(a) at the Fermi energy is lifted. However, this does *not* produce a quasiparticle gap at the Fermi energy. More

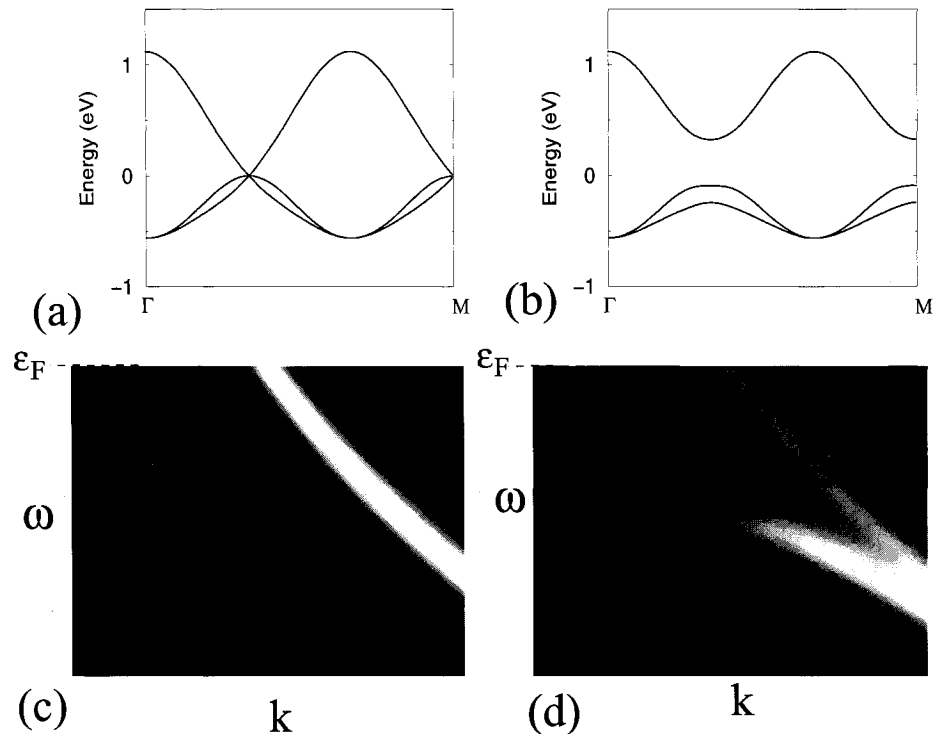


Figure 2.5: The bands in the low temperature CDW state originating from the undistorted (a) and distorted (b) sublattices. The increase in the number of bands corresponds to backfolding resulting from the  $3 \times 3$  supercell. Theoretical ARPES spectra for the normal (c) (corresponding to vanishing electron-phonon coupling) and CDW (d) states for wave vectors over the nested region of the Fermi energy along  $\Gamma M$ . The energy range is  $-0.47$  to  $0$  eV relative to the Fermi energy and the momentum range is  $\frac{b_1+b_2}{3} \frac{3}{10}$  to  $\frac{b_1+b_2}{3} \frac{7}{10}$ .

specifically, this triple degeneracy is lifted in such a way that two of the energies are increased to above the Fermi energy and the other one is decreased to below the Fermi energy. It can be seen that this will indeed not gap the Fermi surface, given  $\gamma_1$  is considerably smaller than  $\gamma_2$ .

### **2.1.5 Conclusion**

In conclusion, we have studied the CDW state in the 2H-transition metal dichalcogenides and found that due to a unique feature in the electronic structure of these materials revealed from first-principles calculations, the triangular lattice can be effectively decoupled into three independent sublattices, with one remaining undistorted in the CDW phase. As illustrated with a model calculation, this leads to the remarkable situation where no regions of the entire Fermi surface become gapped even when these materials exhibit a commensurate CDW.

### **2.1.6 Acknowledgements**

The work done at Harvard University was supported by the NSF (DMR-0132874, DMR-0231631), the Sloan Foundation, and Harvard NSEC and MRSEC (DMR-0213805). The work done at Brookhaven National Laboratory was supported by U.S. Department of Energy under Contract No. DE-AC02-98CH1-886 and DOE-CMSN. W.Y. and W.K. thank A.M. Tsvelik and T. Valla for helpful discussions.

## 2.2 The temperature dependence of the electronic self-energy

### 2.2.1 Introduction

In a recent set of very interesting experiments the quasiparticle self-energy of 2H-TaSe<sub>2</sub> [158] and 2H-NbSe<sub>2</sub> was determined by ARPES experiments. This was done by measuring the dressed quasiparticle energies,  $\varepsilon_{\mathbf{k}}$ , and using then using the relation  $\varepsilon_{\mathbf{k}} = \varepsilon_{\mathbf{k}}^{(0)} + \text{Re}(\Sigma(\mathbf{k}, \varepsilon_{\mathbf{k}}))$  to determine the quasiparticle self-energy where a linear form for the bare energy  $\varepsilon_{\mathbf{k}}^{(0)}$  is typically assumed. Similar studies have revealed the mysterious “kink” structure in the quasiparticle energies of the cuprate superconductors [95]. For 2H-TaSe<sub>2</sub> it was found that at temperatures close to and above the commensurate transition temperature of 90K, there is a peak in the real part of the quasiparticle self-energy  $\text{Re}(\Sigma(\omega))$  at  $\omega_{\text{peak}} = 30$  meV. This peak is consistent with coupling to a phonon mode (the maximum phonon energy is 40 meV). As the temperature was reduced below the CDW transition temperature, the peak position experienced an upward shift until reaching the low-temperature value of  $\omega_{\text{peak}} = 65$  meV at 34 K. Since this peak energy exceeds the energy of any phonon, it was attributed to the appearance of an exotic collective bosonic mode below the CDW transition temperature and not to phonons [158]. In the more recent experiment on 2H-NbSe<sub>2</sub> [157] a peak at  $\omega_{\text{peak}}$  was observed which had no measurable temperature dependence.

In the following, we will propose an alternative explanation of the these experiments. We will show that the peak position in the quasiparticle energy will occur

at

$$\omega_{\text{peak}}(T) = \Omega_{\text{ph}} + |\Delta_{\text{CDW}}(T)| \quad (2.7)$$

where  $\Omega_{\text{ph}} = 30$  meV is the energy of an optical phonon mode and  $\Delta_{\text{CDW}}(T)$  is the energy of the charge-density wave gap which has temperature dependence. The shift in the quasiparticle energy of 35 meV is consistent with the low temperature CDW gap energies of 2H-TaSe<sub>2</sub>. We argue that the peak shift of 2H-NbSe<sub>2</sub> is unobservable because of its significantly smaller CDW gap.

### 2.2.2 Simple model

We will consider coupling to a single dispersionless phonon mode of energy  $\Omega$  and electron-phonon coupling constant which has weak momentum transfer dependence  $g_{\mathbf{k}\mathbf{k}'} \approx g$  where  $\mathbf{k}$  and  $\mathbf{k}'$  are on the Fermi surface. Then Migdal's expression for the electronic self-energy is

$$\Sigma(\omega) = ig^2 \sum_{\mathbf{k}'} \int \frac{d\omega'}{2\pi} G(\mathbf{k}', \omega' + i\eta\omega') D(\omega - \omega'). \quad (2.8)$$

where the phonon Green's function is

$$D(\omega) = \frac{2\Omega}{(\omega - \Omega + i\eta)(\omega + \Omega - i\eta)}. \quad (2.9)$$

We can now perform a Wick rotation in the energy integral to obtain the expression

$$\begin{aligned} \Sigma(\omega) = & g^2 \sum_{\mathbf{k}'} \int \frac{d\omega'}{2\pi} G(\mathbf{k}', i\omega') \frac{2\Omega}{(\omega' + i\omega)^2 + \Omega^2} \\ & + g^2 \theta(\omega - \Omega) \sum_{\mathbf{k}'} G(\mathbf{k}', \omega - \Omega + i\eta) + g^2 \theta(-\omega - \Omega) \sum_{\mathbf{k}'} G(\mathbf{k}', \omega + \Omega - i\eta) \end{aligned} \quad (2.10)$$

Numerically evaluating Eq. 2.10 will sometimes prove to be easier than directly evaluating Eq. 2.8.

As an initial step, we will consider the simple 1d tight-binding band  $\varepsilon_k = -2t \cos(k)$  at half filling which undergoes a period two CDW transition. This band has the simplifying feature that  $\varepsilon_{k+\pi} = -\varepsilon_k$ , and the Green's function is

$$G(k, \omega) = \frac{\omega + \varepsilon_k}{(\omega - \varepsilon_k)(\omega + \varepsilon_k) - |\Delta|^2}. \quad (2.11)$$

With this, using Eq.2.10, we obtain

$$\begin{aligned} \Sigma(\omega) = & -ig^2\nu(0)\pi \int \frac{d\omega'}{2\pi} \frac{\omega'}{\sqrt{\omega'^2 + |\Delta|^2}} \frac{2\Omega}{(\omega' + i\omega)^2 + \Omega^2} \\ & -ig^2\nu(0)\pi \frac{\omega - \Omega}{\sqrt{(\omega - \Omega)^2 - |\Delta|^2 + i\eta}} \theta(\omega - \Omega) \\ & -ig^2\nu(0)\pi \frac{\omega + \Omega}{\sqrt{(\omega + \Omega)^2 - |\Delta|^2 + i\eta}} \theta(-\omega - \Omega) \end{aligned} \quad (2.12)$$

where the first term is to be evaluated numerically. At  $|\Delta| = 0$ , the above expression reduces to

$$\Sigma(\omega) = g^2\nu(0) \log \left| \frac{\omega - \Omega}{\omega + \Omega} \right| - ig^2\nu(0)\pi\theta(\omega - \Omega) - ig^2\nu(0)\pi\theta(-\omega - \Omega). \quad (2.13)$$

We find, as shown in Fig. 2.6, that the position of the peak in  $\text{Re}(\Sigma(\omega))$  is at  $\omega_{\text{peak}} = \Omega + |\Delta|$ , which is the relation stated above in Eq. 2.7. The above analysis can also be carried out at finite temperature. It is found that the divergences occurring at  $\omega = \Omega + \Delta$  are replaced by maxima which have a logarithmic dependence on temperature.

The features in the electronic self-energy can be understood by the following qualitative arguments. Consider a hole injected into the material in the normal state

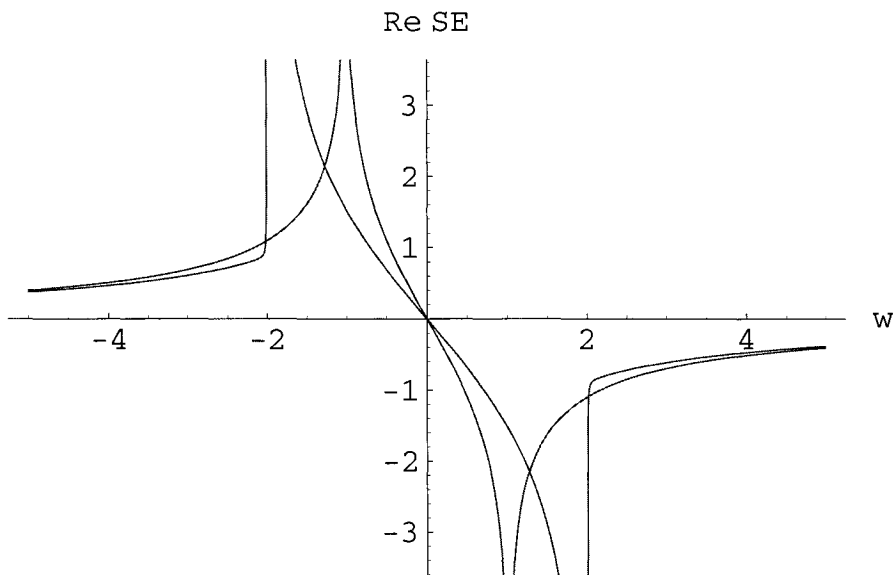


Figure 2.6: The real part of the electronic self-energy as a function of  $\omega$  for  $\Delta = 0$  (blue) and  $\Delta = \Omega$  (red). The horizontal axis is in units of  $\Omega$  and the vertical axis has arbitrary units.

with energy  $\omega$  satisfying  $\omega < -\Omega$  labeled as (2) in Fig. 2.7 (a). Then a higher energy electron can emit a phonon of energy  $\Omega$  and decay into this hole, giving the excitation a finite lifetime. On the other hand, if the energy of the hole is in the range  $-\Omega < \omega < 0$  as shown as (1) in Fig. 2.7 (a), then there is no similar process, which means that the hole will have an infinite lifetime. Similar conclusions can be reached by considering the injection of electrons above the Fermi energy. The lifetimes of these excitations gives information about the imaginary part of the electronic self-energy. Namely,  $\text{Im}(\Sigma(\omega))$  will be zero in the region  $-\Omega < \omega < \Omega$ , and outside this region will obtain finite values. The real part of the self-energy can then be obtained by use of the Kramers-Kronig relations. A schematic depiction of the arguments for the CDW phase is given in Fig. 2.7 (b). Here, a gap in the density of states of width  $2|\Delta|$  is opened at the Fermi energy for the model discussed above. Using similar

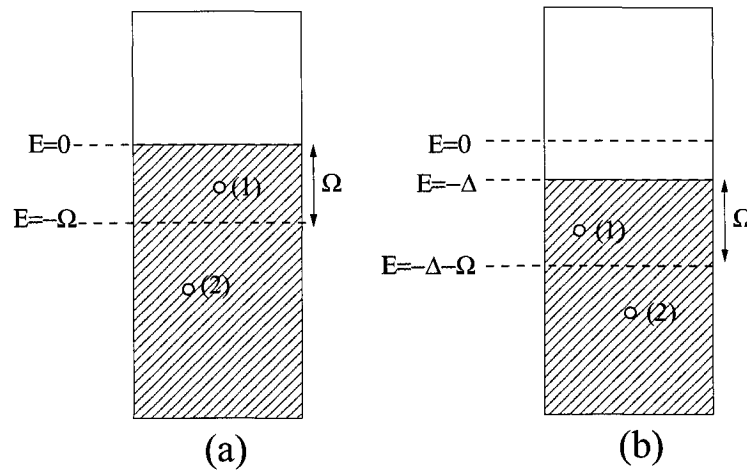


Figure 2.7: Schematic depiction of hole injection into the normal (a) and CDW (b) phases of the TMDs. By considering scattering from a single optical phonon, one can conclude that the holes labeled as (1) will have infinite lifetimes whereas the holes labeled by (2) will have finite lifetimes.

arguments as above, one sees that injected holes with energies  $-\Omega - \Delta < \omega < -\Delta$  will have infinite lifetimes while holes injected with energy  $\omega < -\Omega - \Delta$  will have finite lifetimes with similar results holding for injected electrons. This means that the  $\text{Im}(\Sigma(\omega))$  will be zero in the range  $-\Omega - \Delta < \omega < \Omega + \Delta$  and outside this range will be finite.

### 2.2.3 Realistic Computation

Now we want to provide a more realistic calculation of the self-energy shift as a function of the gap by using the the band structure energies  $\varepsilon_{\mathbf{k}}$  given in Eq. 2.1 and the gap  $\Delta_{\mathbf{k}}^{\mathcal{Q}}$  given in Eq. 2.2. Also, to be consistent, we will calculate the self-energy at finite temperature. At finite temperature, the self-energy for the retarded electronic



Green's function corresponding to Eq. 2.8 can be expressed as [1]

$$\Sigma(\omega) = \frac{g^2}{2} \int dz \nu(z) \left( \frac{\tanh(\frac{1}{2}\beta z) - \coth(\frac{1}{2}\beta\Omega)}{z - \omega - \Omega - i\eta} - \frac{\tanh(\frac{1}{2}\beta z) + \coth(\frac{1}{2}\beta\Omega)}{z - \omega + \Omega - i\eta} \right) \quad (2.14)$$

where  $\nu(z)$  is the density of states obtained from the eigenvalues of the matrix Eq. 2.5 and  $\beta$  is inverse temperature. We will again use the Monkhorst-Pack method [116] to generate a mesh and weights in the first BZ to carry out the  $\mathbf{k}$ -integration. We fix the optical phonon frequency at  $\Omega = 30$  meV, and, as discussed above, use the hopping value  $t = 0.21$  eV in the expression for the band structure energies.

Now we need to obtain quantitative values for the CDW gap. In the low-temperature STM experiment of Wang *et al.* [162] an abrupt change in the slope of the tunneling conductance was found at a bias voltage of 80 meV which was attributed to the magnitude of the zero-temperature CDW gap:  $\Delta_{\text{CDW}}(0) = 80$  meV. We use the mean field result

$$\Delta_{\text{CDW}}(T) = \Delta_{\text{CDW}}(0) \sqrt{1 - \frac{T}{T_{\text{CDW}}}} \quad (2.15)$$

to obtain values of the finite temperature gap where  $T_{\text{CDW}} = 90$  K is the commensurate CDW transition temperature for 2H-TaSe<sub>2</sub>. There is some ambiguity in defining the magnitude of the gap in our model since  $\Delta_{\mathbf{k}}^{\mathbf{Q}}$  in Eq. 2.4 has  $\mathbf{k}$ -dependence. We adopt the definition  $\Delta_{\text{CDW}} = \frac{1}{2} \max_{\mathbf{k}} |\Delta_{\mathbf{k}}^{\mathbf{Q}}|$ . Now with all these parameters specified, we can calculate the shift in  $\omega_{\text{peak}}$  ( for occupied states) as a function of temperature which is shown in Fig. 2.9 which is in quantitative agreement with the experiments of Valla *et al.* [158]. Because of the approximate nesting condition, there is a maximum in the density of states within 30 meV of the Fermi energy. Because this is on the order of the phonon frequencies and the gap, the standard approximation of taking the electronic density of states to be constant around the Fermi energy (which we

used in the previous section of the toy model) is not valid here.

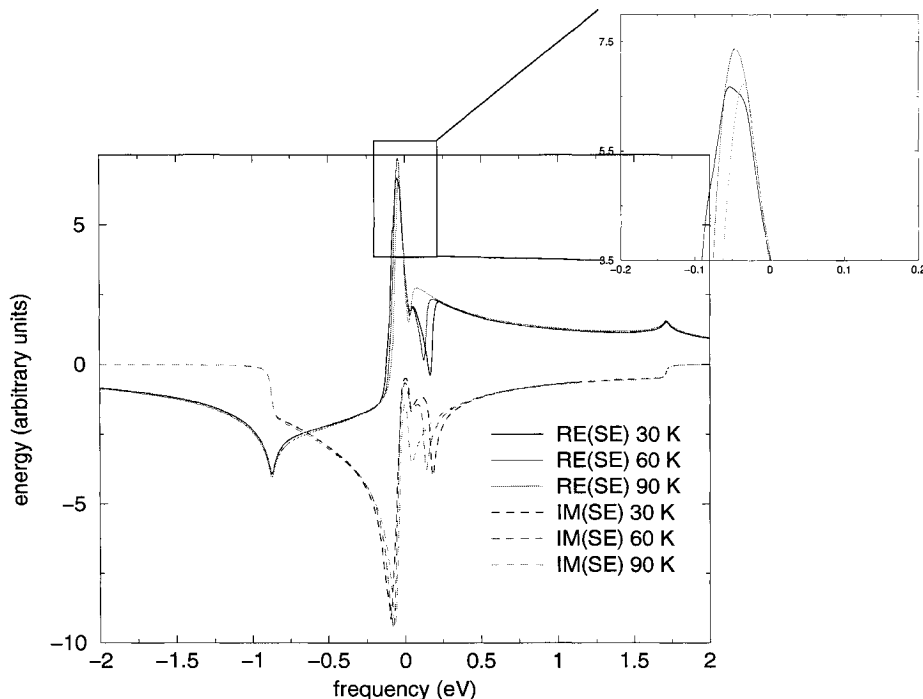


Figure 2.8: The real and imaginary parts of the finite-temperature retarded self-energy for various temperatures.

According to the Drude approximation for electronic transport in solids, the resistivity is proportional to the scattering rate of electrons at the Fermi energy. Using Eq. 2.14, this temperature-dependent rate can be expressed as

$$\Gamma(T) = |\text{Im}(\Sigma(\omega = 0))| = g^2 \pi \left| \frac{\nu(\Omega) + \nu(-\Omega)}{\sinh(\frac{1}{2}\beta\Omega)} \right|. \quad (2.16)$$

Note that the density of states in  $\nu(\omega)$  in this expression has temperature dependence which enters through  $\Delta_{\text{CDW}}(T)$  below the CDW transition temperature. However, for temperatures greater than the CDW transition temperature, the temperature dependence will come exclusively from the denominator in Eq. 2.16. In the experiment of Valla *et al.* in Ref.citeValla00, it was observed that the temperature dependent

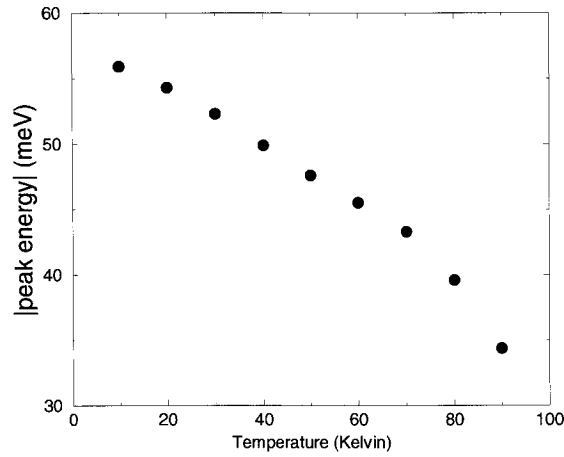


Figure 2.9: The energy for which the peak in the electronic self-energy occurs  $\omega_{\text{peak}} < 0$  as a function of temperature.

scattering rates at the Fermi energy extracted from ARPES measurements, were in close correspondence with the resistivity measured from transport experiments. For comparison, we plot the scattering rate  $\Gamma(T)$  calculated from our model in Fig. 2.10. This shows a change of slope at  $T_{\text{CDW}}=90$  K which is qualitatively consistent with the temperature-dependent resistivity of 2H-TaSe<sub>2</sub>.

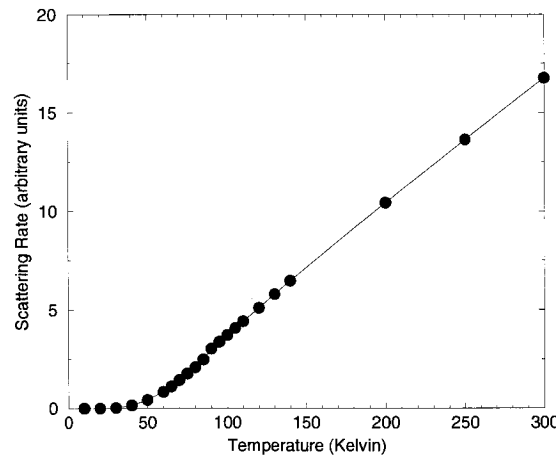


Figure 2.10: The scattering rate  $\Gamma(T)$  as a function of temperature which exhibits a cusp at  $T_{\text{CDW}}=90$  K.

## 2.3 Fourier STM analysis

The recently developed method of high-resolution Fourier-transform scanning-tunneling microscopy (FT-STM) [66, 108, 68] has yielded much insight into the nature of the cuprate superconductors, and the experiments have been analyzed from various theoretical perspectives [127, 23, 128, 11]. In this section, we consider the possible insights that similar experiments would give for the TMD materials.

### 2.3.1 Formalism

Real-space STM experiments measure the local density of electronic states which can be expressed as

$$\nu(\mathbf{x}, \omega) = \frac{1}{\pi} \text{Im} (G(\mathbf{x}, \mathbf{x}, \omega)) \quad (2.17)$$

where

$$G(\mathbf{x}, \mathbf{x}', \omega) = \langle \mathbf{x} | \hat{G}(\omega) | \mathbf{x}' \rangle = \langle \mathbf{x} | (\omega - \mathcal{H} - i\eta)^{-1} | \mathbf{x}' \rangle \quad (2.18)$$

is the real-space Green's function. In this,  $|\mathbf{x}\rangle = \psi^\dagger(\mathbf{x}) |0\rangle$  where  $\psi(\mathbf{x})$  is the electron field operator. The Fourier transform of the local density of states  $\nu(\mathbf{x}, \omega)$  is performed to yield  $\nu(\mathbf{q}, \omega)$ . Consider now adding an impurity to our system represented by the potential  $\hat{V}_{\text{imp}}$ . In the Born approximation we obtain

$$\langle \mathbf{x} | \hat{G}(\omega) | \mathbf{x}' \rangle = \langle \mathbf{x} | \hat{G}_0(\omega) | \mathbf{x}' \rangle + \langle \mathbf{x} | \hat{G}_0(\omega) \hat{V}_{\text{imp}} \hat{G}_0(\omega) | \mathbf{x}' \rangle. \quad (2.19)$$

where  $\hat{G}_0$  is the Green's function operator in the absence of the impurity potential. The contribution to  $\nu(\mathbf{q}, \omega)$  from the first term in this equation will essentially be peaks at each reciprocal lattice vector. On the other hand, the second term can reveal more subtle information concerning the nesting of the Fermi surface. In the

following, we will concentrate exclusively on the implications of this second term resulting from impurity scattering and label the resulting contribution to the Fourier transformed local density of states as  $\nu_{\text{imp}}(\mathbf{q}, \omega)$ .

Let  $|\mathbf{k}\rangle$  denote an eigenstate of the undistorted Hamiltonian  $\mathcal{H}_0$  of energy  $\varepsilon_{\mathbf{k}}$ .

Inserting these states, we obtain

$$\begin{aligned} & \langle \mathbf{x} | \hat{G}_0(\omega) \hat{V}_{\text{imp}} \hat{G}_0(\omega) | \mathbf{x} \rangle \\ &= \sum_{\mathbf{k}, \mathbf{k}', \mathbf{k}'', \mathbf{k}''' \in \text{BZ}} \langle \mathbf{x} | \mathbf{k} \rangle \langle \mathbf{k} | \hat{G}_0(\omega) | \mathbf{k}' \rangle \langle \mathbf{k}' | \hat{V}_{\text{imp}} | \mathbf{k}'' \rangle \langle \mathbf{k}'' | \hat{G}_0(\omega) | \mathbf{k}''' \rangle \langle \mathbf{k}''' | \mathbf{x} \rangle \\ &= \sum_{\mathbf{k}, \mathbf{k}' \in \text{BZ}; \mathbf{Q}, \mathbf{Q}'} \langle \mathbf{x} | \mathbf{k} \rangle \langle \mathbf{k} | \hat{G}_0(\omega) | \mathbf{k} + \mathbf{Q} \rangle \langle \mathbf{k} + \mathbf{Q} | \hat{V}_{\text{imp}} | \mathbf{k}' + \mathbf{Q}' \rangle \langle \mathbf{k}' + \mathbf{Q}' | \hat{G}_0(\omega) | \mathbf{k}' \rangle \langle \mathbf{k}' | \mathbf{x} \rangle \end{aligned} \quad (2.20)$$

where the  $\mathbf{Q}$  sums are over the nine vectors  $0, \mathbf{Q}_1, \mathbf{Q}_2, \mathbf{Q}_3, -\mathbf{Q}_1, \dots$  which are the vectors pointing to the centers of the nine hexagons in the first Brioullin zone shown in Fig. 2.3. To simplify things in taking the Fourier transform of the above expression, we will take

$$\langle \mathbf{x} | \mathbf{k} \rangle = \frac{1}{\sqrt{\Omega}} e^{i\mathbf{k} \cdot \mathbf{x}} \quad (2.21)$$

where  $\Omega$  is the volume of the system noting that a more detailed expression for the Bloch functions of the undistorted lattice should not change the qualitative features of  $\nu(\mathbf{q}, \omega)$ . Taking the Fourier transform, and assuming that  $V_{\text{imp}}(\mathbf{x})$  has inversion symmetry, we finally obtain

$$\begin{aligned} \nu_{\text{imp}}(\mathbf{q}, \omega) &= \frac{1}{\pi} \text{Im} \left( \sum_{\mathbf{k} \in \text{RBZ}; \mathbf{Q}, \mathbf{Q}', \mathbf{Q}''} \langle \mathbf{k} + \mathbf{q} + \mathbf{Q} | \hat{G}_0(\omega) | \mathbf{k} + \mathbf{q} + \mathbf{Q}' \rangle \right. \\ &\quad \times \left. \langle \mathbf{q} + \mathbf{Q}' | \hat{V}_{\text{imp}} | \mathbf{Q}'' \rangle \langle \mathbf{k} + \mathbf{Q}'' | \hat{G}_0(\omega) | \mathbf{k} + \mathbf{Q} \rangle \right) \end{aligned} \quad (2.22)$$

where the  $\mathbf{k}$ -summation is over the reduced Brillouin zone composed of the innermost hexagon in Fig. 2.3 having one ninth of the area of the total Brioullin zone. Using

our expression for the matrix Green's function  $\mathcal{G}(\mathbf{k}, \omega)$ , the expression for  $\nu(\mathbf{q}, \omega)$  can be rewritten in the convenient form

$$\nu_{\text{imp}}(\mathbf{q}, \omega) = \frac{1}{\pi} \text{Im} \left( \text{Tr} \left( \sum_{\mathbf{k} \in \text{RBZ}} \tilde{\mathcal{G}}(\mathbf{k} + \mathbf{q}, \omega) \tilde{\mathcal{V}}_{\text{imp}}(\mathbf{q}) \tilde{\mathcal{G}}(\mathbf{k}, \omega) \right) \right) \quad (2.23)$$

where  $\tilde{\mathcal{V}}_{\text{imp}}$  is the  $9 \times 9$  impurity potential matrix

### 2.3.2 Results and discussion

In Fig. 2.11, we show several FT-STM plots evaluated for various energies  $\omega$  viewed over the same region in reciprocal space as in Fig. 2.3 for the normal phase of the TMDs.

We now place a delta-function impurity at a site on one of the sublattices which experiences distortion in the CDW phase. Placing the impurity at such a location has the effect of modifying only the band structure energies associated with this sublattice. If the impurity were placed at a site on the sublattice which does not experience distortion in the CDW phase, then information on the CDW phase could not be obtained through the respective FT-STM plots.

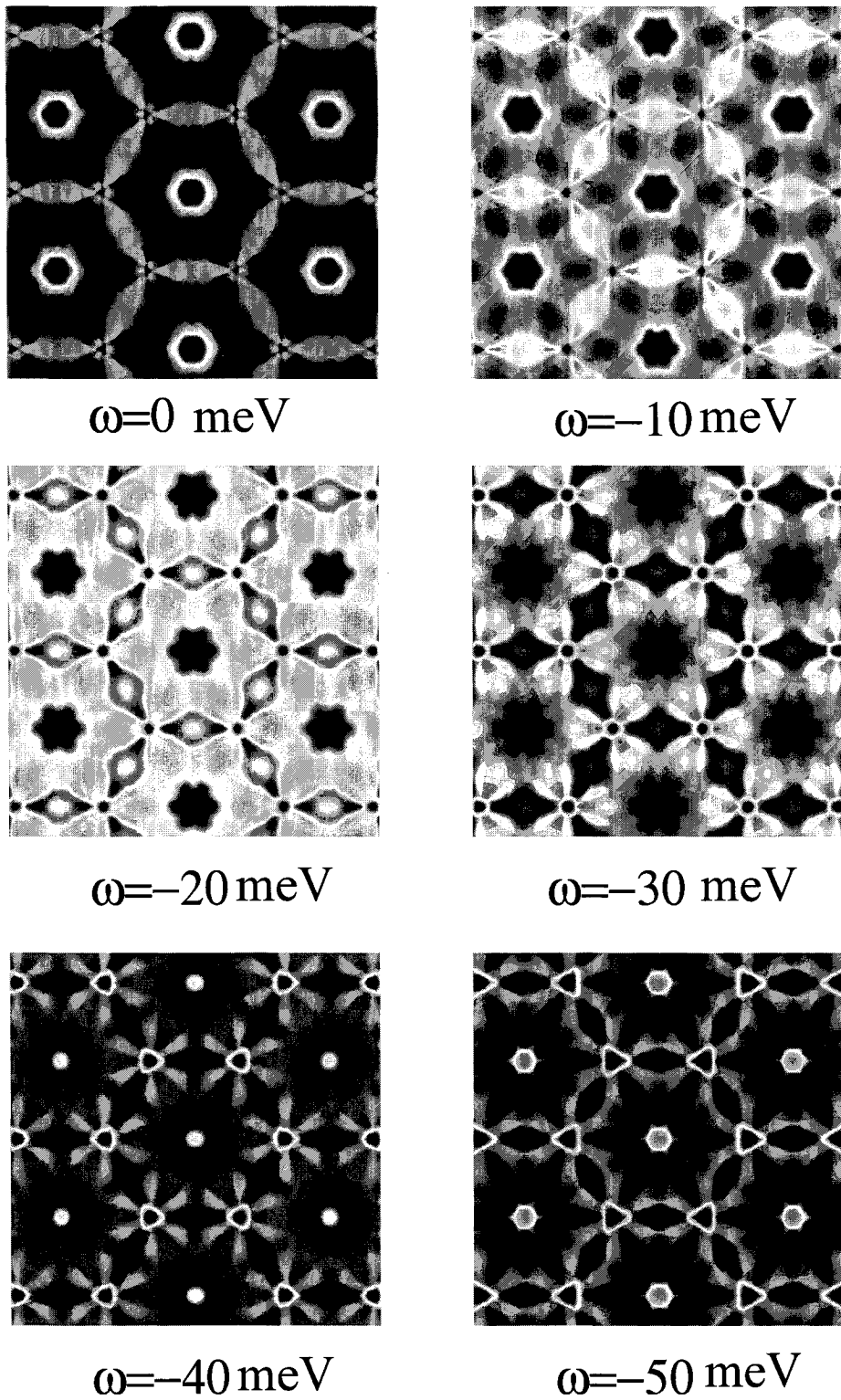


Figure 2.11: FT-STM images obtained by calculating  $\nu_{\text{imp}}(\mathbf{q}, \omega)$ . The range of  $\mathbf{q}$  is the same as used in Fig. 2.3. These plots correspond to the normal phase ( $\Delta_{\mathbf{k}}^Q = 0$ ).

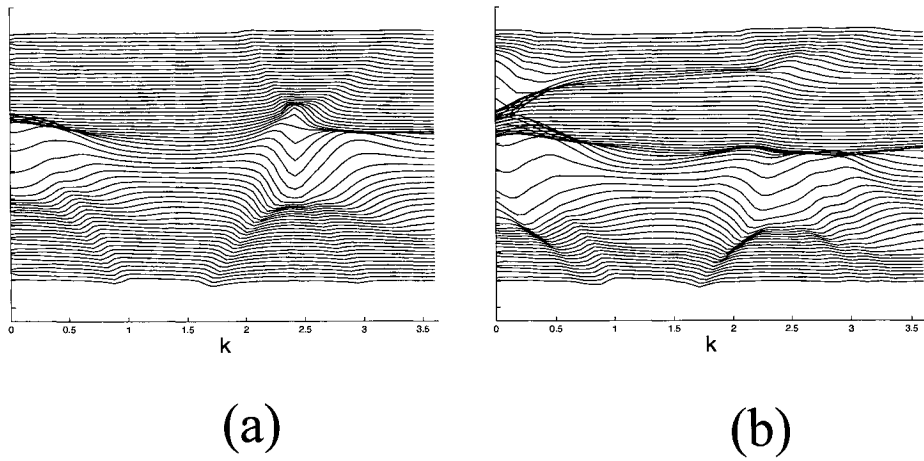


Figure 2.12: Plots of  $\nu_{\text{imp}}(\mathbf{q}, \omega)$  for  $\mathbf{q}$  along  $\Gamma M$ . Curves for  $\omega = -300$  meV through  $\omega = 300$  meV are shown in steps of 10 meV. The plots are offset with respect to each other for visualization. (a) corresponds to the normal state while (b) corresponds to the low-temperature CDW state.



# Chapter 3

## Electronic properties of DNA

### 3.1 Introduction

The notion of efficient charge transport along the stacked  $\pi$  orbitals of the bases in DNA was proposed [45] soon after Watson and Crick's discovery of its structure [163]. From both biological and technological considerations, interest in the electronic properties of DNA has been renewed recently. Over a decade ago Barton and co-workers observed distance-independent charge transfer between DNA-intercalated transition-metal complexes [119] which was argued to be relevant for biology and biotechnology (a review of electron transport experiments is given by [35]). Recent electron transport experiments on DNA have yielded widely varying results, showing insulating [19, 34, 146, 173], semiconducting [129], Ohmic conductivity [50, 22, 155, 28], and proximity induced superconductivity [83]. The large number of relevant variables endemic to such experiments explains the variability of results. Two such variables are the DNA-electrode contact resistances and the variations in the DNA molecules

and their environments (for a recent review of transport theory and experiments see Ref. [48]).

Theoretical efforts to understand electron transport in DNA can be divided into two categories:

In the first, model calculations use effective hamiltonians and master equations to describe the dynamics of electrons and holes in DNA (see, for instance, the papers by Yamada [168] and Iguchi [71] and references therein). Recent results [21] have led to considerable insights concerning the sequence-independent delocalization of electronic states in DNA. However, the main limitation of such approaches lies in the difficulty of determining accurate values for the parameters in the effective hamiltonians. In the second category, *ab-initio* calculations are employed for accurate and detailed description of the electronic features; these approaches are limited by the large number of atoms required for a realistic representation of the DNA molecules.

In this study, we address the problem of DNA stretching effects on electron localization by providing a bridge between these two extremes. As a representative model, we consider an 18 base-pair poly(CG)-poly(CG) DNA sequence, which can be synthesized using standard laboratory techniques, stretched up to 90% of its natural length where the unstretched structure is in the B form. We employ the well-established stretched structures obtained in the atomistic simulations of Lebrun and Lavery [96] and compute the electronic structure of this finite system with an efficient and realistic self-consistent tight-binding model [47]. Earlier calculations with our approach [106] and, independently, with *ab initio* approaches [34], have established that the highest occupied molecular orbitals (HOMO) and lowest unoccupied molecular or-

bitals (LUMO) are extended along the molecule, centered on the guanine (G) and cytosine (C) bases respectively.

In order to employ these results in further analysis of electron localization, we construct maximally localized states  $|\tilde{\psi}_i\rangle$  which reside on single bases by forming the appropriate linear combinations of the HOMO and LUMO states. With these maximally localized states we compute the hopping matrix elements  $t_{ij} = \langle \tilde{\psi}_i | \mathcal{H} | \tilde{\psi}_j \rangle$  between neighboring bases, thereby constructing an effective 1d chain model for this system which can be diagonalized to yield a simplified effective hamiltonian describing the dynamics of the valence and conduction electrons in the stretched forms of DNA. This enables us to obtain the electronic band energies of an infinite system based on the information from the finite molecule calculation. To include the effects of disorder, we add a random on-site energy term which leads to electronic localization. To quantify this effect, we diagonalize the new hamiltonian including disorder, and find that stretching leads to dramatic reduction of the localization length, by several orders of magnitude for a very modest amount of disorder. This calculation, and comparison to recent experiments with which it is in agreement, proves that the conformation of DNA plays a pivotal role in characterizing its conducting properties.

## 3.2 Constructing the tight-binding hamiltonian from the maximally localized Wannier states

In this section we describe the bottom-up approach used to construct effective tight-binding models for the conduction and valence electrons in stretched DNA,

starting from an all-atom quantum mechanical calculation. For the detailed electronic structure calculations we use an efficient quantum-mechanical approach which employs an atomic orbital basis set [47]. In this method, the ground state energy is calculated by a second order expansion in the electronic density, and takes into account self-consistently the charge transfer which is important for biological systems. As a first test of this method, we computed the band gap of poly(C)-poly(G) DNA to be 2.1 eV [106] and found that it is in excellent agreement with the published *ab-initio* result of de Pablo *et al.* [34] of 2.0 eV. In the remainder of this paper we will restrict our attention to the canonical poly(CG)-poly(CG) structure of DNA.

We took the structures obtained in the pioneering study of Lebrun and Lavery [96]. Here, the adiabatic elongation of selected DNA molecules was modeled and two modes of stretching were considered corresponding to pulling on opposite 3'-3' ends or 5'-5' ends: In the 3'-3' stretching mode, the DNA helix is unwound leading to a ribbon-like structure, while in the 5'-5' stretching mode the DNA helix contracts. The molecule can be reversibly stretched up to 90% of its natural length after which breaking occurs, consistent with single-molecule stretching experiments [143, 27, 148]. We compute the electronic structure of each of the stretched poly(CG)-poly(CG) DNA structures (see Fig. 3.1).

We now move on to describe our method of constructing maximally localized states on single base pairs, by taking linear combinations of the HOMO and LUMO states from the electronic structure method. These maximally localized states are then used to calculate the hopping parameters in the effective 1d hamiltonian. Let  $|\psi_n\rangle$  be the electronic eigenfunctions in the conduction or valence bands with corresponding

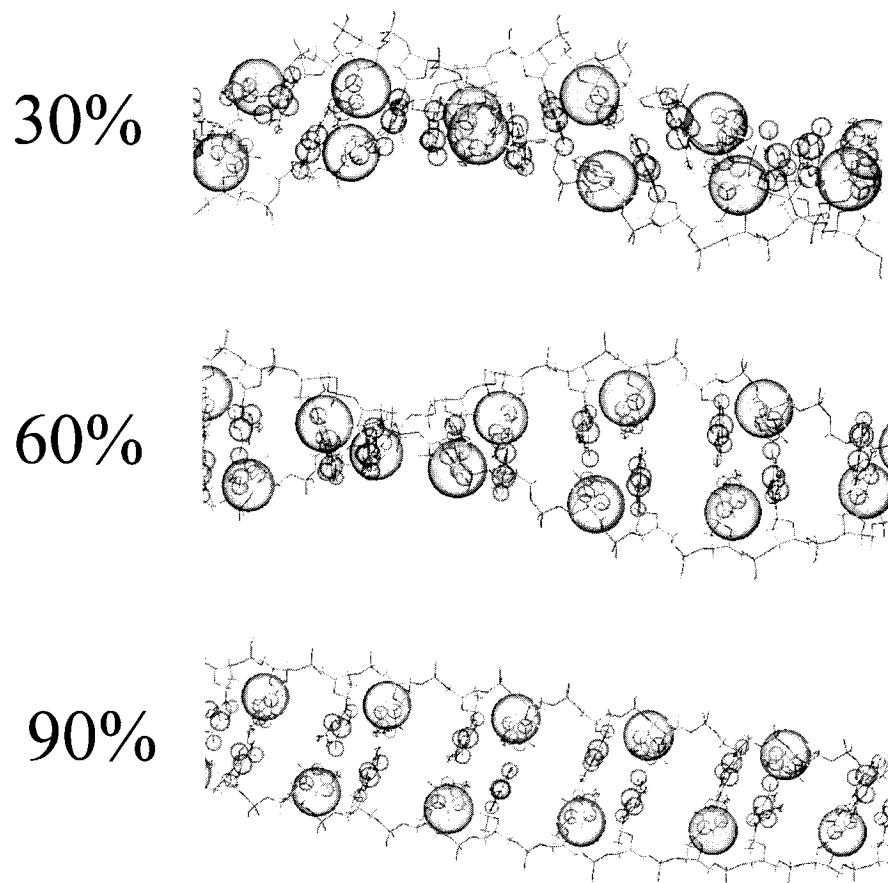


Figure 3.1: The DNA structures for different stretching magnitudes for the 3'-3' mode. For visualization purposes, we represent the calculated electronic density for the valence and conduction bands as blue and red spheres, respectively. The volume of a sphere centered on a particular atom is proportional to the electronic density.

energies  $\varepsilon_n$ . We wish to find the maximally localized states  $|\tilde{\psi}_i\rangle$  obtained by the unitary transformation

$$|\tilde{\psi}_i\rangle = \sum_n \langle \psi_n | \tilde{\psi}_i \rangle |\psi_n\rangle. \quad (3.1)$$

which minimizes the sum of the variances

$$\zeta = \sum_i \left( \langle \tilde{\psi}_i | \hat{z}^2 | \tilde{\psi}_i \rangle - \langle \tilde{\psi}_i | \hat{z} | \tilde{\psi}_i \rangle^2 \right) \quad (3.2)$$

under the constraint  $\langle \tilde{\psi}_i | \tilde{\psi}_j \rangle = \delta_{ij}$  where  $z$  is the position along the helical axis. Due to the invariance of the trace, the first term in Eq. 3.2 is independent of the unitary transformation and our problem is simplified to maximizing the second term with the same orthonormality constraint. Carrying out the minimization, we arrive at the equation

$$\langle \tilde{\psi}_n | \hat{z} | \tilde{\psi}_m \rangle (z_n - z_m) = 0 \quad (3.3)$$

where  $z_n = \langle \tilde{\psi}_n | \hat{z} | \tilde{\psi}_n \rangle$ . By inspection, we see that  $\zeta$  is maximized when  $z_n = z_m$  for all  $m$  and  $n$ , corresponding to maximally delocalized states. On the other hand,  $\zeta$  is minimized when the states  $|\tilde{\psi}_n\rangle$  are the eigenkets of the position operator  $\hat{z}$  within the conduction or valence band subspace. So our problem is reduced to constructing and diagonalizing the matrix  $\langle \psi_n | \hat{z} | \psi_m \rangle$  which has the eigenvectors  $\langle \psi_n | \tilde{\psi}_i \rangle$  which provide the desired transformation given in Eq. 3.1. The eigenvalues  $z_n$  are the positions of the localized states.

In DFTB [47], the eigenstates are expanded onto a basis set of atomic orbitals

$$|\psi_n\rangle = \sum_\nu c_{n\nu} |\varphi_\nu\rangle. \quad (3.4)$$

Here  $\nu$  is summed over each orbital of each atom in the system. To evaluate the

matrix elements we use the approximation

$$\langle \psi_n | \hat{z} | \psi_m \rangle = \sum_{\mu\nu} c_{n\mu}^* c_{m\nu} \langle \varphi_\mu | \hat{z} | \varphi_\nu \rangle \approx \sum_{\mu\nu} c_{n\mu}^* c_{m\nu} S_{\mu\nu} z_{\mu\nu} \quad (3.5)$$

where  $S_{\mu\nu} = \langle \varphi_\mu | \varphi_\nu \rangle$  is the tight-binding overlap matrix and  $z_{\mu\nu}$  is the average z-value for the atoms located at sites given by the labels  $\mu$  and  $\nu$ . Once the localized states are constructed, the hopping parameters are computed as

$$t_{ij} = \langle \tilde{\psi}_i | \mathcal{H} | \tilde{\psi}_j \rangle = \sum_n \varepsilon_n \langle \tilde{\psi}_i | \psi_n \rangle \langle \psi_n | \tilde{\psi}_j \rangle \quad (3.6)$$

recalling that the quantities  $\langle \psi_n | \tilde{\psi}_i \rangle$  are determined from the transformation described above.

Now that we have described the method of calculating hoppings, starting from the all-atom calculation, we can consider the resulting effective hamiltonian. For the first, second, and third neighbors along the helix, we denote the hopping matrix elements according to the scheme shown in Fig. 3.2 which allows us to define an effective hamiltonian for our system

$$\begin{aligned} \mathcal{H} = \varepsilon \sum_n c_n^\dagger c_n &+ t_1 \sum_{n \text{ even}} (c_n^\dagger c_{n+1} + c_{n+1}^\dagger c_n) \\ &+ t_2 \sum_{n \text{ odd}} (c_n^\dagger c_{n+1} + c_{n+1}^\dagger c_n) \\ &+ t_3 \sum_n (c_n^\dagger c_{n+2} + c_{n+2}^\dagger c_n) \end{aligned} \quad (3.7)$$

where  $n$  represents the  $n^{\text{th}}$  base pair along the helical axis and we have neglected spin indices because they are unimportant for our analysis. Performing a Fourier transform on the electron creation and annihilation operators  $c_k = \frac{1}{\sqrt{N}} \sum_n e^{-ikn} c_n$  gives a hamiltonian which has coupling between momenta  $k$  and  $k + \pi/a$ . By doubling the unit cell (and reducing the Brillouin zone by a factor of two), this can finally be

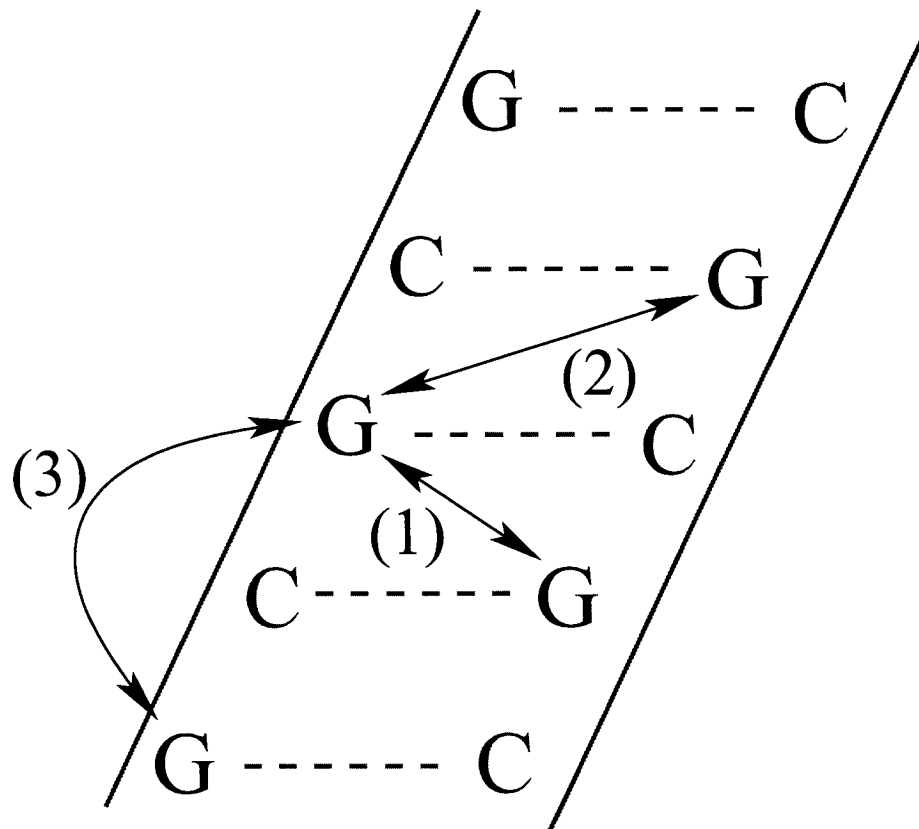


Figure 3.2: Schematic depiction of the electron hopping in poly(CG)-poly(CG) DNA for the valence band. The hopping matrix elements  $t_i$  are denoted by the indices  $(i) = (1), (2), (3)$ . For the conduction band, the hopping is similar with electrons localized on the C bases.



	valence	conduction
$\varepsilon$ (eV)	3.12	-0.09
$t_1$ (meV)	14	-0.29
$t_2$ (meV)	2.6	0.044
$t_3$ (meV)	0.091	0.26

Table 3.1: Parameters for the on-site ( $\varepsilon$ ) and hopping matrix elements ( $t_i, i = 1, 2, 3$ ), for the valence and conduction bands of unstretched poly(CG)-poly(CG) DNA.

diagonalized to obtain the eigenvalues

$$E_k^\pm = \varepsilon + 2t_3 \cos(2k) \pm \sqrt{t_1^2 + t_2^2 + 2t_1 t_2 \cos(2k)}$$

with the momentum sum carried out over the reduced Brillouin zone. Using these expressions for the band structure energies, the density of states  $\nu(\omega) = \frac{1}{N} \sum_{k,n} \delta(\omega - E_k^{(n)})$  is readily obtained.

To summarize the results of this section, we have used a density-functional theory method to calculate the electronic structure of stretched DNA. Using these detailed results, we developed a method to calculate the input parameters  $\varepsilon, t_{1,2,3}$  of the simple tight-binding hamiltonian given in Eq. 3.7 for different stretching magnitudes.

### 3.3 Electronic localization in the presence of disorder

In this section, we first discuss the calculated results for the hoppings used in Eq. 3.7, then later move on to discuss the resulting electronic localization. In Table 1 we give the calculated values we obtain for unstretched poly(CG)-poly(CG) DNA for these hopping matrix elements. For the valence and conduction states, the electron hops between nearest and next-nearest neighbor sites centered on the G and C bases

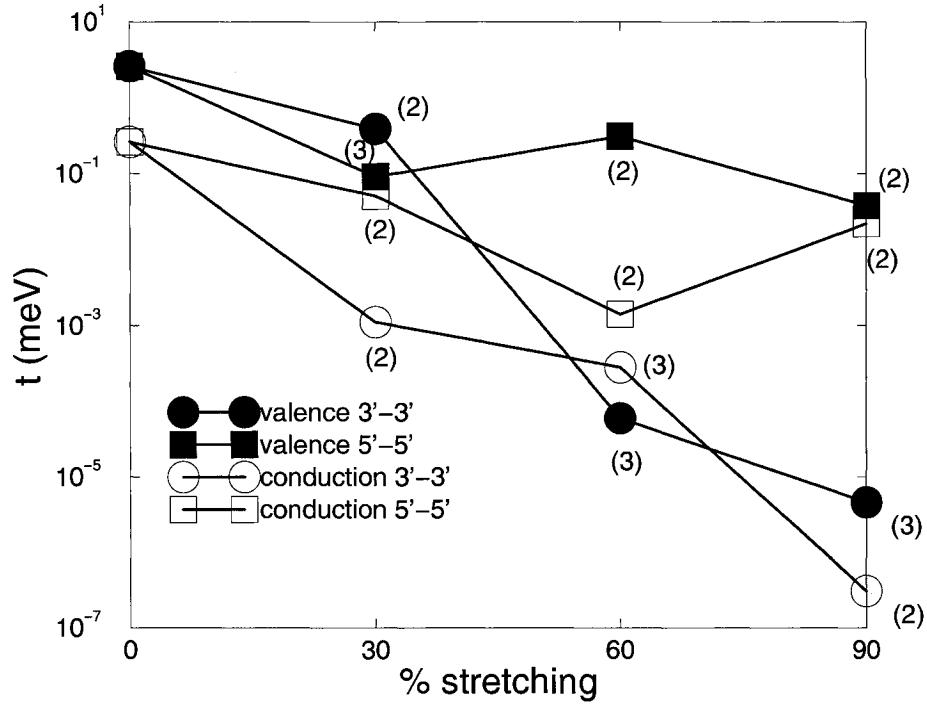


Figure 3.3: The valence and conduction band bottleneck hopping as given by Eq. 3.8 for the different modes of stretching. The dominant hopping process as defined in Fig. 3.2 is indicated in parenthesis.

respectively; matrix elements for farther hopping are much smaller in magnitude. Now consider a hole or electron injected into the valence or conduction band: if  $t_2 = t_3 = 0$  the electron will not be able to migrate along the DNA molecule even if  $t_1$  is quite large. From this simple picture, it is evident that the conductivity will be limited by the hopping of minimum magnitude with the requirement that an electron or hole must participate in this process while traversing the DNA molecule. More quantitatively, this “bottleneck” hopping is given by

$$t = \max(\min(|t_1|, |t_2|), |t_3|). \quad (3.8)$$

In Fig. 3.3 we show the bottleneck hopping calculated as a function of stretching. This indicates that hopping conductivity will dramatically decrease by several orders of magnitude upon stretching the molecule and that the hopping will decrease more from stretching in the 3'-3' mode than in the 5'-5' mode. This is due to the conformational changes induced by the different stretching modes, described earlier.

The evolution of the density of valence band states upon stretching is given in Fig. 3.4 where similar behavior is seen for the conduction band. The dramatic narrowing of the dispersion in the band structure energies as revealed in the density of states is suggestive of electronic localization [7], in this case induced by stretching. Such behavior was indeed observed in the recent experiment of Heim *et al.* [64]. In this experiment, ropes of  $\lambda$ -DNA on a substrate are overstretched by a receding meniscus technique. It was estimated that the DNA ropes are slightly positively charged, with a depletion of a few electrons per 1000 base pairs. Electrons are then injected into the DNA and the resulting localization length is measured by an electron force microscope. For the unstretched DNA, the charge is found to delocalize across the entire molecule, extending several microns. On the other hand, the charge injected into the overstretched DNA is localized, extending over a few hundred nanometers only.

To quantify the amount of localization that is expected in stretched DNA molecules, we add a term to the hamiltonian in Eq. 3.7 of the form

$$\mathcal{H}_{\text{dis}} = \sum_n U_n c_n^\dagger c_n \quad (3.9)$$

which is meant to emulate disorder arising from a variety of sources such as interaction with stray water molecules and ions or interaction with the substrate.  $U_n$  are

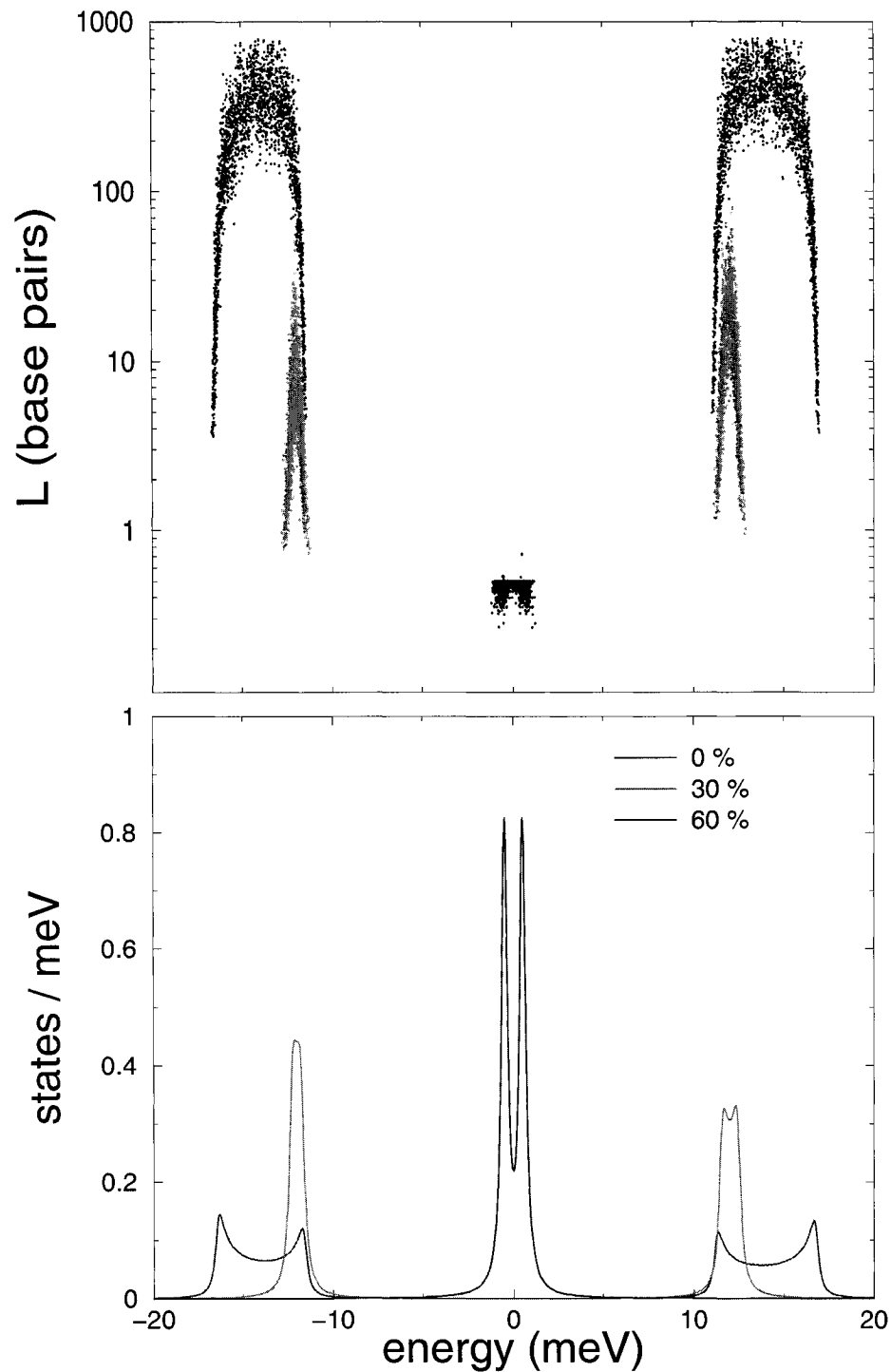


Figure 3.4: (bottom) The density of electronic states for the valence band stretched in the 3'-3' mode. For comparison, the on-site energy parameter,  $\varepsilon$ , has been set to zero. (top) The localization length  $L_i$ , defined in Eq.(3.11), computed for each eigenstate with disorder strength  $\gamma = 0.3$  meV.

uncorrelated random energy variations chosen according to a Gaussian distribution of zero mean and width  $\gamma$

$$P(U) = \frac{1}{\gamma\sqrt{2\pi}} \exp\left(-\frac{U^2}{2\gamma^2}\right). \quad (3.10)$$

Once the disorder hamiltonian is constructed with a specific set of random onsite energies, by direct diagonalization we find the eigenstates  $|\psi_i\rangle$  of  $\mathcal{H} + \mathcal{H}_{\text{dis}}$  and then calculate the localization length defined as

$$L_i = \sqrt{\langle\psi_i|\hat{n}^2|\psi_i\rangle - \langle\psi_i|\hat{n}|\psi_i\rangle^2} \quad (3.11)$$

where  $\hat{n} = \sum_n n c_n^\dagger c_n$ . We note that for a single-hopping model with weak disorder, the localization length scales as  $L \sim (t/\gamma)^2$  for electrons near the middle of the band [153], but the more complicated effective hamiltonian considered here is not amenable to simple analytic treatment. In Fig. 3.4 we show the localization length for each eigenstate for a 1500 base-pair DNA strand for different amounts of stretching. For the disorder strength we take  $\gamma = 0.3$  meV which is much smaller than the band width of the unstretched DNA, but becomes comparable to the band width as the molecule is stretched. The magnitude of such variations in onsite energies are in line with those produced by the dipole potential terms, produced for instance by a stray water molecule situated on the substrate roughly 15 Å away from the bases. However, we note that changing  $\gamma$  in either way by an order of magnitude will not affect our qualitative picture. Note that the localization length is not a strict function of the energy, as it depends on the disorder near where a given state happens to be localized. As the molecule is stretched, the localization length dramatically decreases until (for 60% stretching) the eigenstates are localized on single base pairs. This

change of localization length by up to three orders of magnitude is in line with the experimental observations of Heim *et al.* [64] discussed above.

### 3.4 Conclusion

In conclusion, we have described and implemented a bottom-up method to derive effective tight-binding models describing the dynamics of conduction and valence electrons in stretched DNA, starting from an all-atom quantum mechanical calculation. With these models, we find that stretching dramatically narrows the band widths close to the Fermi energy. As a result, adding a random potential in line with that from stray water molecules will cause the electronic states to become localized as the molecule is stretched.

# Chapter 4

## Superconductivity and charge-density wave instabilities in carbon nanotubes

### 4.1 Introduction

It has been over a decade since the discovery of carbon nanotubes (CNTs) [72] and the interest level in these systems continues to be high. The majority of theoretical work on CNTs focuses on understanding the effects of the electron-electron interactions using the celebrated Luttinger liquid theory.[43] Experimental observation of superconductivity in ropes of nanotubes [86] and small-radius nanotubes in a zeolite matrix [152] has also motivated theoretical studies of the electron-phonon interactions (EPI), including the analysis of charge density wave (CDW) [113, 70, 140, 42] and superconducting (SC) [12, 141, 20, 54, 80] instabilities. In this work we study the

electron-phonon interactions in CNTs and discuss possible instabilities to the CDW and SC orders. Our approach provides reliable parameters for the effective Hamiltonians we use in contrast to the Luttinger liquid treatments where obtaining such accurate quantities is quite difficult.

A conventional starting point for discussing the electron-phonon interaction in solids is the Fröhlich Hamiltonian [139]

$$\begin{aligned} \mathcal{H} = & \sum_{k\tau\sigma} \varepsilon_{k\tau} c_{k\tau\sigma}^\dagger c_{k\tau\sigma} + \sum_{q\mu} \Omega_{q\mu}^0 (a_{q\mu}^\dagger a_{q\mu} + \frac{1}{2}) \\ & + \sum_{k\tau k'\tau'\sigma\mu} g_{k\tau k'\tau'\mu} c_{k\tau\sigma}^\dagger c_{k'\tau'\sigma} (a_{q\mu} + a_{-q\mu}^\dagger). \end{aligned} \quad (4.1)$$

Here  $c_{k\tau\sigma}^\dagger$  creates an electron with quasimomentum  $k$  in band  $\tau$  with spin  $\sigma$ ,  $a_{q\mu}^\dagger$  creates a phonon with lattice momentum  $q$  and polarization  $\mu$ , and  $q = k - k'$  modulo a reciprocal lattice vector. The energies of electron quasiparticles and phonons (in the absence of EPC) are given by  $\varepsilon_{k\tau}$  and  $\Omega_{q\mu}^0$  respectively. The EPC vertex is given by

$$g_{k\tau k'\tau'\mu} = \sqrt{\frac{1}{2\Omega_{q\mu}^0 M N N_c}} M_{k\tau k'\tau'\mu} \quad (4.2)$$

with

$$M_{k\tau k'\tau'\mu} = N \langle \psi_{k\tau} | \sum_i \frac{\partial V}{\partial \mathbf{R}_{0i}} \cdot \hat{\epsilon}_{q\mu}(i) | \psi_{k'\tau'} \rangle. \quad (4.3)$$

Here  $|\psi_{k\tau}\rangle = c_{k\tau}^\dagger |0\rangle$  is a quasistationary electron state in band  $\tau$  with quasimomentum  $k$ ,  $\hat{\epsilon}_{q\mu}(i)$  is the phonon polarization vector on atom  $i$  in the unit cell,  $N_c$  is the number of atoms per unit cell,  $M$  is the mass of a single C atom,  $N$  is the total number of unit cells in the system, and  $\partial V / \partial \mathbf{R}_{0i}$  is the derivative of the crystal potential with respect to the ion position  $\mathbf{R}_{0i}$ .

A common approach to obtaining parameters of the Hamiltonian Eq. (4.1) for the CNTs is the zone-folding method (ZFM) [135]. The essence of this method is to



take the electron band structure and the phonon dispersion for graphene and quantize momenta in the direction of the wrapping. The main results of such a procedure may be summarized as follows. The only bands crossing the Fermi level in graphene are the bonding and the antibonding combinations of the atomic  $p_z$  orbitals. Hence, the zone-folding method predicts that these are the only bands which may cross the Fermi level in carbon nanotubes. The condition for the quantized momenta to cross the Dirac points of the graphene gives the condition for the (N,M) CNT to be metallic:  $N - M$  should be divisible by 3. The ZFM also predicts that the electron-phonon coupling in the CNTs should be dominated by the in-plane optical modes. This follows from the fact that the latter have the largest effect on the overlaps between the  $p_z$  orbitals of the neighboring carbon atoms.

While the ZFM was shown to provide a quantitatively accurate description of the larger radius nanotubes, it is expected to fail as the radius of the nanotubes is decreased and the curvature of the C-C bonds becomes important. Determining the band structure, the phonon dispersion, and the electron-phonon coupling of the small radius CNTs requires detailed microscopic calculations. In this paper we use the empirical tight-binding model [110] to provide such analysis for three types of small-radius nanotubes: (5,0) with the diameter 3.9 Å, (6,0) with the diameter 4.7 Å, and (5,5) with the diameter 6.8 Å. We find that the large curvature of the C-C bonds leads to qualitative changes in the band structure of the (5,0) and (6,0) nanotubes. Previous work on the band structure of small-radius carbon nanotubes can be found in Refs. [16, 62, 81, 150, 98, 99, 104, 174]. For example, the (5,0) CNT becomes metallic from strong hybridization between the  $\sigma$  and  $\pi$  bands (see Fig. 4.4).

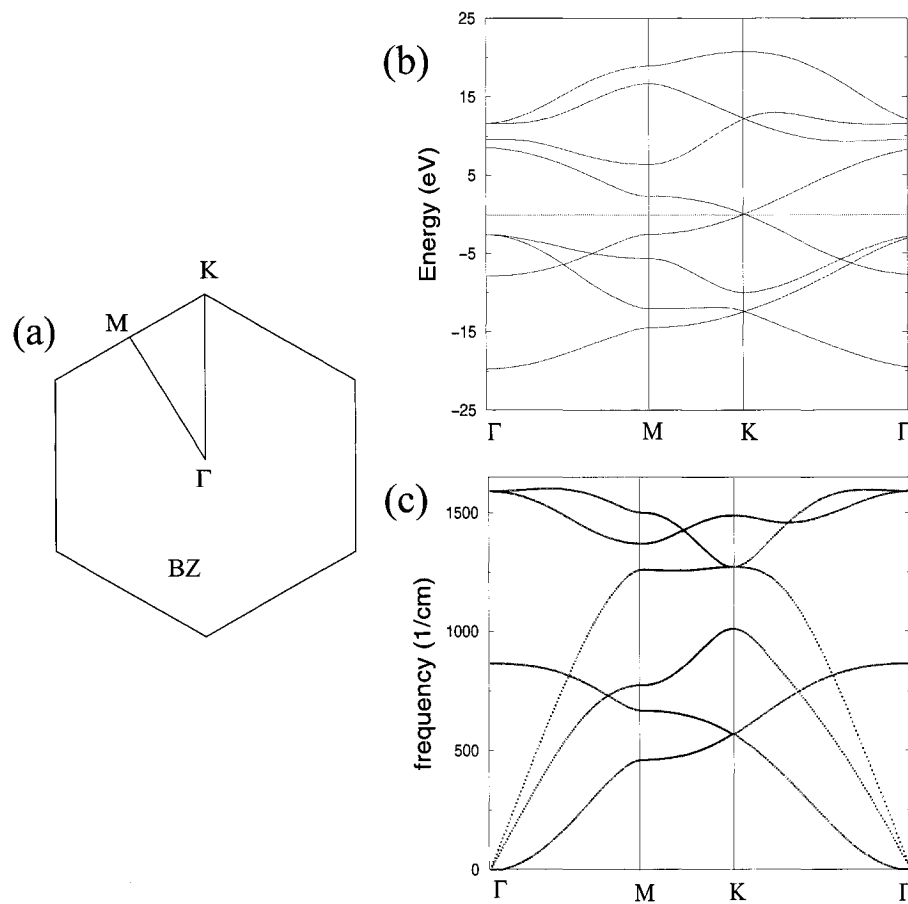


Figure 4.1: The first Brillouin zone (a), electronic band structure (b), and phonon dispersion (c) of graphene.

Frequencies of the phonon modes in small radius CNTs are also strongly renormalized from their values in graphene. Not only does the out-of-plane acoustic mode become a finite frequency breathing mode, [135] but even the optical modes change their energy appreciably (see e.g. Fig. 4.7). Finally, the electron-phonon coupling changes qualitatively in the small-radius CNTs. It is no longer dominated by the in-plane optical modes but by the out-of-plane optical modes which oscillate between the  $sp_2$  bonding of graphene and the  $sp_3$  bonding of diamond (see discussion in Sec. 4.6). We find that the strong effects of the CNT curvature decrease rapidly with increasing the tube radius. Already for the (5,5) nanotubes the ZFM gives a fairly accurate description of the band structure as well as the electron-phonon interactions.

Determining parameters of the Fröhlich Hamiltonian for a one-dimensional system is not as straightforward as for two and three-dimensional metals. Traditional methods for analyzing EPI from first-principles calculations are mean-field and, therefore, suffer from instabilities intrinsic to one-dimensional systems. In particular, the frozen-phonon approximation, which is commonly used to determine the phonon frequencies,  $\Omega_{q\mu}^0$ , in Eq. (4.1) gives imaginary frequencies close to the nesting wave vector  $q = 2k_F$ . This is the result of the giant Kohn anomaly, [87] which corresponds to the Peierls instability of the one-dimensional electron-phonon system [123]. An important result of our paper is that we developed a new formalism, which combines the frozen-phonon approximation with the Random-Phase Approximation (RPA) analysis of the EPI. This allows us to extract effective non-singular parameters of the Fröhlich Hamiltonian from first-principles calculations or from the empirical tight-binding model. This technique should be applicable to many systems other than carbon nanotubes.

After determining parameters of the Fröhlich Hamiltonian Eq. (4.1) for the (5,0), (6,0), and (5,5) CNTs we discuss possible superconducting and charge-density wave instabilities in these systems. We find that neglecting the residual Coulomb interaction leads to much stronger CDW instabilities in all three cases (in such analysis Coulomb interaction is included only at the mean-field level via the energy of the single-particle quasi-stationary states,  $\varepsilon_{k\tau}$ ). In the mean-field approximation we find the onset of the Peierls instability at temperatures 160, 5, and  $10^{-14}$  K for (5,0), (6,0), and (5,5) CNTs respectively. However, including the Coulomb interactions at the RPA level [97] can lead to a stronger suppression of the CDW transition temperatures,  $T_{\text{CDW}}$ , than the superconducting  $T_{\text{SC}}$ . For instance, we find by using the model Coulomb interaction of Ref. [44] that for the (5,0) CNT, the CDW transition is suppressed to very low temperatures while superconductivity becomes the dominant phase with transition temperature of  $T_{\text{SC}} \approx 1$  K.

This chapter is organized as follows. In Sec. 4.2 we discuss our method for extracting parameters for the one-dimensional Fröhlich Hamiltonian. We then apply this method to the (5,0), (6,0), and (5,5) CNTs in Sec. 4.3. In Sec. 4.4, we use the constructed Hamiltonian for these CNTs to study their instabilities toward superconductivity and charge-density wave states. The effect of introducing the residual Coulomb interacting between electrons is covered in Sec. 4.5. Finally all of the results are discussed and summarized in Sec. 4.6.

## 4.2 Extraction parameters of the effective Fröhlich hamiltonian from the first principles calculations

Now we discuss our methods for calculating input parameters to the Fröhlich Hamiltonian Eq. (4.1) for the representative nanotubes. Our analysis relies on the empirical tight-binding model [110] but it is easily amenable to any density-functional theory [67, 88] treatment of the system.

### 4.2.1 Band structure

To compute the electronic structure of the CNTs we study, we use the NRL tight-binding method [110] which has been tested and provided accurate results on a variety of materials. In this method, the Slater-Koster tight-binding matrix elements are parametrized and are fit to reproduce the first-principles density-functional band structures and total energies, with around 70 adjustable parameters per element.

We study the (5,0), (6,0), and (5,5) CNTs which are shown in Figs. 4.4, 4.8, and 4.10. The smallest possible unit cells for these CNTs contain 20, 24, and 20 atoms respectively. These CNTs are relaxed by minimizing their total energy per unit cell with respect to the atomic coordinates using 35 k-points in the first Brillouin zone. Matrix elements between neighboring atoms of up to 5.5 Å were used, which is used for the parameterization of Carbon in the NRL tight-binding method. The calculations were performed on an orthorhombic lattice with spacing between parallel CNTs of 16 Å, a distance sufficiently large to ensure negligible dispersion from inter-

tube hopping. Once the CNTs are relaxed, the band structure is calculated.

### 4.2.2 The phonon modes

To calculate the electron-phonon coupling vertices and the phonon frequencies which will be discussed in the subsequent sections, one needs to have the ionic displacements corresponding to the normal vibrational modes of the CNT. As pointed out previously, [136, 135] we find that it is typically sufficient to use the zone-folded modes of a graphene sheet, even for the small-radius CNTs we study as will be discussed below.

Following the method used in the book of Saito *et al.*, [135] we have computed the  $60 \times 60$  dynamical matrix of a (5,0) CNT and in Fig. 4.2 we compare the resulting phonon dispersions with the zone-folding results. The ionic displacement modes obtained by the two different methods are very similar except for a few special cases. For instance, the zone-folding results give three acoustic modes which correspond to translating the graphene sheet in different directions. Upon rolling the graphene sheet, these modes get mapped to two acoustic modes corresponding to rotation about the CNT axis and translation along the CNT axis and the optical breathing mode. Conversely, diagonalizing the dynamical matrix of the CNT gives four acoustic modes corresponding to translations in three directions and the rotating mode (actually using the method of Ref. [135], one obtains a small spurious frequency for the rotating mode as pointed out in this reference). Upon unrolling the CNT to the graphene sheet, the rotating mode and the mode corresponding to translation along the CNT axis will become acoustic modes of the graphene sheet. However, the two CNT trans-

lational modes which are perpendicular to the CNT axis will get mapped to ionic displacements which are not eigenmodes of the graphene sheet which are mixtures of in-plane and out-of-plane oscillations. In addition, using the dynamical matrix of the CNT, we find that there is mixing between the breathing and stretching modes around  $k = 0.3$ . In this vicinity, there is level repulsion from the lifting of the degeneracy of these modes. Away from this point, the modes are, to a good approximation, decoupled.

In our analysis of the electron-phonon coupling we use the displacements obtained from the zone-folding method to simplify the calculations, as well as to give a clear conceptual picture. We then check that none of the important electron-phonon couplings come from any of the few graphene modes for which the zone-folding method breaks down.

### 4.2.3 The electron-phonon coupling vertices

The electron-phonon coupling (EPC) matrix in Eq. (4.3) can be evaluated by using the finite difference formula

$$M_{k\tau k'\tau'\mu} = \frac{1}{u} \langle \psi_{k\tau} | (V_{q\mu} - V_0) | \psi_{k'\tau'} \rangle \quad (4.4)$$

where  $V_{q\mu}$  and  $V_0$  are the perturbed and the unperturbed lattice potentials respectively and  $u$  is the magnitude of the displacement. A method for calculating the expression (4.4) with a plane-wave basis set was previously developed [93]. In this paper we extend this procedure to tight-binding models. We introduce the standard tight-

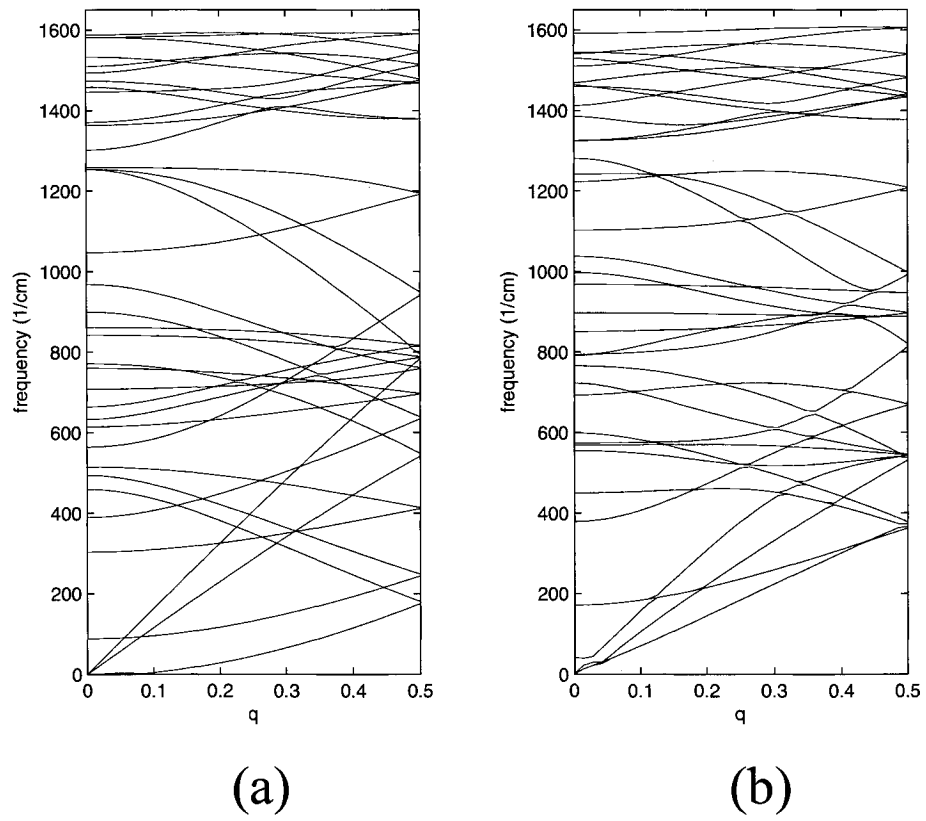


Figure 4.2: The phonon dispersions of a (5,0) CNT determined by (a) the zone-folding method and (b) diagonalizing the full dynamical matrix of the CNT.



binding notation

$$|\psi_{k\tau}\rangle = \sum_{il} A_{k\tau il} |\chi_{kil}\rangle \quad (4.5)$$

$$|\chi_{kil}\rangle = \frac{1}{\sqrt{N}} \sum_n e^{ik \cdot R_n} |\phi_{nil}\rangle. \quad (4.6)$$

Here  $|\phi_{ni}\rangle$  are the electron states for isolated carbon atoms,  $n$  runs over unit cells,  $i$  runs over basis vectors in the unit cell, and  $l$  runs over orbital type. We find (for details, see Appendix A.1)

$$M_{k\tau k'\tau'\mu} = \frac{1}{u} \sum_{il i'l'} A_{k\tau il}^* \langle \chi_{kil}^{q\mu} | (\mathcal{H}^{q\mu} - E_F) | \chi_{k'i'l'}^{q\mu} \rangle A_{k'\tau' i'l'}. \quad (4.7)$$

This expression can be computed by evaluating the tight-binding Hamiltonian and overlap matrices for the distorted lattice, evaluating the coefficients  $A_{ki}$  and  $A_{k'i'}$  of the wave functions for the undistorted lattice, and performing the above sum.

In all the calculations presented in this paper we used the ZFM to find phonon eigenvectors in the nanotubes starting from the phonon eigenvectors in graphene [135]. The latter have been obtained using the  $6 \times 6$  dynamical matrix of graphene given in Ref. [78]. We emphasize that we use the ZFM only to find the phonon eigenvectors in small nanotubes, but not the phonon frequencies. The frequencies are affected strongly by the CNT curvature, and should be computed directly. This is discussed in detail in Sec. 4.2.4 and Sec. 4.3.

#### 4.2.4 Phonon frequencies

A standard method of calculating the bare phonon frequencies  $\Omega_{q\mu}^0$  in Eq. (4.1) is the frozen-phonon approximation (FPA) [171]. In this approach

$$\Omega_{q\mu} = \frac{1}{u\sqrt{MN_c}} \sqrt{\Delta E_{\cos}(q) + \Delta E_{\sin}(q)} \quad (4.8)$$

Figure 4.3: The phonon propagator evaluated within the RPA.

where  $u$  is the amplitude of the displacement, and  $\Delta E_{\cos}(q)$  and  $\Delta E_{\sin}(q)$  are the energy differences per unit cell between the distorted and equilibrium lattice structures where the distortion corresponds to the real and imaginary parts of  $\delta \mathbf{R}_{ni} = ue^{iqR_n} \hat{e}_{q\mu}(i)$  respectively. When we apply this procedure to one-dimensional CNTs, we find that  $\Delta E_{\cos}(q) + \Delta E_{\sin}(q)$  becomes negative around certain wave vectors (see e.g. Fig. 4.7). A closer inspection shows that such anomalous softening always corresponds to one of the  $2k_F$  wave vectors of the electron bands indicating the presence of the giant Kohn anomaly.

It is important to realize that the divergence of  $\Omega_{q\mu}$  obtained in the FPA does not imply the divergence of  $\Omega_{q\mu}^0$  in the Fröhlich Hamiltonian Eq. (4.1). The frequencies  $\Omega_{q\mu}$  are calculated *after* the electron-phonon interaction in Eq. (4.1) have been included, which gives anomalous softening at  $2k_F$  due to the well-known Peierls instability of electron-phonon systems in 1d. In two and three dimensional systems renormalization of the phonon frequency by electrons in the conduction band is typically negligible. So, one can use phonon energies obtained in the FPA as a direct input into the Fröhlich Hamiltonian. By contrast, nesting of the one-dimensional Fermi surfaces, leads to dramatic renormalization of the phonon dispersion by electrons in the conduction band.

To extract the bare phonon frequency  $\Omega_{q\mu}^0$  from the numerically computed  $\Omega_{q\mu}$ , we

point out a connection between the FPA and the RPA for the Fröhlich Hamiltonian. For negligible interband coupling (this condition is satisfied for all modes showing the giant Kohn anomaly, which we discuss in this paper) Dyson's equation for the phonon propagator  $D(q, i\nu_m)$ , as shown in Fig. 4.3 is given by

$$D_\mu(q, i\nu_m) = D_{0\mu}(q, i\nu_m) (1 + \Pi_\mu(q, i\nu_m) D_\mu(q, i\nu_m)). \quad (4.9)$$

Here  $\nu_m = 2\pi mT$  are the bosonic Matsubara frequencies and

$$D_{0\mu}(q, i\nu_m) = \frac{2\Omega_{q\mu}}{(i\nu_m)^2 - (\Omega_{q\mu}^0)^2} \quad (4.10)$$

is the non-interacting phonon Green's function. The phonon self-energy evaluated in the RPA is given by

$$\Pi_\mu(q, i\nu_m) = 2T \sum_{np\tau} |g_{p\tau p+q\tau\mu}|^2 G_{0\tau}(p+q, i\omega_{m+n}) G_{0\tau}(p, i\omega_n) \quad (4.11)$$

where non-interacting electronic Green's functions are given by  $G_{0\tau}(p, i\omega_n) = (i\omega_n - \varepsilon_{p\tau})^{-1}$  and  $\omega_n = \pi(2n+1)T$  for integer  $n$  are the fermionic Matsubara frequencies.

Summing over  $n$ , we obtain for Eq. (4.11)

$$\Pi_\mu(q, i\nu_m) = 2 \sum_{\tau} |g_{q\tau\mu}|^2 \chi_{0\tau}(q, i\nu_m) \quad (4.12)$$

where the bare susceptibility is given by

$$\chi_{0\tau}(q, i\nu_m) = \sum_p \frac{f(\varepsilon_{p\tau}) - f(\varepsilon_{p+q\tau})}{i\nu_m + \varepsilon_{p\tau} - \varepsilon_{p+q\tau}}. \quad (4.13)$$

with  $f(\varepsilon_{p\tau}) = (1 + e^{\beta\varepsilon_{p\tau}})^{-1}$  being the Fermi-Dirac distribution function.

The poles of the phonon Green's function  $\Omega_{q\mu}$  (we put  $i\nu_m \rightarrow \Omega_{q\mu}$  in  $D_\mu(q, i\nu_m)$ ), which give the dressed phonon frequencies, will satisfy the equation

$$(\Omega_{q\mu})_{\text{RPA}}^2 = (\Omega_{q\mu}^0)^2 + 2\Omega_{q\mu}^0 \Pi_\mu(q, \Omega_{q\mu}). \quad (4.14)$$

Due to the large energy difference between electrons and phonons, it is typically a good approximation to set  $\Omega_{q\mu} \rightarrow 0$  in  $\Pi_\mu(q, \Omega_{q\mu})$ . This approximation results in an expression that can be derived by doing stationary second-order perturbation theory to obtain the change in energy due to the presence of the phonon. That is, setting  $\Omega_{q\mu} \rightarrow 0$  in  $\Pi(q, \Omega_{q\mu})$  corresponds to the frozen-phonon approximation

$$(\Omega_{q\mu})_{\text{FPA}}^2 = (\Omega_{q\mu}^0)^2 + 2\Omega_{q\mu}^0 \Pi_\mu(q, 0). \quad (4.15)$$

We can typically approximate well the quasiparticle energy by a plane-wave state with given effective mass  $m^*$ . Then, by incorporating the FPA, at zero temperature the integral in Eq. (4.13) can be done which will enable us to obtain

$$(\Omega_{q\mu})_{\text{FPA}}^2 = (\Omega_{q\mu}^0)^2 + \sum_\tau |M_{2k_{F\tau}\mu}|^2 \frac{2m^*a}{\pi M N_c k_{F\tau}} \log \left| \frac{2k_{F\tau} - q}{2k_{F\tau} + q} \right|. \quad (4.16)$$

This expression explicitly shows the logarithmic divergences in the phonon dispersion at the nesting wave vectors of the Fermi surface. This is the famous Peierls instability to a CDW state. Our procedure for determining the elusive undressed frequencies is then as follows. We take  $\Omega_{q\mu}$  obtained from the FPA and fit them with the expression Eq. (4.16) using  $\Omega_{q\mu}^0$  as an adjustable parameter. The coefficients of the log divergences at the nesting wave vectors of the Fermi surface are fixed by the effective masses  $m_\tau^*$  and  $k_{F\tau}$  (known from the band structure) and the computed EPC matrix elements  $M_{2k_{F\tau}\mu}$ . In all cases we found excellent agreement of the calculated FPA frequencies with Eq. (4.16) in the vicinity of the singular points, which provides a good self-consistency check for our analysis.

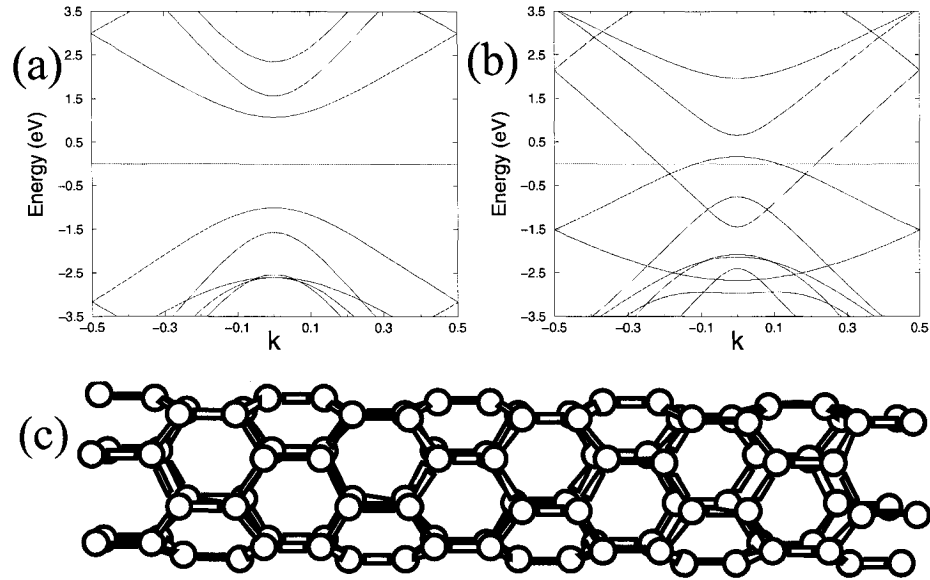


Figure 4.4: The band structure of the (5,0) CNT obtained through zone-folding (a) and calculated directly (b) along with the atomic structure (c).

## 4.3 Results for representative nanotubes

### 4.3.1 (5,0) nanotube

The zig-zag (5,0) CNT has a diameter of around 3.9 Å making it close to the theoretical limit [124]. Nanotubes of this size have been experimentally realized through growth in the channels of a zeolite host [152]. Through the Raman measurement of the frequency of the radial breathing mode, the (5,0) CNT is thought to be a likely candidate structure for these experiments [98].

We first compute the band structure of this tube by using the zone-folding method [135]. To do this, we use the band structure of graphene, which is shown in Fig. 4.1, computed by using the NRL tight binding method. Shown in this figure are four valence bands and four conduction bands, coming from the three  $sp_2$  and one  $p_z$

bonding and antibonding states respectively. There is a degeneracy between the  $p_z$  bonding and antibonding states at the Fermi energy at the  $K$  point in the first Brillouin zone which accounts for the semimetallic behavior of graphene. The zone-folding band structure of the (5,0) CNT is shown in the right of Fig. 4.4. Since  $5/3$  is not an integer, zone-folding predicts this CNT to be semiconducting.

Fig. 4.4 (b) shows the band structure of the (5,0) CNT calculated directly by using a unit cell of 20 atoms. One sees that there are significant qualitative differences between the two band structures, one being that the directly computed band structure predicts metallic behavior. The inner band (with smaller Fermi point  $k_F^A$ ) is doubly degenerate while the outer band (with larger Fermi point  $k_F^B$ ) is nondegenerate. The strong curvature effects causes hybridization between  $\sigma$  and  $\pi$  bands, pushing them through the Fermi energy and therefore making the tube metallic. Furthermore, for the (5,0) CNT, we see that inner band is close to the Van Hove singularity at  $k = 0$ , which produces a large density of states at the Fermi energy. The calculated density of  $\nu(0) = 0.16$  states/eV / C atom is around a factor of five larger than that of larger radius metallic armchair CNTs.

After the band structure is calculated, we consider all possible scattering processes of electrons between Fermi points  $-k_F^B$ ,  $-k_F^A$ ,  $k_F^A$ , and  $k_F^B$  due to phonons with wave vectors  $q$  that satisfy the momentum conservation condition. As a starting point for the phonon spectrum, we use the dynamical matrix of Jishi *et al.* [78] which uses a fourth nearest-neighbor model, and we employ the zone-folding method. The reproduced phonon dispersion of graphene is shown in Fig. 4.1. For a given process, we calculate the coupling for all of the  $3 \times N_c$  distinct phonon modes where  $N_c = 20$  is

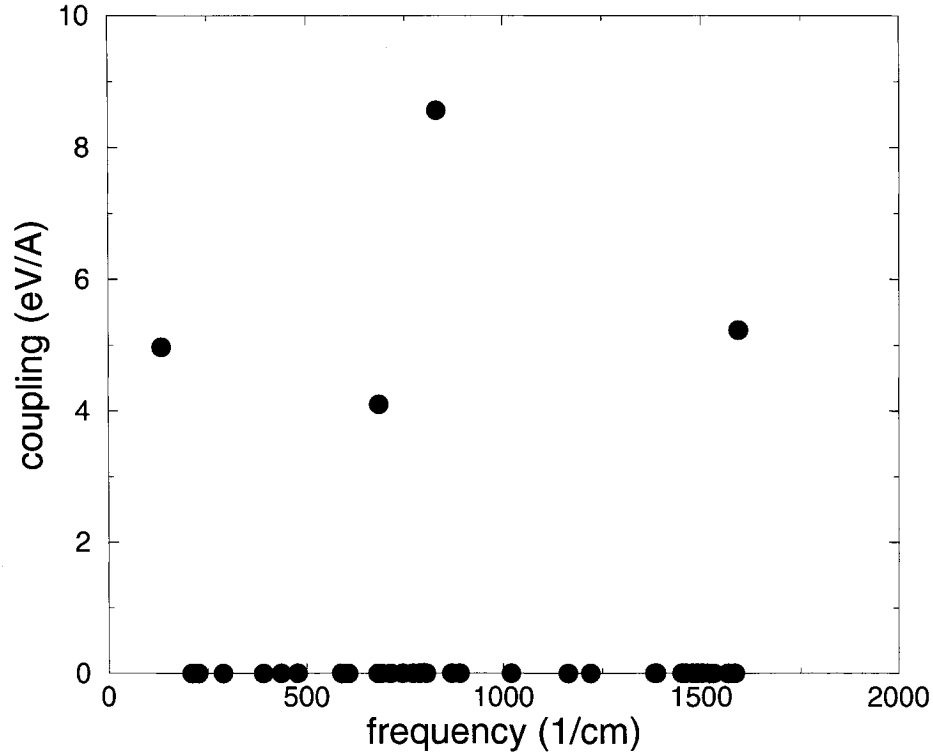


Figure 4.5: The coupling  $M_{kk'}$  for the outer band  $2k_F^B$  process for each of the  $3 \times 20 = 60$  phonon modes respectively vs. graphene frequency.

the number of atoms per unit cell. Shown in Fig. 4.5 is an example of the outcome for one of these calculations. Shown is the coupling for the outer band  $2k_F^A$  processes vs. graphene frequency. One can immediately see that most couplings vanish which can be explained by symmetry of the electronic wave functions and the phonon modes.

To keep this paper concise, we cannot present all of the coupling results for each scattering process. Instead, we show the most dominant couplings. These dominant couplings were found to be from intraband  $2k_F$  processes. The largest couplings for the (5,0) CNT occur for phonons along the  $\Gamma M$  line of graphene at the appropriate wave vector corresponding to the particular  $2k_F$ . For the inner band, the largest

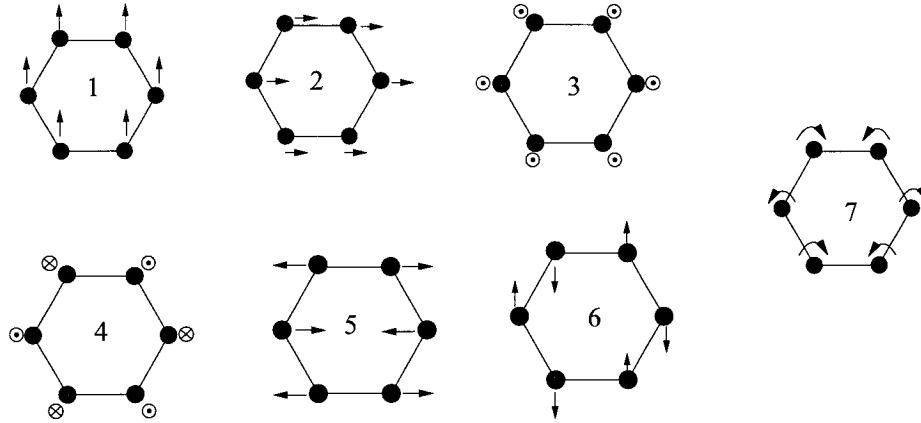


Figure 4.6: 1-6: The phonon modes at the  $\Gamma$  point in the first Brillouin zone of graphene. 7: An in-plane optical phonon mode at the  $K$  point of the first Brillouin zone of graphene. The out-of-plane optical mode 4 is the leading cause of the CDW instability in the (5,0) and (6,0) CNTs.

couplings, in descending order, occur for the out-of-plane optical mode, the radial breathing mode, and the in-plane acoustic stretching mode. For the outer (with larger  $k_F$ ) band, the dominant couplings occur for the out-of-plane optical, an in-plane optical, the radial breathing, and in-plane stretching modes. These results are summarized in Fig. 4.6 and Table 4.1. Although the magnitude of the dominant coupling matrix element for the outer band is larger than that of the inner band, the inner band processes are significantly more important in the study of instabilities because their contribution to the total density of states at the Fermi energy is significantly larger than that of the outer band. This is due to the small Fermi velocity of the inner band and its degeneracy.

It is interesting to note that the phonons that have the strongest coupling to electrons at the Fermi surface are out-of-plane modes. This is different than intercalated graphene where in-plane phonon modes are responsible for superconductivity.[40] The fact that the out-of-plane modes are the most important for this CNT are presumably



(5,0)	mode	$\omega_q^{graph}$ (cm <sup>-1</sup> )	$M_{kk'}$ (eV/Å)
$2k_F^A$	4	853	5.55
	3	39	4.46
	5	1588	4.24
$2k_F^B$	4	829	8.56
	5	1593	5.23
	3	133	4.97
	2	684	4.10

Table 4.1: Calculated values for the dominant coupling processes for the (5,0) CNT. The numbering scheme here corresponds to that given in Fig. 4.6.  $2k_F^A$  and  $2k_F^B$  correspond to inner and outer band processes respectively. Phonon frequencies are given for graphene.

due to the large curvature effects. For instance, we find that the bond angles of the relaxed (5,0) CNT structure (having the values of 119.4° and 111.9°) are intermediate between the  $sp_2$  bond angle (found in graphene) of 120° and the  $sp_3$  bond angles (found in diamond) of 109.4°.

Now we calculate the CNT phonon frequencies by using the frozen-phonon approximation with the eigenvectors from graphene. The circles shown in Fig. 4.7 are the frequencies obtained for phonon modes along the  $\Gamma M$  line of graphene for the out-of-plane optical mode which was found to be the most important mode. First, we see that the calculated FPA frequencies are significantly lower than the corresponding ones in graphene. This can be understood as follows. The strong curvature of the nanotube changes the C-C bonds so that they are in an intermediate regime between the  $sp_2$  bonding (found in graphene) and  $sp_3$  bonding (found in diamond). The out-of-plane optical mode oscillates between these two bonding configurations and is therefore significantly softened. Next, we notice that there are divergences at  $q = 2k_F^A$  and  $q = 2k_F^B$ . This result is the giant Kohn anomaly.

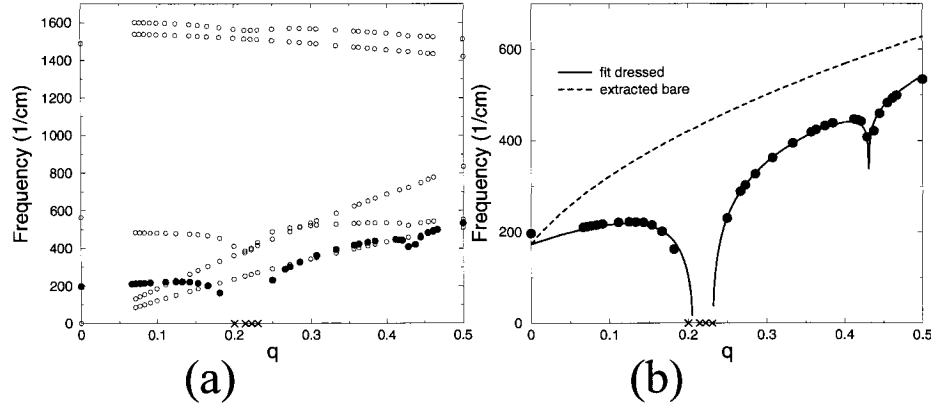


Figure 4.7: (a): Phonon dispersion for the (5,0) CNT along the  $\Gamma M$  line of graphene. The X's denote values for which the frozen-phonon approximation gave imaginary frequencies for the out-of-plane optical mode in the vicinity of  $2k_F^A$ . (b): The mode showing the most softening fit to the RPA expression.

To extract the bare phonon frequency of the Fröhlich Hamiltonian Eq. 4.1 for the (5,0) CNT we follow the procedure discussed in Sec. 4.2.4. The dressed phonon frequencies are given by

$$\begin{aligned}
 (\Omega_{q\mu})^2 = (\Omega_{q\mu}^0)^2 &+ D_A \log \left| \frac{2k_F^A - q}{2k_F^A + q} \right| \\
 &+ D_B \log \left| \frac{2k_F^B - q}{2k_F^B + q} \right|
 \end{aligned} \quad (4.17)$$

where

$$D_A = |M_{2k_F^A}|^2 \frac{2m_A^* a}{\pi M N_c k_F^A} \quad (4.18)$$

and

$$D_B = |M_{2k_F^B}|^2 \frac{m_B^* a}{\pi M N_c k_F^B}. \quad (4.19)$$

All of the quantities needed to calculate the coefficients  $D_A$  and  $D_B$  have been obtained already. We assume that the bare phonon frequencies are fit well by the form  $(\Omega_{q\mu}^0)^2 = a_0 + a_1 q + a_2 q^2$ . We then use  $a_0, a_1$  and  $a_2$  as fitting parameters to fit our expression for  $\Omega_q$  to the calculated FPA frequencies. Doing this thereby enables us to extract the

important bare frequency dispersion  $\Omega_q^0$  which is shown in Fig. 4.7. Extracting these bare frequencies  $\Omega_q^0$  allows us to calibrate the effective Frölich Hamiltonian Eq. (4.1) which will be used to study instabilities of the electron-phonon system. With our previously calculated quantities, we obtain  $D_A = (219 \text{ cm}^{-1})^2$  and  $D_B = (146 \text{ cm}^{-1})^2$ . Using these values we thereby extract  $\Omega_{q=2k_F^A}^0 = 433 \text{ cm}^{-1}$ .

### 4.3.2 (6,0) nanotube

The band structure of the (6,0) CNT was considered extensively by Blase *et al.* in Ref. [16]. This tube has a slightly larger diameter of 4.7 Å. The zone-folding band structure of this CNT is shown in the left of Fig. 4.8. As is typical of metallic zig-zag tubes, there are two bands crossing at  $k = 0$  at the Fermi energy. The band structure directly computed with 24 atoms in the unit cell is shown in the right of Fig. 4.8. As discussed before [16], these band structures differ qualitatively which is a result of the hybridization of the  $sp_2$  and  $p_z$  bands. Here the inner band (with smaller  $k_F^B$ ) is nondegenerate and originates from the  $p_z$  bands in graphene while the outer band (with larger  $k_F^A$ ) is degenerate and originates from the  $sp_2$  bands in graphene.

The coupling matrix elements for the (6,0) CNT were computed and the coupling for the most dominant modes are shown in Fig. 4.6 and Table 4.2. The dominant inner band couplings were for intraband processes and are, in descending order, to the out-of-plane optical and an in-plane optical. The dominant outer band couplings processes were found to be the out-of-plane optical mode, an in-plane optical mode, the radial breathing mode, and the in-plane acoustic stretching mode.

Using the same procedure as was used for the (5,0) CNT in the previous section

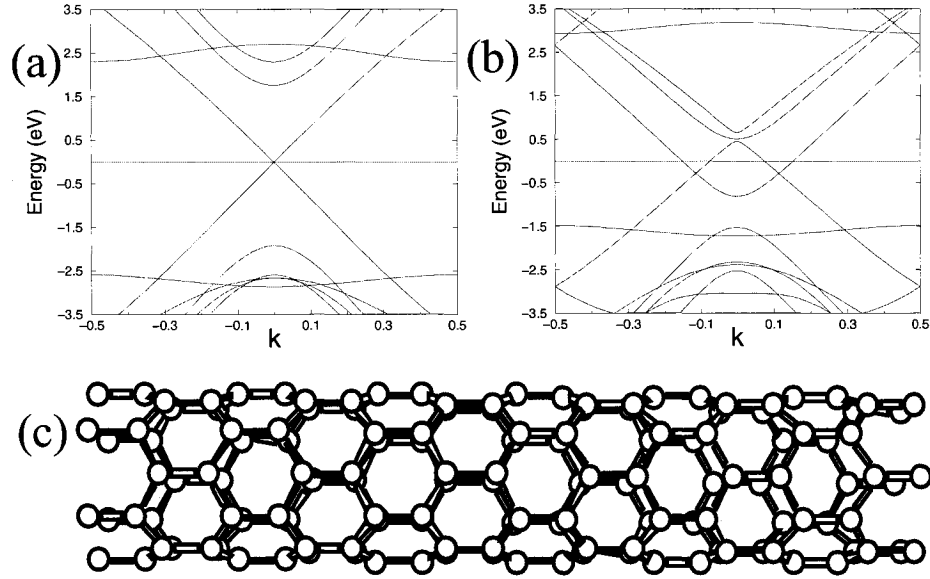


Figure 4.8: The band structure of the (6,0) CNT obtained through zone-folding (a) and calculated directly (b) along with the atomic structure (c).

(6,0)	mode	$\omega_q^{graph}$ (cm <sup>-1</sup> )	$M_{kk'}$ (eV/Å)
$2k_F^A$	4	857	7.27
	5	1585	6.80
$2k_F^B$	4	847	6.84
	6	1591	6.12
	3	68	3.73
	2	493	2.31

Table 4.2: Calculated values for the dominant coupling processes for the (6,0) CNT. The numbering scheme here corresponds to that given in Fig. 4.6.  $2k_F^A$  and  $2k_F^B$  correspond to inner and outer band processes respectively. Phonon frequencies are given for graphene.

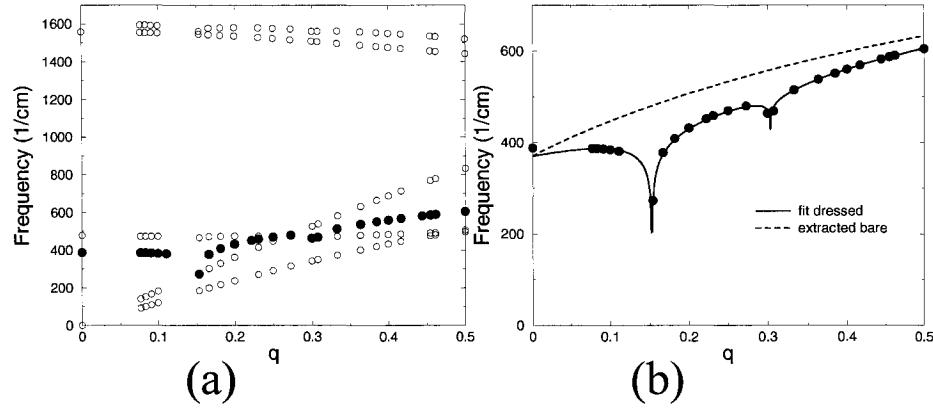


Figure 4.9: (a): Phonon dispersion for the (6,0) CNT along the  $\Gamma M$  line of graphene. (b): The mode showing the most softening fit to the RPA expression.

for extracting the bare phonon frequency at  $2k_F^A$ . From the previously computed values for the electron-phonon coupling matrix elements and the band structure, we find  $D_A = (166 \text{ cm}^{-1})^2$  and  $D_B = (107 \text{ cm}^{-1})^2$ . After fitting, we extract the value  $\Omega_{q=2k_F^A}^0 = 480 \text{ cm}^{-1}$ .

### 4.3.3 (5,5) nanotube

Finally, we study the more conventional armchair (5,5) CNT which has a diameter of around  $6.8 \text{ \AA}$ . As shown in Fig. 4.10, the zone-folding and directly computed band structure for this larger diameter tube agree quite well. Both of these band structures show two bands which originate from  $p_z$  orbitals which cross at the Fermi energy at around  $k = \frac{2}{3}\pi$ .

The largest couplings for the CNT were found to again be from the intraband processes and are shown in Fig. 4.6 and Table 4.3. The only significant intraband coupling is for an in-plane mode shown denoted by 7 in Fig. 4.6. The wave vector for this mode is at the  $K$  point in the first Brillouin zone of graphene. For the interband

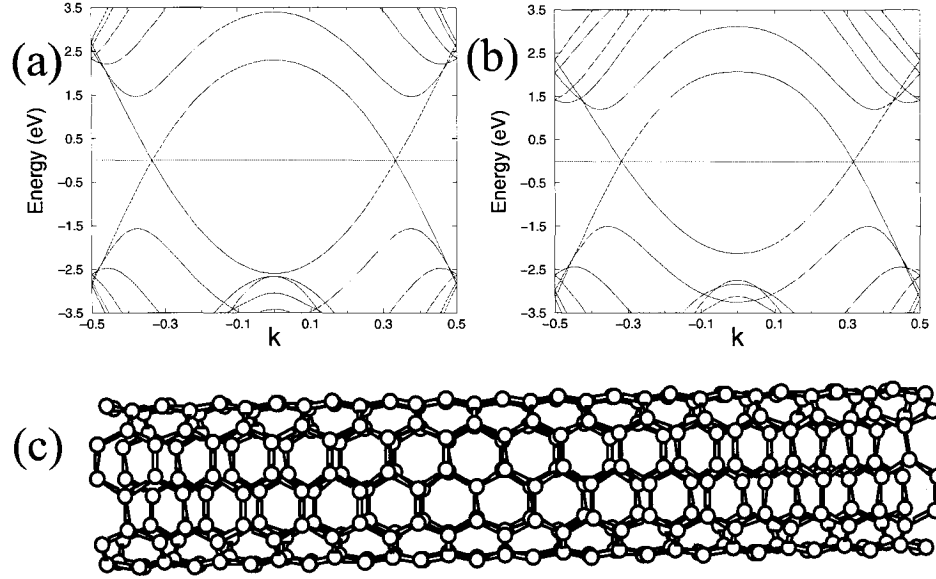


Figure 4.10: The band structure of the (5,5) CNT obtained through zone-folding and calculated directly are shown in the upper right and left. Bottom: the structure of the (5,5) CNT.

(5,5)	mode	$\omega_q^{graph}$ (cm <sup>-1</sup> )	$M_{kk'}$ (eV/Å)
	7	1479	11.60
	3	542	4.64

Table 4.3: Calculated values for the dominant coupling processes for the (5,5) CNT. The numbering scheme here corresponds to that given in Fig. 4.6. Phonon frequencies are given for graphene.

processes, there is coupling to the the radial breathing mode, but this is significantly smaller.

For the (5,5) CNT, applying our method of extracting the bare phonon frequencies, we obtain  $D_B = (228 \text{ cm}^{-1})^2$ . Note that for this system, only  $\pi$  bands are relevant at the Fermi surface. We extract  $\Omega_{q=2k_F}^0 = 1469 \text{ cm}^{-1}$ .

It is worth pointing out that there has been some controversy about the relevant phonon mode which couples the electrons at the Fermi surface for the (5,5) CNT.[70,

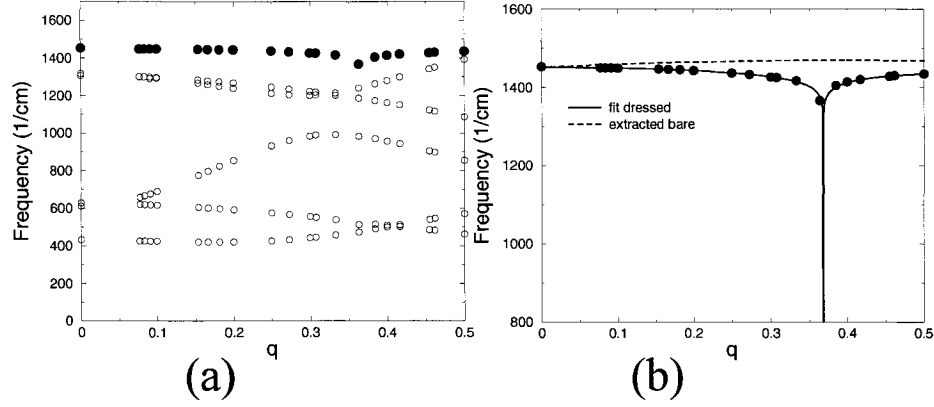


Figure 4.11: (a): Phonon dispersion for the (5,5) CNT along the  $MK$  line of graphene. (b): The mode showing the most softening fit to the RPA expression.

140] Our results confirm the study of Ref. [140]. The  $2k_F$  processes couple to the phonons at the K point of graphene and the relevant graphene mode has polarization vectors  $\hat{\epsilon}_q(1) = \frac{1}{\sqrt{2}}(i, 1, 0)$  and  $\hat{\epsilon}_q(2) = \frac{1}{\sqrt{2}}(1, i, 0)$ . This out-of-phase circular motion is qualitatively different from the linear oscillations thought to couple previously.

## 4.4 Instabilities of the electron-phonon system

### 4.4.1 Charge-density wave order

The RPA analysis presented in Sec. 4.2.4 can be used to investigate the CDW (Peierls) transition temperature. This instability corresponds to softening of the phonon frequency to zero, so we can obtain it from the condition  $\Omega_{Q_\tau} = 0$  in Eq. (4.14) where  $Q_\tau = 2k_{F\tau}$  is one of the nesting wave vectors of the Fermi surface. The electron polarization evaluated at temperature  $T$  is given by  $\chi_{0\tau}(2k_{F\tau}, \omega = 0, T) = \frac{1}{2}\nu_\tau(0) \log(T/4\varepsilon_{F\tau})$ , where  $\nu_\tau(0) = 2m_\tau^*/Lk_{F\tau}$  is the contribution to the total density

	(5,0)	(6,0)	(5,5)
mode	4	4	7
$\Omega_{2k_F}^0$ (cm <sup>-1</sup> )	433	480	1469
$\lambda_{\text{CDW}}$	0.26	0.12	0.024
$T_{\text{CDW}}$ (K)	160	5	$7 \times 10^{-14}$

Table 4.4: The dominant mode for the CDW instability, the extracted bare phonon frequency, the CDW coupling parameter, and the CDW transition temperature for the various CNTs studied.

of states from band  $\tau$ . We introduce the CDW coupling constant

$$\lambda_{\text{CDW},\tau\mu} = \frac{|g_{Q,\tau\mu}|^2 \nu_\tau(0)}{\Omega_{Q,\tau\mu}^0} \quad (4.20)$$

where  $\tau$  specifies which of the  $2k_F$  nesting wave vectors we are considering and  $\mu$  labels the phonon mode. Note, that distinguishing between various phonon modes is important, since it tells us about the nature of the distortion of atoms below the Peierls transition (i.e. the in the plane vs out of the plane). One finds for the CDW transition temperature

$$T_{\text{CDW},\tau\mu} = 4\varepsilon_{F\tau} e^{-1/\lambda_{\text{CDW},\tau\mu}}. \quad (4.21)$$

Corrections to this equation due to an additional band with different Fermi wave vector (e.g. the term with the logarithmic divergence at  $2k_F^B$  in Eq. 4.17) is small and will be neglected. Degenerate bands (e.g. the A band for the (5,0) CNT), are accounted for by an additional factor of 2 in the density of states in Eq. (4.20). In Table 4.4 we summarize our results for the CDW instability for the CNTs studied.

#### 4.4.2 Superconductivity

To analyze the superconducting instability of the CNTs we use the Migdal-Eliashberg theory. The isotropic Eliashberg equations for the one-dimensional case, neglecting



the Coulomb interaction, can be written as (see Appendix A.2 for details)

$$Z_n = 1 + f_n s_n \sum_{n'} \lambda(n - n') s_{n'} \quad (4.22)$$

$$Z_n \Delta_n = \sum_{n'} \lambda(n - n') f_{n'} \Delta_{n'} \quad (4.23)$$

where  $f_n = 1/|2n + 1|$ ,  $s_n = \text{sgn}(2n + 1)$ ,  $\Delta_n = \phi_n/Z_n$ , and the frequency dependent coupling constant  $\lambda(n)$  is given by

$$\begin{aligned} \lambda(n - n') = -\frac{1}{\nu_\sigma(0)} \sum_{k\tau k'\tau'\mu} \delta(\varepsilon_{k\tau}) \delta(\varepsilon_{k'\tau'}) |g_{kk'\mu}|^2 \\ \times D_\mu(k - k', n - n') \end{aligned} \quad (4.24)$$

where  $\nu_\sigma(0)$  is the density of states per spin at the Fermi energy. When analyzing superconductivity in two and three dimensional systems using the Eliashberg equations it is sufficient to take the bare phonon propagators  $D_0(k - k', n - n')$  in Eq. (4.24). This is justified since in the absence of Fermi surface nesting there is typically little difference between the bare and the dressed phonon frequencies and propagators. In one-dimensional systems, however, there is a strong temperature dependent renormalization of the phonon spectrum which needs to be taken into account. The simplest way to do so is to use the FPA form of the phonon propagator (see Eqns. (4.9) - (4.15))

$$D_\mu^{\text{FPA}}(q, i\nu_m) = \frac{2\Omega_{q\mu}^0}{(i\nu_m)^2 - (\Omega_{q\mu})^2}. \quad (4.25)$$

Here  $\Omega_{q\mu}$  is the dressed phonon frequency in the FPA given in Eq. (4.15). Taking a soft dressed phonon propagator immediately leads to the enhancement of the electron pairing via the increase of  $\lambda(n)$ . Enhancement of superconductivity by the giant Kohn anomaly in one-dimensional systems has been discussed previously by Heeger

in Ref. [63]. The main subtlety of the Eliashberg equations in this case is that the phonon frequency  $\Omega_{q\nu}$  now has temperature dependence which needs to be found using the finite temperature form of the polarization operator  $\Pi(q, 0)$  in Eq. (4.15).

When we analyze the (5,0) nanotube following this strategy, we find, however, that the CDW instability always appears before the superconducting one. This is in agreement with the general argument proposed in Ref. [53] that in strictly one-dimensional electron-phonon systems Peierls instability always dominates, since it involves all electrons in the band, compared to the superconducting instability, which involves only electrons in the vicinity of the Fermi surface.

To introduce a quantitative measure of the strength of superconducting pairing we use the *bare* phonon propagator in Eq. (4.24). This approximation will be more carefully considered in Sec. 4.5.4, along with inclusion of the Coulomb interaction. A useful approximate solution of the Eliashberg equations (4.22) - (4.24) is given by the McMillan formula (again in the absence of Coulomb interaction) [109, 3]

$$T_{\text{SC}} = \frac{\langle \Omega \rangle}{1.20} \exp \left[ -\frac{1.04(1 + \lambda_{\text{SC}})}{\lambda_{\text{SC}}} \right]. \quad (4.26)$$

Here  $\lambda_{\text{SC}}$  is the zero frequency component of Eq. (4.24) where, again, the bare phonon frequencies are used

$$\lambda_{\text{SC}} = -\frac{1}{\nu_{\sigma}(0)} \sum_{kk'} \delta(\varepsilon_k) \delta(\varepsilon_{k'}) |g_{kk'}|^2 D_0(k - k', 0). \quad (4.27)$$

In accordance with Ref. [12], we take  $\langle \Omega \rangle = 1400$  K. The superconducting coupling constants and transition temperatures calculated in this manner are summarized in Table 4.5. We emphasize, however, that these numbers should be taken with some skepticism, since within the same approximation the CDW instability is usually the dominant one and appears at much higher temperatures (compare to Table 4.4).

	(5,0)	(6,0)	(5,5)
$\lambda_{\text{SC}}$	0.57	0.12	0.031
$T_{\text{SC}}$ (K)	64	0.071	$1.11 \times 10^{-12}$

Table 4.5: The SC coupling parameter, and the SC transition temperature for the various CNTs studied. The CDW instability and the residual Coulomb interaction between electrons are neglected in the calculation of these quantities.

Finally, it is known that  $q \approx 0$  scattering processes due to acoustic phonons can be important in one-dimensional electron-phonon systems [164, 9, 49]. However, in the approximations leading to Eq. 4.27 these contributions were neglected. In Appendix A.3 we show that while these processes can be important for some systems, their inclusion leads to only a small correction to  $\lambda_{\text{SC}}$  for the CNTs we study. This is due to the fact that the dominant contributions to the superconducting coupling constant are from optical phonons.

## 4.5 Role of the Coulomb interaction

In the discussion above we concentrated on the electron-phonon interaction with electron-electron Coulomb interaction included only at the mean-field level via the band structure. It is useful to consider how the residual Coulomb interaction can modify the analysis of the Peierls and superconducting instabilities discussed above. We take

$$\mathcal{H} = \mathcal{H}_{\text{e-ph}} + \mathcal{H}_{\text{e-e}} \quad (4.28)$$

$$\mathcal{H}_{\text{e-e}} = \frac{1}{2} \sum_{kk'q\tau\tau'\sigma\sigma'} V_{q\tau\tau'} C_{k+q\tau\sigma}^\dagger C_{k'-q\tau'\sigma'}^\dagger C_{k'\tau'\sigma'} C_{k\tau\sigma}$$

where  $\mathcal{H}_{\text{e-ph}}$  is still given by Eq. (4.1) and we will always assume  $k$  and  $k'$  around the Fermi surface. Note that we have neglected interband scattering which is typically

small due to the orthogonality of the wave functions from different bands. In the following, we will consider how introducing this Coulomb interaction modifies the results.

### 4.5.1 Coulomb interaction potential

For the Coulomb interaction between conduction electrons, we take the form used by Egger *et al.* in Ref. [44]

$$V(\mathbf{r} - \mathbf{r}') = \frac{e^2/\kappa}{\sqrt{(x - x')^2 + \left(2R \sin\left(\frac{y - y'}{2R}\right)\right)^2 + a_z^2}}. \quad (4.29)$$

Here, the  $y$ -direction is chosen to be along the perimeter of the CNT and  $x$  measures the distance along the CNT axis. A measure of the spatial extent of the  $p_z$  electrons perpendicular to the CNT is given by  $a_z \approx 1.6 \text{ \AA}$  and  $R$  is the CNT radius. We note that the spatial extent of these electrons will differ inside and outside of the CNT, but the error from this approximation does not affect the magnitudes of the Coulomb matrix elements (which we evaluate below) significantly. Note that this interaction potential is periodic in the  $y$ -direction. For the dielectric constant due to the bound electrons, we will take the value  $\kappa \approx 2$  predicted by the model of Ref. [13].

We can now use Eq. (4.29) to obtain the Coulomb interaction entering Eq. (4.28)

$$V_{q\tau\tau'} = \int d^2r d^2r' V(\mathbf{r} - \mathbf{r}') \times \psi_{\mathbf{k}+q\tau}^*(\mathbf{r}) \psi_{\mathbf{k}\tau}(\mathbf{r}) \psi_{\mathbf{k}'-q\tau'}^*(\mathbf{r}') \psi_{\mathbf{k}'\tau'}(\mathbf{r}'). \quad (4.30)$$

The region of integration above is over areas of length  $L$  along the  $x$ -direction where  $L$  is the length of the system and of width  $2\pi R$  along the  $y$ -direction. For backward

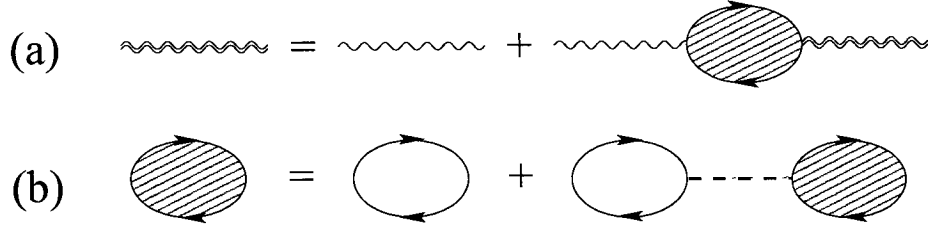


Figure 4.12: Dyson's equation for the phonon propagator (a) where the Coulomb interactions are taken into account within the RPA (b).

scattering processes ( $q \approx 2k_F$ ) between the inner bands of the (5,0) and (6,0) CNTs we find that  $V_{q\tau\tau'}$  is independent of  $\tau$  and  $\tau'$ , and (see Appendix A.5 for derivation)

$$\begin{aligned}
 V_q &\approx \gamma \frac{1}{L^2} \int dx dx' e^{-iq(x-x')} \\
 &\times \int_0^{2\pi R} \frac{dy}{2\pi R} \int_0^{2\pi R} \frac{dy'}{2\pi R} V(\mathbf{r} - \mathbf{r}')
 \end{aligned} \quad (4.31)$$

where  $\gamma = 0.59$  and  $0.0016$  for the (5,0) and (6,0) CNTs respectively. This is significantly reduced from the value of  $\gamma \approx 1$  that one obtains for larger radius CNTs [44] which is due to the fact that wave functions at the Fermi points have different symmetries for the (5,0) CNT and (6,0) CNTs. More specifically, it can be found that  $\mu_{\text{CDW}}$  is very small for the (6,0) CNT due to the fact that for metallic zig-zag nanotubes, the wave functions at  $-k$  and  $k$  close to the Fermi energy are nearly orthogonal within the unit cell of the CNT since they correspond to symmetric and antisymmetric combinations of atomic orbitals in the graphene sheet.

#### 4.5.2 Modification of CDW instability due to Coulomb interaction

The simplest approximation (beyond mean-field) which includes the Coulomb repulsion is the RPA shown in Fig. 4.12 (see e.g. Refs. [139, 97]), Eq. (4.14) now

becomes for a one-band system

$$(\Omega_{q\mu})^2 = (\Omega_{q\mu}^0)^2 + 2\Omega_{q\mu}^0 \frac{\Pi_\mu(q, \Omega_{q\mu})}{1 - V(q)\chi_0(q, \Omega_{q\mu})} \quad (4.32)$$

where  $\Pi_\mu(q, \Omega_{q\mu}) = |g_{q\mu}|^2 \chi_0(q, \Omega_{q\mu})$ . We immediately see that including the Coulomb interaction can suppress the CDW instability. The second term in Eq. (4.32) no longer diverges when  $q = 2k_F$  and the softening of the  $2k_F$  phonons occurs only for  $\mu_{\text{CDW}} < \lambda_{\text{CDW},\mu}$ , where

$$\mu_{\text{CDW}} \equiv \frac{1}{2} \nu(0) V_{q=2k_F}. \quad (4.33)$$

From equation (4.32) we also find how the Coulomb interaction modifies the Peierls transition temperature

$$T_{\text{CDW},\mu} = 4\varepsilon_F \exp\left(-\frac{1}{[\lambda_{\text{CDW},\mu} - \mu_{\text{CDW}}]}\right). \quad (4.34)$$

We will now estimate the magnitude of  $\mu_{\text{CDW}}$  from this residual Coulomb interaction for the (5,0) which was seen above to be the most unstable toward the formation of a CDW from distortion of the out-of-plane optical mode shown in Fig. 4.6. Carrying through the straightforward generalization of the RPA analysis for the multiple-band system, and carrying out the integrals in Eq. (4.31) for the Coulomb backward scattering interaction, we obtain  $\mu_{\text{CDW}} = 0.24$ . Note that this is quite close to  $\lambda_{\text{CDW}} = 0.26$  for this particular instability. This indicates that it is possible that the Coulomb interaction can significantly suppress the CDW transition temperature or even remove the CDW instability altogether. Indeed, taking these values we find that  $T_{\text{CDW}}$  is suppressed to less than  $10^{-18}$  K.

For the (6,0) CNT, we calculate the smaller value  $\mu_{\text{CDW}} = 0.0019$ . This will not change the value of  $T_{\text{CDW}} = 5.0$  K that we calculated previously for the (6,0) CNT.

### 4.5.3 Phonon vertex renormalization through screening

It can be seen that the Coulomb interaction further can screen the electron-phonon vertex. By including screening through the RPA, we find that the screened vertex is given by [139]

$$\bar{g}_{q\mu} = \frac{g_{q\mu}}{1 - V_q \chi_0(q)} \quad (4.35)$$

for a one-band system where  $\chi_0(q) \equiv \chi_0(q, \Omega_{q\mu} = 0)$ . Thus we see that the inclusion of screening reduces the electron-phonon vertex. We note that in the treatment in Sec. 4.5.2 of the CDW instability it would be inappropriate to use the screened vertices since this would lead to double-counting.

Full charge self-consistent calculations will determine the dressed electron-phonon vertex (see Appendices A.1 and A.4). This is desirable in 3d, where the renormalization is presumably small. However in 1d, one would calculate greatly suppressed values for the couplings, dominated by the screening due to the logarithmic divergence of the susceptibility at  $2k_F$ . Because of the subtle interplay between these divergences, it is desirable to calculate the bare vertex and then manually put in the Coulomb interaction as we do.

Since with the method we use, the charge distribution is not calculated self-consistently, we calculate the bare electron-phonon vertex  $g_{q\mu}$ . We point out, however, that there is an approximation here. The true bare electron-phonon vertex should be calculated in the absence of the conduction electron entirely which is separately accounted for in the residual Coulomb term. In our method, however, the conduction electron is taken to adiabatically follow the ion through the distortion. Because of this, we expect our results to slightly underestimate the bare electron-phonon coupling

vertices.

#### 4.5.4 Modification of superconducting instability due to Coulomb interactions

To include the Coulomb interaction in the Eliashberg equations, it is necessary to dress both electron-phonon vertices shown in Fig. A.1 according to Sec. 4.5.3 as well as the phonon propagator according to Sec. 4.5.2. This leads to the modified phonon-mediated interaction between electrons of

$$|\bar{g}_{q\mu}|^2 D_\mu(q, \Omega) = \frac{|g_{q\mu}|^2}{(1 - V_q \chi_0(q))^2} \times \frac{2\Omega_{q\mu}^0}{\Omega^2 - (\Omega_{q\mu}^0)^2 - 2\Omega_{q\mu}^0 |g_{q\mu}|^2 \frac{\chi_0(q)}{1 - V_q \chi_0(q)}}. \quad (4.36)$$

Using this leads to a modified result for the superconducting coupling constant  $\lambda_{\text{SC}}$ . For a specific process of wave vector  $q$ , coupling points on the Fermi surface, we find that the renormalized contribution to the superconducting coupling constant is given by

$$\lambda_{q\mu} = \left( \frac{1}{(1 - V_q \chi_0(q))^2} \right) \left( \frac{1}{1 + \frac{2|g_{q\mu}|^2}{\Omega_{q\mu}^0} \frac{\chi_0(q)}{1 - V_q \chi_0(q)}} \right) \lambda_{q\mu}^0 \quad (4.37)$$

where  $\lambda_{q\mu}^0$  is the unrenormalized contribution. All such contributions must be summed over to determine the total  $\lambda_{\text{SC}}$ . The first and second factors tend to decrease and increase the electron-phonon coupling, respectively. Physically, the first factor is due to the screening of the electron-ion interaction due to conduction electrons. The second factor is due to the softening of particular modes due to the Kohn Anomaly which will in turn enhance the overall electron-phonon coupling. Since these renormalization



factors depend on temperature through the susceptibility  $\chi_0$ ,  $T_{\text{SC}}$  must be determined self-consistently.

In addition to the renormalization of the Coulomb vertex, there is also the direct Coulomb repulsion between electrons that is taken into account through the Coulomb pseudopotential  $\mu_{\text{SC}}^*$  which is included in McMillan's expression [109, 3]

$$T_{\text{SC}} = \frac{\langle \Omega \rangle}{1.2} \exp \left( - \frac{1.04(1 + \lambda_{\text{SC}})}{[\lambda_{\text{SC}} - \mu_{\text{SC}}^*(1 + 0.62\lambda_{\text{SC}})]} \right) \quad (4.38)$$

where

$$\mu_{\text{SC}}^* = \frac{\mu_{\text{SC}}}{1 + \mu_{\text{SC}} \ln \left( \frac{E_F}{\omega_D} \right)} \quad (4.39)$$

and  $\mu_{\text{SC}}$  is the screened Coulomb interaction averaged over the Fermi surface.

We will now estimate  $\mu_{\text{SC}}^*$ . Taking into account screening within the RPA one finds

$$V_q^s = \frac{V_q}{1 - V_q \chi_0(q)} \quad (4.40)$$

for the screened Coulomb interaction. In 1d for  $q \approx 2k_F$ ,  $V_q^s \approx 0$ . This is due to the divergence of  $\chi_0(q)$  at  $q = 2k_F$ . Also, one finds that for  $q \approx 0$ ,  $V^s(q) \approx 1/\nu(0)$ . Using this RPA screened Coulomb interaction we find for our three band system of the (5,0) CNT

$$\mu_{\text{SC}} \equiv \frac{1}{\nu_\sigma(0)} \sum_{k\tau k'\tau'} \delta(\varepsilon_{k\tau}) \delta(\varepsilon_{k'\tau'}) V_{\tau\tau'}^s(k - k') = 0.25. \quad (4.41)$$

Then, using Eq. (4.39), we obtain  $\mu_{\text{SC}}^* = 0.19$  for the Coulomb pseudopotential with the calculated values of the Fermi energy and Debye frequency.

We now see how taking into account the Coulomb interaction in this manner modifies the superconducting transition temperature for the (5,0) CNT. The most

significant renormalization of the total superconducting  $\lambda_{\text{SC}}$  given by Eq. (4.37) will be for the  $2k_F$  process that couples to the out-of-plane optical mode which was previously seen to have the overall strongest coupling. That is, at temperatures where the renormalized  $\lambda_{\text{SC}}$  will start to differ from the bare  $\lambda_{\text{SC}}^0$ , all of the renormalization will come from this mode. Using Eqns. (4.37) and 4.38, we find that a self-consistent solution for the superconducting transition temperature occurs at  $T_{\text{SC}} \approx 1.1$  K which is larger than the previously calculated CDW transition temperature. This therefore shows that the Coulomb interactions can favor superconductivity over the CDW instability.

For the (6,0) CNT, we see that the value of  $T_{\text{SC}}$  without the inclusion of Coulomb interaction is smaller than  $T_{\text{CDW}} = 5\text{K}$  that we computed in the previous section with the inclusion of the Coulomb interaction. We therefore conclude that the CDW will be dominant for the (6,0) CNT.

#### 4.5.5 Summary of Coulomb effects

In the above, we have shown that the introduction of the residual Coulomb interaction will lower both the SC and CDW transition temperatures. We also illustrated the possibility that the CDW instability can be suppressed so much by Coulomb interactions that SC will be dominant at low temperatures. However, we stress the difficulty of obtaining such quantitative results. In principle, to obtain an accurate Coulomb interaction in our basis of Bloch states, one needs to use the interaction

$$V_{kk'k''k'''} = \frac{1}{\kappa} \int d^3r d^3r' \psi_k^*(\mathbf{r}) \psi_{k'}^*(\mathbf{r}') \frac{e^2}{|\mathbf{r} - \mathbf{r}'|} \psi_{k''}(\mathbf{r}') \psi_{k'''}(\mathbf{r}) \quad (4.42)$$

where the  $\psi_k$ 's are Bloch state wave functions of the CNT which is difficult to obtain. The Coulomb interaction  $V_q$  we used is only a rough approximation to this more realistic interaction. On the other hand, the SC and CDW transition temperatures have exponential dependence on the Coulomb interaction parameters. One also has to be very careful not to double-count the electron-electron interaction terms taken into account in the single-particle energies  $\varepsilon_k$  through the Hartree term. As shown in Appendix A.4, using a method in which the charge density is calculated self-consistently will give more accurate values for the phonon frequencies calculated through the FPA. However, there are serious difficulties with calculating the bare electron-phonon vertex with such a method as discussed in Sec. 4.5.3.

## 4.6 Discussion

### 4.6.1 Comparison to other carbon based materials

As a consistency check, we now compare our results for the attractive potential due to electron-phonon coupling to established results for other carbon based solids, namely the intercalated graphene  $\text{KC}_8$  and the carbon fullerene  $\text{K}_3\text{C}_{60}$ . Calculations of the density of states at the Fermi energy yield  $\nu(0) = 0.24$  (Ref. [74]) and 0.29 (Ref. [8]) states/ eV / C atom for  $\text{KC}_8$  and  $\text{K}_3\text{C}_{60}$  respectively. Estimates of  $\lambda_{\text{SC}}$  for these are 0.21 (Ref. [74]) and 0.7 (Ref. [12]). In the BCS theory,  $\lambda_{\text{SC}}$  is expressed in terms of the product of the electronic density of states at the Fermi level and the attractive pairing potential strength  $\lambda_{\text{SC}} = \nu(0)V$ . [139] Now that we have the magnitude  $\lambda_{\text{SC}}$  and  $\nu(0)$ , we can extract the magnitude of the pairing potential for

	KC <sub>8</sub>	K <sub>3</sub> C <sub>60</sub>	(5,0) CNT	(6,0) CNT	(5,5) CNT
$\nu(0)$ (eV <sup>-1</sup> )	0.24 <sup>a</sup>	0.29 <sup>b</sup>	0.16	0.068	0.034
$\lambda_{\text{SC}}$	0.21 <sup>a</sup>	0.7 <sup>c</sup>	0.57	0.12	0.031
$V$ (eV)	0.875	2.4	3.6	1.8	0.92

Table 4.6: Density of states at the Fermi energy, the superconducting coupling strength, and the attractive potential strength for various carbon materials. Superscripts  $a$ ,  $b$ , and  $c$  denote Refs. [74], [[8]], and [12] respectively.

the intercalated graphene, the fullerene, and the CNTs we study. The results are summarized in Table 4.6.

The following analysis will be very similar to that of Benedict *et al.* in Ref. [12]. The central idea in their analysis is as follows. Since curvature increases the amount of hybridization between  $\sigma$  and  $\pi$  states at the Fermi energy, the strict selection rules for phonon scattering between pure  $\pi$  states in graphene will be lifted. The amount of  $\sigma - \pi$  hybridization has roughly a  $1/R$  dependence on the radius of curvature, so the matrix elements and therefore the attractive potential due to curvature will go as  $1/R^2$  [12].

Neglecting presence of pentagons in fullerenes, we write the attractive potential for the fullerene  $V_{\text{ball}}$  as the sum of contributions from that of the graphene sheet  $V_{\text{flat}}$  and that from curvature effects  $V_{\text{curve}}$

$$V_{\text{ball}} = V_{\text{flat}} + V_{\text{curve}}. \quad (4.43)$$

This relation enables us to obtain the value for  $V_{\text{curve}} = 1.5$  eV. Now we can write the expected attractive interaction for the CNT

$$V_{\text{tube}}(R) = V_{\text{flat}} + V_{\text{curve}} \left( \frac{R_0/2}{R} \right)^2 \quad (4.44)$$

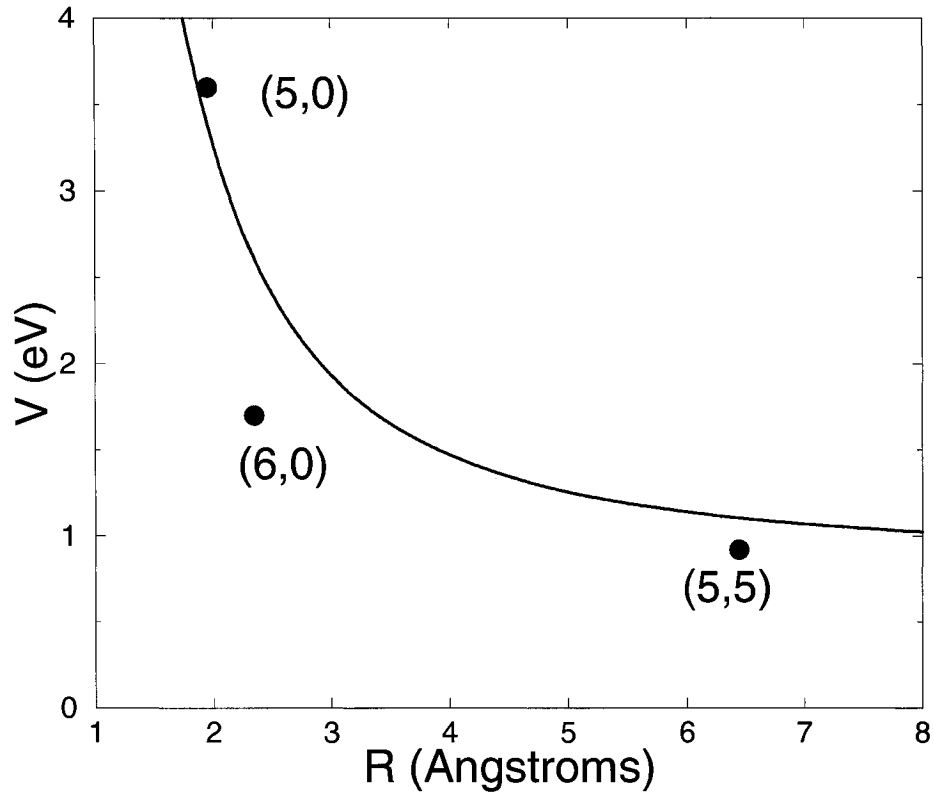


Figure 4.13:  $V_{\text{tube}}(R)$  from Eq. (4.44) calibrated with parameters from intercalated graphene and fullerenes (solid line) compared to the attractive potentials calculated for the representative CNTs (filled circles).

where  $R_0 \approx 5 \text{ \AA}$  is the radius of a fullerene and the factor of two comes in because there is twice as much  $\sigma - \pi$  hybridization in a fullerene as there is in a CNT of radius  $R_0$ . [12] In Fig. 4.13, we show that Eq. (4.44), which was calibrated by using only quantities from intercalated graphene and fullerenes, is consistent with the attractive potentials we obtain for the (5,0), (6,0), and (5,5) CNTs.

### 4.6.2 Beyond mean field theory

One-dimensional electron-phonon systems have several competing instabilities and the true ground state may be found only by analyzing their interplay. [160, 161] Hence, one may be concerned that we use a mean-field approach to analyze a 1d CNT. We point out that when we calculate the superconducting  $T_{\text{SC}}$  we include the interplay of the CDW and SC orders. That is, the effective superconducting coupling  $\lambda_{\text{SC}}$  that we obtain in Eq. 4.37 includes softening of the  $2k_F$  phonon mode. Such an approach is equivalent to the two parameter RG analysis used in Ref. [59]. The mean-field transition temperature obtained by our method is equivalent to the coupling constants becoming of the order of unity in the RG analysis. At  $T_{\text{SC}}$  electrons start to pair, but the system has strong fluctuations in the phase of the SC order parameter. The most important kind of fluctuations are thermally activated phase slips, discussed originally for superconducting wires in Refs. [94, 107]. Phase slips lead to only a gradual decrease of resistivity with temperatures below  $T_{\text{SC}}$ .

For an incommensurate CDW, long range order may not appear at finite temperature either. To understand the physical meaning of the mean-field transition, we can introduce a Landau-Ginzburg formalism. [24] Here we concentrate on the (5,0) and (6,0) CNTs which have three partially filled bands with Fermi points  $k_F^A$  and  $k_F^B$  where the exact relation  $2k_F^A = k_F^B$  is satisfied. We introduce a complex order parameter  $\Psi_1(x)$  related to the amplitude of the lattice distortion as  $q(x) = e^{2ik_F^A x} \Psi_1(x) + e^{-2ik_F^A x} \Psi_1^*(x)$ . At low temperature the free energy is given by  $F_\sigma[\Psi_1] = \int dx (a|\Psi_1|^2 + b|\Psi_1|^4 + c|\frac{d\Psi_1}{dx}|^2)$ . Below the mean-field transition temperature  $T_{\text{CDW}}$  we have  $a < 0$  and the system develops an amplitude for the order

parameter  $\Psi_1$ . The phase of  $\Psi_1$ , however, is still fluctuating, leading to short range correlations for the CDW order  $\langle \Psi_1(x)\Psi_1^*(0) \rangle \propto e^{-x/\xi(T)}$ . Even at  $T = 0$  we can have at best a quasi long-range order for  $\Psi_1$  due to the incommensurate value of  $2k_F^A$ . Lattice distortions at  $2k_F^B$  can be included by introducing another complex field  $\Psi_2(x)$  that contributes  $e^{2ik_F^B x} \Psi_2(x) + e^{-2ik_F^B x} \Psi_2^*(x)$  to the distortion amplitude. The relation  $2k_F^A = k_F^B$  implies that the free energy allows coupling between  $\Psi_1$  and  $\Psi_2$  of the form  $F_{\pi\sigma}[\Psi_1, \Psi_2] = \gamma \int dx (\Psi_1^2 \Psi_2^* + \Psi_1^{*2} \Psi_2)$ , so when the amplitude of  $\Psi_1$  is established, it will immediately induce the amplitude for  $\Psi_2$  (although none of the fields have a long-range order). Appearance of such amplitudes should lead to a pseudogap state of the system below  $T_{\text{CDW}}$ . [24] The dominant contribution to electrical conductivity in a clean system would then come from the Goldstone mode of the phase of the  $\Psi$ 's, i.e. sliding of CDWs (Fröhlich mode). Any kind of disorder (e.g. impurities or crystal defects), however, gives strong pinning of the CDW phase and suppresses collective mode contributions to transport. Therefore, we expect insulating behavior of the low temperature resistivity in most experimentally relevant circumstances if CDW is the dominant low temperature phase.

### 4.6.3 Experimental Implications

Proximity induced [82, 118] as well as intrinsic [86, 152] superconductivity has been experimentally observed in carbon nanotubes. On the other hand, the CDW state, despite being endemic to quasi 1d systems has never been reported for carbon nanotubes. As we discuss above, one needs to have very small carbon nanotubes to have electron-phonon interaction strong enough to make either the CDW or the SC

instabilities appear at experimentally relevant temperatures. In this work we address quantitatively both of these instabilities. Our main conclusion is that when we include Coulomb interaction between electrons, the CDW instability does not appear even for the ultrasmall nanotubes, whereas the superconducting  $T_{SC}$  may be in the few Kelvin range.

In the work by Kociak *et al.* in Ref. [86], electronic transport through ropes of single-walled CNTs suspended between normal metal contacts was measured. The ropes are composed of several hundred CNTs in parallel with diameters of the order 1.4 nm. It was found that below 0.5 K, the resistance abruptly drops, an effect which is destroyed by the application of an external magnetic field of order 1 T. The largest radius CNT we study is the (5,5) CNT, which was seen to be in the regime where zone-folding is applicable. For this CNT, we calculated  $\lambda_{SC} = 0.031$ , a value far too small to support superconductivity at this temperature even without the inclusion of the Coulomb interaction. This small value of  $\lambda_{SC}$  is consistent with the experimental measurements of the electron-phonon coupling in CNTs of similar diameter by Hertel *et al.* in Ref. [65]. It is possible that the interactions between CNTs in the rope play a tantamount role for superconductivity in the experiment of Ref. [86] as suggested by Gonzalez in Ref. [54]. Another possibility is that a small number of nanotubes in the rope have a small diameter. For nanotubes with a diameter of 4 Å we find superconducting  $T_{SC}$  in the 1 K range which would be consistent with these experiments. A small number of superconducting nanotubes could provide a short-circuiting in transport measurements or even induce superconductivity in other CNTs via the proximity effect.



In the experimental work of Tang *et al.* in Ref. [152], electrical transport was measured through a zeolite matrix containing single-walled CNTs. In the zeolite matrix, the CNTs are well-separated from each other creating an idealized one-dimensional system. The diameters of the CNTs were determined to be approximately 4 Å by measuring the radial breathing phonon mode frequency by Raman spectroscopy. The superconducting transition temperature for this system was found to be 15 K from transport measurements. In addition, the Meissner effect was observed through the temperature dependence of the magnetic susceptibility suggesting that the large currents observed in transport measurements are not from the sliding charge-density wave collective mode, but are indeed from superconducting correlations.

The ultrasmall (5,0) CNT we study is the likely candidate structure for the CNTs confined in the zeolite matrix in these experiments. We find for this system that the electron-phonon coupling is very strong. We find in the mean-field theory, neglecting Coulomb interactions, that  $T_{\text{CDW}} = 160$  K and  $T_{\text{SC}} = 64$  K, indicating that the charge-density wave instability is stronger in this approximation. However, putting in the Coulomb interaction as in Eq. (4.28), the charge-density wave transition was suppressed to very low temperatures, making superconductivity dominant with  $T_{\text{SC}} = 1$  K. Discrepancy between our calculated  $T_{\text{SC}}$  and the experimentally observed 15 K should not be a reason for concern. The superconducting transition temperature in Eq. 4.38 is exponentially sensitive to the strength of the Coulomb interaction, and our estimates of the latter are not very accurate.

## 4.7 Summary and Conclusions

In this work, we have used the Fröhlich Hamiltonian written in Eq. (4.1) to study three types of small-radius CNTs. For this Hamiltonian, the band structure energies were computed by using an empirical tight-binding method [110] to first relax the structure, and then to compute the eigenvalues of the secular tight-binding equation. The electron-phonon interaction  $g_{k\tau k'\tau'\mu}$  is evaluated for scattering between all Fermi points. The dressed phonon frequencies  $\Omega_{q\mu}$  are computed by using the frozen-phonon approximation given in Eq. (4.8) by the displacement vectors from the dynamical matrix of graphene given in Ref. [78]. The undressed frequencies  $\Omega_{q\mu}^0$ , which enter the Fröhlich Hamiltonian in Eq. (4.1), are then extracted by using the previously computed quantities of the band structure and the electron-phonon coupling, and the RPA analysis of the Peierls instability. This method is elaborated in Sec. 4.2.4. After the calculation of these quantities, the effective Fröhlich Hamiltonian has been fully constructed. The remarkable agreement of the coefficients of the logarithmic divergences computed by using quantities from the band structure and the electron-phonon coupling with the frozen-phonon frequencies is a consistency check for this method.

With the Fröhlich Hamiltonian, we then used the RPA analysis of the Peierls instability (in Sec. 4.4.1 ) and the McMillan equation (in Sec. 4.4.2 and Appendix A.2) to obtain the charge-density wave and superconducting transition temperatures, the result with the higher transition temperature being the dominant phase at low temperatures. For instance, when the CDW is dominant, the Fermi surface will be destroyed around  $T_{\text{CDW}}$  eliminating superconductivity altogether. By this method, we

provided an exhaustive analysis of three types of CNTs: (5,0), (6,0), and (5,5). The more conventional larger-radius (5,5) CNT was seen to be stable against the CDW and SC transitions down to very low temperatures ( $\ll 1\text{K}$ ) if we only include electron-phonon interactions. For the ultrasmall radius (5,0) and (6,0) CNTs, however, the CDW was found to be the dominant phase, with transition temperatures of 160 and 6 K respectively. For both of these CNTs,  $2k_F$  is incommensurate with the underlying lattice. Furthermore, in contrast to larger radius CNTs which have dominant electron-phonon coupling to the in-plane phonon modes, the ultrasmall (5,0) and (6,0) CNTs were found to have dominant coupling to the out-of-plane phonon modes (see Fig. 4.6), as seen from the direct computation of the electron-phonon matrix elements  $M_{k\tau k'\tau'\mu}$ . This is further supported by the frozen-phonon computation of frequencies which show the most robust Kohn anomalies for these modes (see Fig. 4.6).

When we include the Coulomb interaction, for the (5,0) CNT we find that the CDW order is suppressed much more strongly than superconductivity. More specifically, our analysis presented in Sec. 4.5 shows that the CDW transition is pushed down to unobservably low temperatures, whereas the superconducting  $T_{\text{SC}}$  is reduced to 1 K. Hence our calculation supports the possibility of observing superconductivity in ultrasmall CNTs. It is quite foreseeable that a more detailed model for the Coulomb interaction could raise  $T_{\text{SC}}$  to the value seen experimentally, especially considering the exponential dependence of the superconducting transition temperature on the Coulomb interaction strength. For the (6,0) CNT, we found that the CDW remains dominant when the Coulomb interactions are included due to the weak Coulomb interaction between electrons at the Fermi points, and occurs at around  $T_{\text{CDW}} = 5\text{K}$ .

## **4.8 Acknowledgements**

We thank B. Halperin, S. Kivelson, I. Mazin, M. Mehl, and M. Tinkham for useful discussions. This work was supported by the Harvard NSEC and by the Sloan foundation. RB was supported by an NSF graduate research fellowship.

# Chapter 5

## Quantum magnetism with dipolar molecules and spin two bosons in an optical lattice

### 5.1 Spin two bosons in an optical lattice

#### 5.1.1 Hyperfine interaction

In this section, we consider alkali atoms in an optical lattice. These atoms have a nuclear spin of  $I = 3/2$  and electronic spin of  $J = S = 1/2$  ( $L = 0$ ). The hyperfine interaction enters the hamiltonian as

$$\mathcal{H}_{\text{hf}} = A \mathbf{I} \cdot \mathbf{J} = \frac{A}{2}(F^2 - I^2 - J^2) \quad (5.1)$$

where  $\mathbf{F} = \mathbf{I} + \mathbf{J}$ . This will split the degeneracy of the spin states into states with  $F = 1$  and  $F = 2$ . This splitting for  $^{87}\text{Rb}$  is around 7 GHz. The case of  $F = 1$  was

worked out in Imambekov *et al.* [73], so here we consider  $F = 2$  bosons.

### 5.1.2 From the two-body scattering interaction to the onsite interaction

First we start with the two-body scattering problem of spin two bosons. Since the overall wave function must be symmetric, the interaction potential between two such bosons is

$$V(\mathbf{x}_1 - \mathbf{x}_2) = \delta(\mathbf{x}_1 - \mathbf{x}_2)(g_0\mathcal{P}_0 + g_2\mathcal{P}_2 + g_4\mathcal{P}_4). \quad (5.2)$$

We can use the identities

$$\begin{aligned} \mathcal{P}_0 &= \mathcal{P}_0 \\ \mathcal{P}_2 &= \frac{4}{7} - \frac{10}{7}\mathcal{P}_0 - \frac{1}{7}\mathbf{F}_1 \cdot \mathbf{F}_2 \\ \mathcal{P}_4 &= \frac{3}{7} + \frac{3}{7}\mathcal{P}_0 + \frac{1}{7}\mathbf{F}_1 \cdot \mathbf{F}_2 \end{aligned} \quad (5.3)$$

where we note that  $\mathbf{F}_1 \cdot \mathbf{F}_2 = -6, -3, 4$  for combined spin  $S = 0, 2, 4$  to rewrite the interaction as

$$V(\mathbf{x}_1 - \mathbf{x}_2) = \delta(\mathbf{x}_1 - \mathbf{x}_2) \left( \frac{1}{7}(4g_2 + 3g_4) + \frac{1}{7}(7g_0 - 10g_2 + 3g_4)\mathcal{P}_0 + \frac{1}{7}(g_4 - g_2)\mathbf{F}_1 \cdot \mathbf{F}_2 \right). \quad (5.4)$$

This then leads to the onsite interaction

$$\mathcal{H}_U = \frac{1}{2}U_0n(n-1) + \frac{1}{2}U_1\mathcal{P}_0 + \frac{1}{2}U_2(F^2 - 6n) \quad (5.5)$$

where  $n = a_\alpha^\dagger a_\alpha$  and  $\mathbf{F} = a_\alpha^\dagger \mathbf{T}_{\alpha\beta} a_\beta$ .  $\mathbf{T}_{\alpha\beta}$  are the spin-2 matrices given by

$$T^x = \frac{1}{2} \begin{pmatrix} 0 & 2 & 0 & 0 & 0 \\ 2 & 0 & \sqrt{6} & 0 & 0 \\ 0 & \sqrt{6} & 0 & \sqrt{6} & 0 \\ 0 & 0 & \sqrt{6} & 0 & 2 \\ 0 & 0 & 0 & 2 & 0 \end{pmatrix} \quad (5.6)$$

$$T^y = \frac{i}{2} \begin{pmatrix} 0 & -2 & 0 & 0 & 0 \\ 2 & 0 & -\sqrt{6} & 0 & 0 \\ 0 & \sqrt{6} & 0 & -\sqrt{6} & 0 \\ 0 & 0 & \sqrt{6} & 0 & -2 \\ 0 & 0 & 0 & 2 & 0 \end{pmatrix} \quad (5.7)$$

$$T^z = \begin{pmatrix} 2 & 0 & 0 & 0 & 0 \\ 0 & 1 & 0 & 0 & 0 \\ 0 & 0 & 0 & 0 & 0 \\ 0 & 0 & 0 & -1 & 0 \\ 0 & 0 & 0 & 0 & -2 \end{pmatrix} \quad (5.8)$$

The onsite interaction parameters are given by  $U_0 = \frac{\alpha}{7}(4g_2 + 3g_4)$ ,  $U_1 = \frac{\alpha}{7}(7g_0 - 10g_2 + 3g_4)$ , and  $U_2 = \frac{\alpha}{7}(g_4 - g_2)$  where  $\alpha$  is a constant depending on the shape of the onsite Wannier functions.

### 5.1.3 Effective spin interaction for one boson per site

For one boson per site there will be a macroscopic degeneracy if there is no tunneling between sites. The tunneling hamiltonian

$$\mathcal{H}_J = -J \sum_{\langle ij \rangle} (a_{i\alpha}^\dagger a_{j\alpha} + \text{h.c.}) \quad (5.9)$$

will break this degeneracy which will be described by the effective hamiltonian

$$\mathcal{H}_{\text{eff}} = \mathcal{P} \sum_{m \neq 0} \frac{\mathcal{H}_J |m\rangle \langle m| \mathcal{H}_J}{E_0 - E_m} \mathcal{P} \quad (5.10)$$

where  $\mathcal{P}$  projects onto states with single occupancy. This effective hamiltonian can be written as

$$\mathcal{H}_{\text{eff}} = \mathcal{P} \sum_{s=0}^4 \epsilon_s \sum_{\langle ij \rangle} \mathcal{P}_{ij}(S) \mathcal{P} \quad (5.11)$$

where  $\mathcal{P}_{ij}(S)$  projects for neighboring sites into a state with total spin  $S$ . We find that

$$\epsilon_0 = \frac{-4J^2}{U_0 + \frac{1}{2}U_1 - 6U_2}; \quad \epsilon_2 = \frac{-4J^2}{U_0 - 3U_2}; \quad \epsilon_4 = \frac{-4J^2}{U_0 + 4U_2} \quad (5.12)$$

and  $\epsilon_1 = \epsilon_3 = 0$ .

### 5.1.4 Phase diagram

We now consider the phase diagram for one boson per site obtained from the effective spin hamiltonian. To do so, we use the translationally invariant wave function of the form

$$|\psi\rangle = \prod_i A_\alpha |\alpha\rangle_i \quad (5.13)$$

where  $A_\alpha$  are variational parameters satisfying  $A_\alpha^* A_\alpha = 1$  and  $|\alpha\rangle_i$  is the eigenstate of  $F_{iz}$  with eigenvalue  $\alpha$  (the sum over  $\alpha = -2, -1, 0, 1, 2$  is implicit). Since this wave



function is translationally invariant,  $\langle \mathcal{P}_{ij}(S) \rangle$  will not depend on site indices so we will suppress them. Then we have for the energy,

$$E/N = \epsilon_0 \langle \mathcal{P}(0) \rangle + \epsilon_2 \langle \mathcal{P}(2) \rangle + \epsilon_4 \langle \mathcal{P}(4) \rangle = (\epsilon_0 - \epsilon_4) \langle \mathcal{P}(0) \rangle + (\epsilon_2 - \epsilon_4) \langle \mathcal{P}(2) \rangle + \epsilon_4 \quad (5.14)$$

where we note that  $\langle \mathcal{P}(1) \rangle = \langle \mathcal{P}(3) \rangle = 0$ . Evaluating the expectation values of the projection operators leads to the somewhat cumbersome expressions

$$\langle \mathcal{P}(0) \rangle = \frac{1}{5} |A_0 A_0 - 2A_1 A_{-1} + 2A_2 A_{-2}|^2 \quad (5.15)$$

and

$$\langle \mathcal{P}(2) \rangle = \langle \mathcal{P}(2, 2) \rangle + \langle \mathcal{P}(2, 1) \rangle + \langle \mathcal{P}(2, 0) \rangle + \langle \mathcal{P}(2, -1) \rangle + \langle \mathcal{P}(2, -2) \rangle \quad (5.16)$$

where

$$\begin{aligned} \langle \mathcal{P}(2, 2) \rangle &= \frac{1}{7} |2\sqrt{2}A_2 A_0 - \sqrt{3}A_1 A_1|^2 \\ \langle \mathcal{P}(2, 1) \rangle &= \frac{1}{7} |2\sqrt{3}A_2 A_{-1} - \sqrt{2}A_0 A_1|^2 \\ \langle \mathcal{P}(2, 0) \rangle &= \frac{1}{7} |2\sqrt{2}A_2 A_{-2} + \sqrt{2}A_1 A_{-1} - \sqrt{2}A_0 A_0|^2 \\ \langle \mathcal{P}(2, -1) \rangle &= \frac{1}{7} |2\sqrt{3}A_1 A_{-2} - \sqrt{2}A_0 A_{-1}|^2 \\ \langle \mathcal{P}(2, -2) \rangle &= \frac{1}{7} |2\sqrt{2}A_0 A_{-2} - \sqrt{3}A_{-1} A_{-1}|^2. \end{aligned}$$

Minimizing over  $A_\alpha$  (checked numerically), we find that depending on the parameters of our hamiltonian, we can have the possible phases

$$|\psi_A\rangle = \prod_i |2\rangle_i \quad (5.17)$$

$$|\psi_{B1}\rangle = \prod_i \left( \frac{1}{2} |-2\rangle_i + \frac{1}{\sqrt{2}} |0\rangle_i - \frac{1}{2} |2\rangle_i \right) \quad (5.18)$$

$$|\psi_{B2}\rangle = \prod_i \left( \sqrt{\frac{2}{3}} |-1\rangle_i + \sqrt{\frac{1}{3}} |2\rangle_i \right) \quad (5.19)$$

$$|\psi_C\rangle = \prod_i \left( \frac{1}{\sqrt{2}} \sin(\eta) |-2\rangle_i + \cos(\eta) |0\rangle_i + \frac{1}{\sqrt{2}} \sin(\eta) |2\rangle_i \right). \quad (5.20)$$

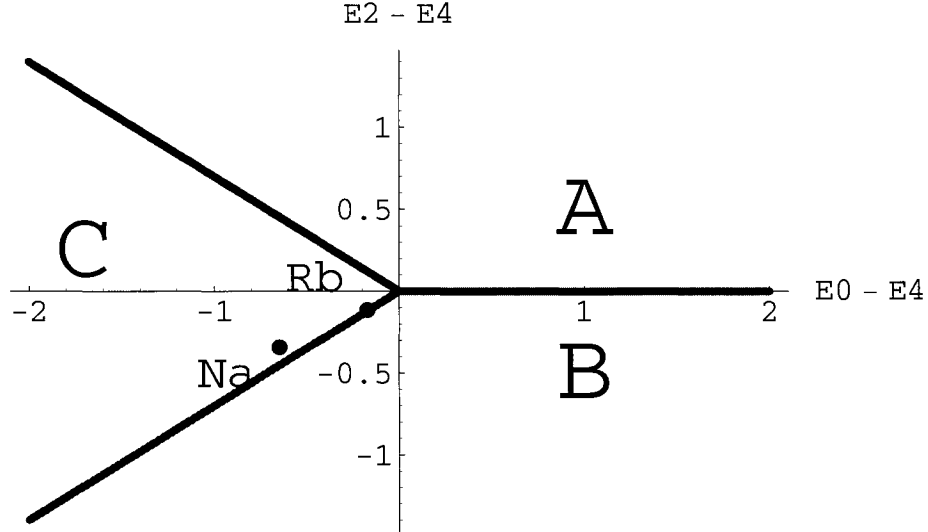


Figure 5.1: Phase diagram for spin two bosons. The  $x$  and  $y$  axes correspond to  $\epsilon_0 - \epsilon_4$  and  $\epsilon_2 - \epsilon_4$  respectively. Shown are the points for  $^{87}\text{Rb}$  and  $^{23}\text{Na}$ . The energy units are  $\frac{-4J^2}{U_0}$ .

These wave functions will maximize (or minimize)  $\langle \mathcal{P}(0) \rangle$  or  $\langle \mathcal{P}(2) \rangle$  which will be desirable if  $\epsilon_0 - \epsilon_4$  or  $\epsilon_2 - \epsilon_4$  is negative or positive. With these wavefunctions we find

$$\langle \psi_A | \mathcal{P}(0) | \psi_A \rangle = 0 ; \langle \psi_A | \mathcal{P}(2) | \psi_A \rangle = 0 \quad (5.21)$$

$$\langle \psi_B | \mathcal{P}(0) | \psi_B \rangle = 0 ; \langle \psi_B | \mathcal{P}(2) | \psi_B \rangle = \frac{4}{7} \quad (5.22)$$

$$\langle \psi_C | \mathcal{P}(0) | \psi_C \rangle = \frac{1}{5} ; \langle \psi_C | \mathcal{P}(2) | \psi_C \rangle = \frac{2}{7}. \quad (5.23)$$

Note that phases  $B1$  and  $B2$  are degenerate here and phase  $C$  is independent on the angle  $\eta$ . The resulting phase diagram is shown in Fig. 5.1. The phase boundaries are given by  $\epsilon_2 - \epsilon_4 = \pm \frac{7}{10}(\epsilon_0 - \epsilon_4)$  and  $\epsilon_2 = \epsilon_4$ .

Now we consider where particular Alkali atoms will lie in this diagram. For  $^{87}\text{Rb}$ , we have  $a_0 = 89.4a_B$ ,  $a_2 = 94.5a_B$ , and  $a_4 = 106a_B$ . This gives  $U_1/U_0 = -0.00172$  and  $U_2/U_0 = 0.0165$  so  $\epsilon_2 - \epsilon_4 = \frac{-4J^2}{U_0}0.114$  and  $\epsilon_0 - \epsilon_4 = \frac{-4J^2}{U_0}0.173$ . For  $^{23}\text{Na}$

the scattering lengths are  $a_0 = 34.9a_B$ ,  $a_2 = 45.8a_B$ , and  $a_4 = 64.5a_B$ . This gives  $U_1/U_0 = -0.0536$  and  $U_2/U_0 = 0.0496$  so  $\epsilon_2 - \epsilon_4 = \frac{-4J^2}{U_0}0.341$  and  $\epsilon_0 - \epsilon_4 = \frac{-4J^2}{U_0}0.646$ . We see that both of these points will lie in phase C in the diagram.

### 5.1.5 Characterizing the phases

We now set out to gain a better understanding of the the variational states found above. It turns out that finding the maximally polarized states which are orthogonal to these variational states will completely characterize the states. The maximally polarized state with coordinates  $\theta$  and  $\phi$  where

$$\langle F_x \rangle = F \sin(\theta) \cos(\phi) ; \quad \langle F_y \rangle = F \sin(\theta) \sin(\phi) ; \quad \langle F_z \rangle = F \cos(\theta) \quad (5.24)$$

is given by

$$|\zeta\rangle = \zeta^4 |-2\rangle + 2\zeta^3 |-1\rangle + \sqrt{6}\zeta^2 |0\rangle + 2\zeta |1\rangle + |2\rangle \quad (5.25)$$

where  $\zeta = e^{-i\phi} \tan(\theta/2)$  is the stereographic mapping of the complex plane to the unit circle. Note that this wave function is not normalized. This state can be found most easily by directly solving the eigenvalue problem

$$\mathbf{F} \cdot \hat{\mathbf{n}} |\zeta\rangle = F |\zeta\rangle \quad (5.26)$$

in the basis of states that are eigenvalues of  $F_z$  where  $\hat{\mathbf{n}} = (\sin(\theta) \cos(\phi), \sin(\theta) \sin(\phi), \cos(\theta))$  is a unit vector. In fact, for general spin  $F$ , we will have

$$|\zeta\rangle = \sum_{n=-F}^F \sqrt{\binom{F}{n}} \zeta^{F-n} |n\rangle. \quad (5.27)$$

Now, as indicated before, we want to find the states  $|\zeta\rangle$  for which  $\langle \zeta | \psi \rangle = 0$ , which will provide the symmetry properites of the wavefunction  $|\psi\rangle$ . For the spin

2 case, this will yield a polynomial of fourth degree, having four roots. The roots corresponding to phase A are degenerate, so this phase has only the symmetry of the rotation about the ferrmagnetic axis. Actually, developing such a technology is not necessary for phase A. On the other hand, the insights gained for phase B and C will turn out to be quite useful. For phase B1, the characteristic polynomial is

$$\langle \zeta | \psi_{B1} \rangle = \frac{1}{2}\zeta^4 + \sqrt{3}\zeta^2 - \frac{1}{2} = 0. \quad (5.28)$$

The roots of this equation lie at the vertices of a regular tetrahedron in the  $xyz$  coordinate system. Therefore, the symmetry of the wavefunction is that of the tetrahedron. Using this method, it is also found that phase B2 also transforms as a tetrahedron, and it can be obtained by rotating phase B1.

For phase C, our characteristic polynomial is

$$\frac{1}{\sqrt{2}}\sin(\eta)\zeta^4 + \sqrt{6}\cos(\eta)\zeta^2 + \frac{1}{\sqrt{2}}\sin(\eta) = 0. \quad (5.29)$$

The roots of this equation all lie at the vertices of a rectangle (within a given plane). For  $0 < \eta < \pi/3$ ,  $\pi/3 < \eta < 2\pi/3$ , and  $2\pi/3 < \eta < \pi$  the rectangle will lie in the  $zy$ ,  $xy$ , and  $xz$  planes respectively. For the special values  $\eta = n\pi/3$  for integer  $n$ , we will have two degenerate roots. This corresponds to a uniaxial nematic with a  $U(1)$  symmetry about the nematic axis and a  $Z_2$  inversion symmetry. Otherwise, the roots will be distinct and we will have a biaxial nematic.

## The nematic phase

We now consider the nematic phase B which has  $\langle F_{x,y,z} \rangle = 0$ . The order parameter of the nematic state is the matrix defined by

$$Q_{ab} = \frac{1}{2} (\langle F_a F_b \rangle + \langle F_b F_a \rangle) - \frac{1}{3} \delta_{ab} \langle F^2 \rangle. \quad (5.30)$$

If the eigenvalues of this  $3 \times 3$  matrix are distinct then we will have a biaxial nematic. Otherwise we will have a uniaxial nematic. Uniaxial nematics are much more common in nature. In addition, the biaxial nematic has non-Abelian defects. From the previous section, phase C is a nematic and the eigenvalues of  $Q_{ab}$  for this case are

$$\text{Eig}(Q_{ab}) = \left( -2 \cos(2\theta), \cos(2\theta) + \sqrt{3} \sin(2\theta), \cos(2\theta) - \sqrt{3} \sin(2\theta) \right). \quad (5.31)$$

From this, we see that depending on the value of  $\theta$ , we can either have a uniaxial or biaxial nematic. It is an interesting question to ask how can we access this range of  $\theta$  that will be a biaxial nematic experimentally.

### 5.1.6 The phase diagram with fixed magnetization with quadratic Zeeman splitting

In the previous section, we placed no constraints on  $\langle F_z \rangle$  during our minimizations. However, in real experiments the time it takes such a quantity to relax is longer than the lifetime of the condensate. This is reflected by the fact that  $F_z$  commutes with our model Hamiltonian. In this section, we will consider the possible phases for fixed magnetization  $\mathcal{M} \equiv \langle F_z \rangle / N$  and also under the presence of quadratic Zeeman splitting. We will consider phases A, B, and C separately.

### Quadratic Zeeman Effect

Experiments for spin one bosons in the presence of an external magnetic field was reviewed by Stamper-Kurn and Ketterle [144]. The Hamiltonian for a single atom in the presence of an external magnetic field is

$$\mathcal{H}_{\text{hf}} = \mathbf{AI} \cdot \mathbf{J} = \frac{A}{2}(F^2 - I^2 - J^2) - BS_z. \quad (5.32)$$

Here we have absorbed the factor of the Bohr magneton into the magnetic field giving  $B$  units of energy. We also point out that we have neglected the coupling of the external electric field to the nuclear spin since this is reduced by a factor on the order of  $m_e/m_p$  compared to the coupling of the electron. The energy eigenstates of this can be computed exactly. However, for our purposes we assume that  $A \gg B$  and compute the eigenvalues to order  $B^2$  which will give the linear and quadratic Zeeman splittings. Then to second order in  $B$ , the eigenenergies of the total spin two states will be

$$\begin{aligned} E(F = 2; F_z = 2) &= 3A - \frac{B}{2} \\ E(F = 2; F_z = 1) &= 3A - \frac{B}{4} + \frac{3B^2}{32A} \\ E(F = 2; F_z = 0) &= 3A + \frac{B^2}{8A} \\ E(F = 2; F_z = -1) &= 3A + \frac{B}{4} + \frac{3B^2}{32A} \\ E(F = 2; F_z = -2) &= 3A + \frac{B}{2}. \end{aligned} \quad (5.33)$$

We point out that these energies will be reproduced up to a constant by the hamiltonian acting in the  $F = 2$  subspace

$$\mathcal{H}' = -\frac{1}{2}BF_z - \gamma F_z^2. \quad (5.34)$$

where  $\gamma = \frac{B^2}{32A}$ . Since the total magnetization is conserved, we can neglect the linear term.

### Phase A

As seen in the previous section, the phases

$$(A_{-2}, A_{-1}, A_0, A_1, A_2) = (1, 0, 0, 0, 0) \text{ and } (0, 0, 0, 0, 1) \quad (5.35)$$

minimize the energy where we did not take into account any constraints on the magnetization. To enforce the constraint of mixed magnetization, we will use a Lagrange multiplier  $\mu$  which couples to the magnetization as  $-\mu\mathcal{M}$  where

$$\mathcal{M} = 2|A_2|^2 + |A_1|^2 - |A_{-1}|^2 - 2|A_{-2}|^2. \quad (5.36)$$

Using this, we find for the energy

$$E_A/N = -2|\mu| - 4\gamma. \quad (5.37)$$

The kink in the energy as a function of  $\mu$  implies phase separation. That is, for a fixed magnetization,  $\frac{N}{2}(1 - \frac{M}{2})$  of the atoms will be in the state  $(1, 0, 0, 0, 0)$  while  $\frac{N}{2}(1 + \frac{M}{2})$  will be in the state  $(0, 0, 0, 0, 1)$

### Phase B

In the previous section, we saw that for zero magnetization and for no quadratic Zeeman shift, the ground state is  $(-\frac{1}{2}, 0, \frac{1}{\sqrt{2}}, 0, \frac{1}{2})$ . It is important to note, however, that this state is degenerate with  $(0, \sqrt{\frac{2}{3}}, 0, 0, \frac{1}{\sqrt{3}})$ . It turns that both states are important for finite  $\gamma$  and  $\mu$ . It is found that the two states are sufficient to describe

phase B are

$$\text{B1 : } \quad (\sin(\theta) \sin(\phi) e^{i\alpha}, 0, \cos(\theta), 0, \sin(\theta) \cos(\phi) e^{-i\alpha}) \quad (5.38)$$

and

$$\text{B2 : } \quad \left( 0, \sqrt{\frac{2-\mathcal{M}}{3}} e^{i\alpha_1}, 0, 0, \sqrt{\frac{1+\mathcal{M}}{3}} e^{i\alpha_2} \right) \quad (5.39)$$

where the  $\alpha$ 's are arbitrary phases. This expression for B2 is only valid for  $\mu > 0$  which gives positive magnetization; it is easy to generalize to the case of negative magnetization. An analytic expression for the phase boundary can be obtained in the limit  $|\gamma|, |\mu| \ll |\epsilon_0 - \epsilon_4|, |\epsilon_2 - \epsilon_4|$  and is found to be

$$2\mu = \zeta\gamma \quad \zeta = \frac{(\epsilon_4 - \epsilon_2) - \frac{7}{10}(\epsilon_0 - \epsilon_4)}{(\epsilon_4 - \epsilon_2) + \frac{7}{10}(\epsilon_0 - \epsilon_4)}. \quad (5.40)$$

For  $2\mu < \zeta\gamma$  we will have phase B1 while for  $2\mu > \zeta\gamma$  we will have phase B2.

### Phase C

We found that for  $\mu = \gamma = 0$  the state  $(0, 0, 1, 0, 0)$  will minimize the energy. This is degenerate, however, with  $(\frac{1}{\sqrt{2}}, 0, 0, 0, \frac{1}{\sqrt{2}})$ . It is clear that the latter state will be favored for  $\gamma > 0$ . It is found that the state sufficient to describe phase C with finite magnetization and  $\gamma$  is

$$\text{C : } \quad \left( \sqrt{\frac{2-\mathcal{M}}{4}} e^{i\alpha_1}, 0, 0, 0, \sqrt{\frac{2+\mathcal{M}}{4}} e^{i\alpha_2} \right) \quad (5.41)$$

where  $\alpha_1$  and  $\alpha_2$  are arbitrary phases. This is the only relevant phase in region C.

### Example

Now that we have determined what happens to each of the phases for finite magnetization and quadratic Zeeman term, it is instructive to do an example. We consider



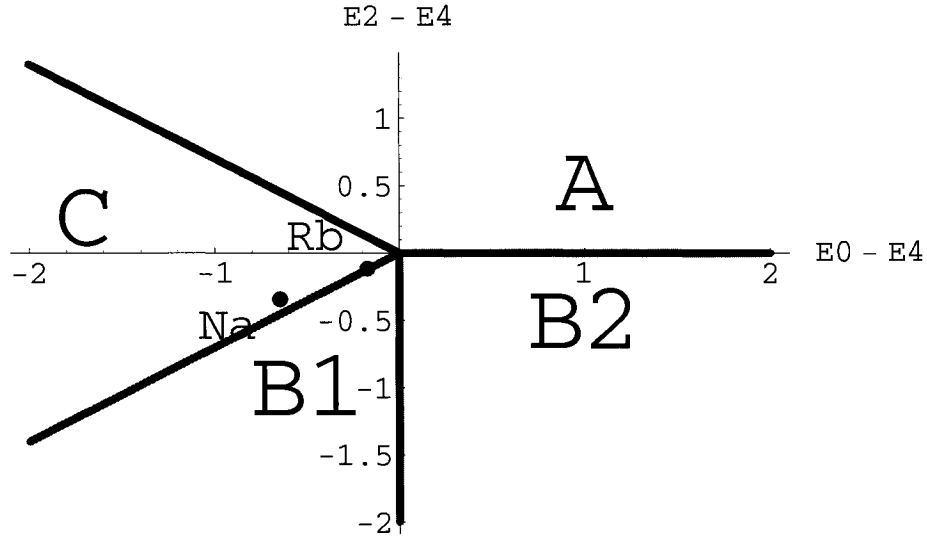


Figure 5.2: Phase diagram for  $2\mu = \gamma$ .

the case  $2\mu = \gamma$ . The resulting phase diagram is shown in Fig.5.2.

## 5.2 Dipolar molecules in an optical lattice

### 5.2.1 Introduction

In ultracold physics, systems with long-range dipolar interactions have recently attracted considerable attention both theoretically and experimentally (for a recent review of ultracold dipolar molecules see [39] and references therein). For atoms, dipolar interactions come from their magnetic moments and become important for large electronic spin [55]. Recent experiments demonstrated the relevance of such dipolar interactions for the expansion of Cr atoms from the BEC state [149]. On the other hand, for heteronuclear molecules, dipolar interactions arise from their

electric dipole moments. Recent experiments have succeeded in trapping and cooling several types of heteronuclear molecules [39, 145, 75, 134]. In a state with a well-defined angular momentum, molecules do not have a dipole moment. However, when an external electric field is used to polarize the molecules, dipolar moments can be induced. There has been considerable theoretical effort to study the resulting dipole interactions and many-body physics associated with such systems [169, 137, 37, 56, 117, 111].

Here, we consider an alternative mechanism for obtaining the  $1/r^3$  dipolar interactions, and the important concomitant directional character. Namely, we investigate a mixture of heteronuclear dipolar molecules in the lowest ( $\ell = 0$ ) and the first excited ( $\ell = 1$ ) rotational states. For such a system, the origin of the long-range interaction is the exchange of angular momentum quanta between molecules. We demonstrate that when loaded into an optical lattice, such mixtures can realize various kinds of non-trivial spin systems with anisotropic and long-range interactions. Several approaches for realizing spin systems using cold atoms have been discussed before, including bosonic mixtures in optical lattices in the Mott state [105, 41, 92, 76], interacting fermions in special lattices [32], and trapped ions interacting with lasers [38]. The system we consider has the practical advantages of the high energy scale for spin-dependent phenomena (set by dipolar interactions) and the new physics associated with the long-ranged nature of the dipole interactions. Experimental realization of the system will give insight into several open questions in condensed matter physics including competition between ferro and antiferroelectric orders in crystals [138, 103] and systems with frustrated spin interactions [114].

### 5.2.2 Hamiltonian definition/discussion

Consider the system that contains bosonic molecules in the lowest ( $\ell = 0, \ell_z = 0$ ) and first excited ( $\ell = 1, \ell_z = -1, 0, 1$ ) rotational states where we let  $s^\dagger$  and  $t_{-1,0,1}^\dagger$  create these respective states. We will often use the change of basis  $t_x^\dagger = (t_1^\dagger + t_{-1}^\dagger)/\sqrt{2}$ ,  $t_y^\dagger = -i(t_1^\dagger - t_{-1}^\dagger)/\sqrt{2}$ , and  $t_z^\dagger = t_0^\dagger$ . To describe molecules in an optical lattice we use the one-band Hubbard type effective model

$$\mathcal{H} = \mathcal{H}_{\text{kin}} + \mathcal{H}_{\text{Hub}} + \mathcal{H}_{\text{dip}}. \quad (5.42)$$

The first term on the right hand side of (5.42) is the kinetic energy from nearest-neighbor hopping  $\mathcal{H}_{\text{kin}} = -J \sum_{\langle ij \rangle} (s_i^\dagger s_j + t_{i\alpha}^\dagger t_{j\alpha} + \text{h.c.})$ . Operators  $s_i^\dagger$  and  $t_{i\alpha}^\dagger$  create molecules on site  $i$  (here and after the summation over repeating indices  $\alpha = x, y, z$  is implied). The last term in (5.42) describes the dipolar interaction between molecules from different sites

$$\mathcal{H}_{\text{dip}} = \frac{\gamma}{2} \sum_{i \neq j} \frac{d_{i\alpha} d_{j\alpha} - 3d_{i\alpha} e_{ij\alpha} d_{j\beta} e_{ij\beta}}{|\mathbf{R}_i - \mathbf{R}_j|^3} \quad (5.43)$$

where  $\mathbf{R}_i$  are lattice vectors,  $e_{ij\alpha}$  is the  $\alpha$ -component of the unit vector along  $\mathbf{R}_i - \mathbf{R}_j$ , and parameter  $\gamma$  equals  $2d^2/3$ , where  $d$  is the value of the dipole moment associated with the  $\ell = 0 \rightarrow \ell = 1$  transition, and  $d_i$  is the dipole moment operator at site  $i$ .

The  $\alpha$ -component of the operator  $\mathbf{d}_i$  is written as

$$d_{i\alpha} = s_i^\dagger t_{i\alpha} e^{-2iB_e t} + t_{i\alpha}^\dagger s_i e^{2iB_e t}, \quad (5.44)$$

where we absorbed the energy difference between the rotational levels  $E_{\ell=1} - E_{\ell=0} = 2B_e$  into the time dependence of the  $t$  operators. Since the rotational constant  $B_e$  is considerably larger than any other energy scale in the system, we assume that the terms in (5.43) that oscillate at frequencies  $\pm 4B_e$  average to zero. This forces the

number of molecules in the  $\ell = 0$  and  $\ell = 1$  states to be independently conserved.

Dropping such terms, (5.43) reduces to

$$\mathcal{H}_{\text{dip}} = \frac{\gamma}{2} \sum_{i \neq j} \frac{(s_i^\dagger t_{j\alpha}^\dagger s_j t_{i\beta} + \text{h.c.})(\delta_{\alpha\beta} - 3e_{ij\alpha}e_{ij\beta})}{|\mathbf{R}_i - \mathbf{R}_j|^3}. \quad (5.45)$$

The second term on the right hand side in (5.42) is the Hubbard on-site interaction. For two  $s$  molecules in the absence of an external electric field, the long-range part of their interaction potential is dominated by the van der Waals tail  $C_6/R^6$  originating from second order terms in the dipole-dipole interaction operator. For polar molecules with large static rotational polarizabilities one can estimate  $C_6 \approx -d^4/6B_e$ . For the RbCs molecule ( $d = 0.5$  a.u.,  $B_e = 7.7 \times 10^{-8}$  a.u.) we have  $C_6 \approx 1.5 \times 10^5$  a.u. For molecules with smaller dipole moments and larger rotational constants like, for example, CO ( $d = 0.043$ ,  $B_e = 9.0 \times 10^{-6}$ ), the van der Waals interaction is comparable in magnitude to interatomic forces. In any case the range of the potential, which scales as  $R_e = (mC_6)^{1/4}$ , is not much different from typical ranges of interatomic potentials (for RbCs it equals  $R_e \approx 400a_0$  where  $a_0$  is the Bohr radius). First order terms in the dipole-dipole operator are also absent for two molecules with  $\ell = 1$ . In this case, apart from a weak quadrupole-quadrupole contribution proportional to  $R^{-5}$ , the long-range part of the intermolecular potential is given by the van der Waals interaction with a comparable  $C_6$  coefficient. Thus, the interactions between molecules with the same  $\ell$  are all short ranged and, in an ultracold system, can be modeled by contact potentials. Then, averaging them over the Gaussian on-site wave functions gives the Hubbard on-site interaction.

The interaction between  $s$  and  $t_\alpha$  molecules (without loss of generality we consider  $\alpha = z$  here) is similar to the resonant interaction of an electronically excited atom

and a ground state atom. For even partial waves the intermolecular potential is asymptotically given by  $W_z(\mathbf{R}) = \gamma(1 - 3 \cos^2 \theta_z)/2R^3$ , where  $\theta_z$  is the angle between  $\mathbf{R}$  and the  $z$ -axis. We consider the weakly interacting regime where the characteristic energy scale of this interaction,  $\Delta E \sim \gamma l_0^{-3}$ , is smaller than the Bloch band separation. Here  $l_0$  is the oscillator length of the on-site harmonic confinement. Then, the two-body problem in a harmonic potential can be solved in the mean-field approximation by using the pseudopotential approach (see [170] and references therein). Due to the anisotropy of  $W_z(\mathbf{R})$  the corresponding on-site interaction energy,  $V_z$ , can be tuned at will by changing the aspect ratio of the on-site confinement [170].

We arrive at the following expression for  $\mathcal{H}_{\text{Hub}}$ :

$$\begin{aligned} \mathcal{H}_{\text{Hub}} = \sum_i & \left[ \frac{U}{2} n_{si}(n_{si} - 1) + \frac{U_\alpha}{2} n_{t_\alpha i}(n_{t_\alpha i} - 1) \right. \\ & \left. + \sum_{\alpha \neq \beta} U_{\alpha\beta} n_{t_\alpha i} n_{t_\beta i} + V_\alpha n_{si} n_{t_\alpha i} \right]. \end{aligned} \quad (5.46)$$

It is easy to see that (5.46) holds for arbitrary filling factors as long as the on-site density profiles remain Gaussian. However, for the purpose of this paper it is sufficient to consider on average one or two molecules per site, which also reduces inelastic losses. The ten coupling constants in Eq. (5) are virtually impossible to control independently. However, in certain cases not all of them are relevant. For instance, for a mixture of  $s$  and  $t_z$  molecules the relevant coupling constants are  $U$ ,  $U_z$ , and  $V_z$ . These are tunable through trap aspect ratio and/or Feshbach resonance. Another example is the Mott insulating state with one molecule per site. As long as the on-site interaction energies are much larger than  $J$ , the particular values of the coupling constants are not important and can be formally set to any desired values. For simplicity, let us restrict ourselves to the case  $U_x = U_y = U_z = U$ ,  $U_{\alpha\beta} = 0$ , and

$$V_x = V_y = V_z = V.$$

### 5.2.3 The Mott Insulating state

We now discuss the resulting phase diagram, first focusing our attention on the Mott insulating state. For this, each site contains an integer  $n$  number of molecules. We take the variational wave function

$$|\Psi_{\text{MI}}\rangle = \prod_i \frac{1}{\sqrt{n!}} \left( \cos(\theta) s_i^\dagger + \sin(\theta) \psi_{i\alpha} t_{i\alpha}^\dagger \right)^n |0\rangle \quad (5.47)$$

where  $\theta$  describes the fraction of the molecules excited into  $\ell = 1$  states and  $\psi_{i\alpha}$  is a normalized complex vector  $\psi_{i\alpha}^* \psi_{i\alpha} = 1$ . Here,  $\psi_{i\alpha}$  is the variational parameter which describes the direction the dipole moment points on site  $i$ . The variational wave function (5.47) is motivated by the observation that it maximizes the magnitude of the dipole moment in individual wells (which is desirable for the range of on-site parameters we consider), while preserving the freedom to choose their local directions. We point out that for such a variational wave function to be valid, the on-site  $|V|$  cannot be very much larger than  $\gamma$ , the dipolar interaction between neighboring sites. This allows us to construct variational states that benefit maximally from dipolar interactions. In all cases discussed below we verified the absence of phase separation by checking the eigenvalues of the compressibility matrix for  $s$  and  $t$  bosons [69]. Taking the expectation value of the dipole operator (5.44) with our variational wave function (5.47) we obtain

$$\langle d_{i\alpha} \rangle = n \sin(2\theta) |\psi_{i\alpha}| \cos(\varphi_{i\alpha} - 2B_e t) \quad (5.48)$$

where we have written  $\psi_{i\alpha} = |\psi_\alpha|e^{i\varphi_{i\alpha}}$ . Upon taking the expectation value of dipole Hamiltonian (5.45), we find for the dipolar energy

$$E_{\text{dip}} = \frac{\gamma n^2 \sin^2(2\theta)}{8} \times \sum_{i \neq j} \frac{(\psi_{i\alpha} \psi_{j\beta}^* + \text{c.c.})(\delta_{\alpha\beta} - 3e_{ij\alpha}e_{ij\beta})}{|\mathbf{R}_i - \mathbf{R}_j|^3}. \quad (5.49)$$

When minimizing the energy in (5.49) it is important to keep track of the conservation laws that may be present for certain experimental geometries and on the initial preparation of the system. We will now consider several examples of ordering in the Mott insulating state. Although the dipole interaction in all cases is described by (5.49) we will see that different preparation leads to very different types of order. Though all discussion in this work will be restricted to 2d, we emphasize that there are nontrivial results in the Mott insulating phase for the 1d and 3d cases as well. As the first example, we consider the square lattice in the  $xy$ -plane defined by vectors  $\mathbf{a}_1 = \hat{\mathbf{x}}$  and  $\mathbf{a}_2 = \hat{\mathbf{y}}$ . Due to cross-terms such as  $s^\dagger t_x^\dagger s t_y$  in the dipolar hamiltonian (5.45), we see that  $t_x$  molecules can be converted to  $t_y$  molecules and vice-versa. Thus,  $N_{t_x}$  and  $N_{t_y}$  are not conserved quantities, and, consequently, the only conserved quantities are  $N_s$  and  $N_{t_z}$ . Now consider preparing this system in a mixture of  $\ell = 0$  and  $\ell = 1, \ell_z = 1$  states. Then after the system relaxes, taking the constraints into account, we must have fixed  $\langle N_s \rangle = N \cos^2(\theta)$ ,  $\langle N_{t_x} \rangle + \langle N_{t_y} \rangle = N \sin^2(\theta)$ , and  $\langle N_{t_z} \rangle = 0$ . This gives the constraints on the variational wave function  $\psi_{iz} = 0$  and  $|\psi_x|^2 + |\psi_y|^2 = 1$ . We see that the dipoles are allowed to rotate freely in the  $xy$ -plane. For this case, the dipoles will choose to point head-to-tail in the direction of one of the bonds, while alternating in the other. Thus, it is straightforward to see that this gives the *ordering wave vector*  $\mathbf{q} = (0, \pi, 0)$  with  $\psi_{ix} = e^{i(\mathbf{q} \cdot \mathbf{R}_i + \varphi_0)}$  and  $\psi_{iy} = \psi_{iz} = 0$

where  $\varphi_0$  is an arbitrary phase corresponding to a change of phase of the time dependent oscillations of the dipolar moment described by (5.48). We point out that this configuration is degenerate to the one with dipoles pointing head-to-tail in the  $y$ -direction.

As the next example in two dimensions, we take the same lattice as in the previous example, but prepare the system in a mixture of  $\ell = 0$  and  $\ell = 1, \ell_z = 0$  states. Recalling that for this geometry, both  $N_s$  and  $N_{t_z}$  are conserved quantities, we find the constraint on the variational wave function  $\psi_{ix} = \psi_{iy} = 0$  and  $\psi_{iz} = e^{i\varphi_i}$ . With this constraint, the dipole interaction energy is

$$E_{\text{dip}} = \frac{\gamma n^2 \sin^2(2\theta)}{4} \sum_{i \neq j} \frac{\cos(\varphi_i - \varphi_j)}{|\mathbf{R}_i - \mathbf{R}_j|^3}. \quad (5.50)$$

Here, the dipoles are confined to point in the  $z$ -direction, and therefore cannot point head-to-tail. This gives antiferromagnetic ordering in all directions,  $\mathbf{q} = (\pi, \pi, 0)$ , with  $\psi_{iz} = e^{i(\mathbf{q} \cdot \mathbf{R}_i + \varphi_0)}$  where  $\varphi_0$  is an arbitrary phase.

For the final example for the Mott insulating state, we consider a lattice in the  $xz$ -plane given by  $\mathbf{a}_1 = \cos(\alpha)\hat{\mathbf{x}} + \sin(\alpha)\hat{\mathbf{z}}$  and  $\mathbf{a}_2 = -\sin(\alpha)\hat{\mathbf{x}} + \cos(\alpha)\hat{\mathbf{z}}$ . In addition, we consider breaking the degeneracy of the  $(\ell = 1, \ell_z = -1, 0, 1)$  states with an external static magnetic field in the  $z$ -direction which will introduce the term proportional to  $BL_z$  into our hamiltonian. Preparing the system in a superposition of  $\ell = 0$  and  $\ell = 1, \ell_z = 1$  states, we note that because of this degeneracy breaking, there will be no mixing between other angular momentum states. That is, we can completely neglect the  $t_{-1,0}$  states. This will give  $\psi_{ix} = -i\psi_{iy} = e^{i\varphi_i}/\sqrt{2}$  and  $\psi_z = 0$  which will confine our dipoles to rotate in the  $xy$ -plane as:  $\langle \mathbf{d}_i(t) \rangle = d_0 \cos(\varphi_i - 2B_e t)\hat{\mathbf{x}} + d_0 \sin(\varphi_i - 2B_e t)\hat{\mathbf{y}}$ .



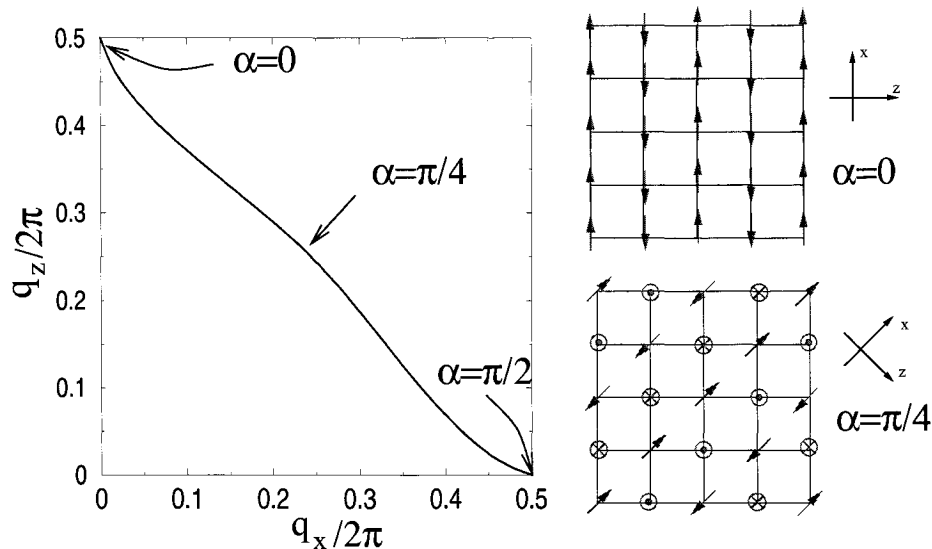


Figure 5.3: The ordering wave vector as the lattice is tilted by angle  $\alpha$ . As described in the text, for this situation a magnetic field is used to break the degeneracy between  $(\ell = 1, \ell_z = -1, 0, 1)$  states.

The dipolar energy of this system is therefore

$$E_{\text{dip}} = \frac{\gamma n^2 \sin^2(\theta)}{8} \sum_{i \neq j} \frac{\cos(\varphi_i - \varphi_j) (1 - \frac{3}{2} e_{ijx}^2)}{|\mathbf{R}_i - \mathbf{R}_j|^3}. \quad (5.51)$$

We use the ansatz  $\varphi_i = \mathbf{q} \cdot \mathbf{R}_i + \varphi_0$  to find the minimum of this dipolar energy for a particular lattice defined by the angle  $\alpha$ , and the results are summarized in Fig. 5.3.

#### 5.2.4 The superfluid state

We now consider melting the Mott insulator, and entering the superfluid (SF) state. An interesting question to consider is what happens to the ordering wave vector as the Mott insulating state is melted? For instance, deep in the superfluid phase, we will have  $q = 0$  which is favorable for Bose-Einstein condensation while we saw that antiferromagnetic ordering is typically favored in the Mott insulating state

by dipolar interactions. One possibility is that the wave vector interpolates smoothly between these two extremes as the hopping  $J$  increases. Another possibility is that the molecules in the  $s$  and  $t$  states phase-separate. We will show below that both scenarios are possible depending on on-site energy parameters in our original hamiltonian. For simplicity, we restrict our attention to the third example we discussed above for the Mott insulating state which was a two dimensional lattice in the  $xy$  plane prepared with  $\sigma_z$  polarized light. For further simplicity, we take  $\langle N_s \rangle = \langle N_{t_z} \rangle = N/2$ . As we saw before, we can neglect populating the  $t_x$  and  $t_y$  states, and this phase has antiferromagnetic  $\mathbf{q} = (\pi, \pi, 0)$  order in the Mott insulating phase.

Allowing for noninteger occupation per site motivates the variational wave function

$$|\Psi\rangle = \prod_i \left( \sum_{n=0}^{\infty} \alpha_n \frac{(a_i^\dagger)^n}{\sqrt{n!}} \right) |0\rangle \quad (5.52)$$

where

$$a_i^\dagger = \cos(\theta) e^{i\mathbf{p}_s \cdot \mathbf{R}_i} s_i^\dagger + \sin(\theta) e^{i\mathbf{p}_t \cdot \mathbf{R}_i} t_{iz}^\dagger. \quad (5.53)$$

and normalization requires  $\sum_n |\alpha_n|^2 = 1$  (compare with (5.47)). As before, this wave function maximizes the dipole energy for a given site which is energetically favorable.

We can now use a canonical transformation to write our original hamiltonian in terms of the boson operators  $a_i^\dagger$  (defined above) and  $b_i^\dagger = -\sin(\theta) e^{i\mathbf{p}_s \cdot \mathbf{R}_i} s_i^\dagger + \cos(\theta) e^{i\mathbf{p}_t \cdot \mathbf{R}_i} t_{iz}^\dagger$  (a new variable resulting from the transformation), and drop the terms which give zero when evaluated using the above variational wave function (5.52). This leads to the following single-site mean field hamiltonian

$$\mathcal{H}_{\text{MF}} = -2J \sum_{\alpha=x,y} \sqrt{\cos^4(\theta) + \sin^4(\theta) + 2 \cos^2(\theta) \sin^2(\theta) \cos(q_\alpha)} \left( a^\dagger \langle a \rangle + a \langle a^\dagger \rangle - \langle a^\dagger \rangle \langle a \rangle \right)$$

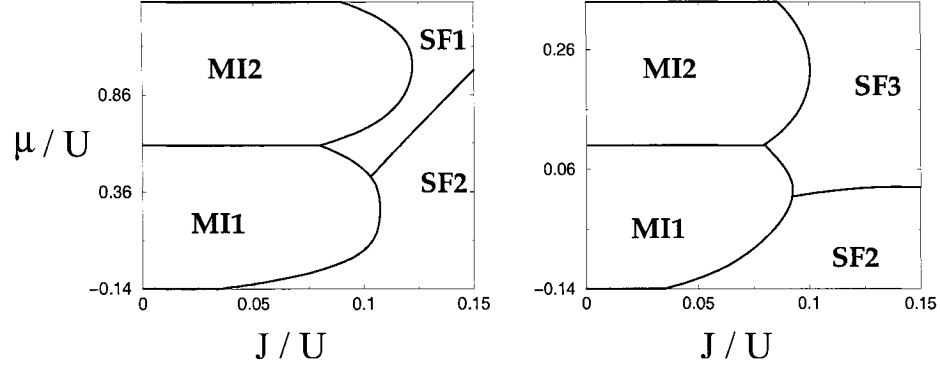


Figure 5.4: The phase diagram for  $V = U$  (left) and  $V = 0$  (right). For both cases, the dipolar interaction strength was fixed at  $\gamma = U/5$ . Shown are the antiferromagnetic MI states with one and two bosons per site labeled MI1 and MI2. SF1 and SF2 correspond to superfluid states with partial and complete phase separation (described in text). SF3 is a superfluid phase with no phase separation which has an ordering wave vector that interpolates between the Mott insulating and deep superfluid regime.

$$\begin{aligned}
 & + \frac{\gamma}{4} \sin^2(2\theta) (2n_a \langle n_a \rangle - \langle n_a \rangle^2) \sum_{\mathbf{R}_i \neq 0} \frac{\cos(\mathbf{q} \cdot \mathbf{R}_i)}{|\mathbf{R}_i|^3} + \frac{1}{2} U n_a (n_a - 1) \\
 & + \frac{1}{4} (V - U) \sin^2(2\theta) n_a (n_a - 1)
 \end{aligned} \tag{5.54}$$

where  $n_a = a^\dagger a$  and we have already performed the minimization over the center of mass momentum  $\mathbf{p} = (\mathbf{p}_t + \mathbf{p}_s)/2$ . The ground state of this hamiltonian for fixed  $\theta$  (relative concentrations) and  $\mathbf{q} = \mathbf{p}_t - \mathbf{p}_s$  (relative momentum) can be determined self-consistently in  $\langle a \rangle$  and  $\langle n_a \rangle$  through iteration numerically. The general approach will then be to minimize these ground state energies over  $q_{x,y} \in [0, \pi]$  and  $\theta \in [0, \pi/2]$ . When the minimum occurs for  $\theta \neq \pi/4$ , phase separation will occur.

The resulting phase diagrams are shown in Fig. 5.4. The Mott insulating phases are antiferromagnetically aligned and were discussed in the previous section. SF1 corresponds to partial phase separation where part of the lattice will have a larger concentration of  $s$  molecules while the other part will have a higher concentration of  $t$  molecules. Recall that phase separation will occur for when  $\theta \neq \pi/4$  since we initially

prepare the system to have equal populations of molecules in the  $s$  and  $t_z$  states. The region with more  $s$  molecules will have  $(p_s)_{x,y} = 0$  and  $(p_t)_{x,y} = \pi$ . This will allow the more populated  $s$  species to benefit maximally from BEC which prefers zero wave vector while still giving  $q_{x,y} = \pi$  which is preferred for the dipole interaction. The similar situation holds for the region of the lattice with a higher concentration of  $t_z$  molecules. SF2 corresponds to the case where the  $s$  and  $t_z$  molecules completely phase separate. Since the dipole interaction is negligible for this case, we will have  $(p_s)_{x,y} = (p_t)_{x,y} = 0$  which will favor BEC. Finally, SF3 corresponds to the case mentioned above where the wave vector  $\mathbf{q}$  interpolates between the deep superfluid and Mott insulating states ( $0 < q_{x,y} < \pi$ ) for which no phase separation occurs ( $\theta = \pi/4$ ).

### 5.2.5 Conclusion

In conclusion, we have shown that polar molecules prepared in a mixture of two rotational states can exhibit long-range dipolar interactions in the absence of an external electric field. We have described several novel Mott insulating and superfluid phases that can be realized as a result of such an interaction. Such states can be detected by Bragg scattering or by time-of-flight expansion [4].

### 5.2.6 Acknowledgements

This work was supported by the NSF grant DMR-0132874, the Harvard-MIT CUA, and the Harvard-Smithsonian ITAMP. We thank B. Halperin, R. Krems, A. Polkovnikov, D.W. Wang, and P. Zoller for useful discussions.

# Appendix A

## Appendices for Chapter 2

### A.1 The electron-phonon coupling vertices

The electron-phonon coupling matrix is given by

$$M_{k\tau k'\tau'\mu} = N \langle \psi_{k\tau} | \sum_i \frac{\partial V}{\partial \mathbf{R}_{0i}} \cdot \hat{\epsilon}_{q\mu}(i) | \psi_{k'\tau'} \rangle. \quad (\text{A.1})$$

One can see that the above expression can be evaluated by using the finite difference formula

$$M_{k\tau k'\tau'\mu} = \frac{1}{u} \langle \psi_{k\tau} | (V^{q\mu} - V_0) | \psi_{k'\tau'} \rangle. \quad (\text{A.2})$$

A method for calculating this expression with a plane-wave basis set was previously developed.[93] This section will be devoted to describing how to calculate  $M_{k\tau k'\tau'\mu}$  with a tight-binding method. We introduce the standard tight-binding notation

$$|\psi_{k\tau}\rangle = \sum_{il} A_{k\tau il} |\chi_{kil}\rangle \quad (\text{A.3})$$

$$|\chi_{kil}\rangle = \frac{1}{\sqrt{N}} \sum_n e^{ik \cdot R_n} |\phi_{nil}\rangle. \quad (\text{A.4})$$

Here  $n$  runs over unit cells and  $i$  runs over basis vectors in the unit cell and  $l$  over orbital type. Because the kinetic energy operator will be the same in the perturbed and unperturbed Hamiltonians, we can write

$$M_{k\tau k'\tau'\mu} = \frac{1}{u} \langle \psi_{k\tau} | (H^{q\mu} - \varepsilon_F) | \psi_{k'\tau'} \rangle. \quad (\text{A.5})$$

The reason why we keep the  $\varepsilon_F$  term which clearly is zero through orthogonality will become clear below. Expanding the wave functions in the tight-binding basis set, we obtain

$$M_{k\tau k'\tau'\mu} = \frac{1}{u} \sum_{ii'l'} A_{k\tau il}^* \langle \chi_{kil} | (H^{q\mu} - \varepsilon_F) | \chi_{k'i'l'} \rangle A_{k'\tau' i'l'}. \quad (\text{A.6})$$

Now, we write  $|\chi_{kil}^{q\mu}\rangle = |\chi_{kil}\rangle + |\delta\chi_{kil}^{q\mu}\rangle$  where the orbitals of  $|\chi_{kil}^{q\mu}\rangle$  are centered on the perturbed lattice. Inserting this into the above equation, we obtain

$$\begin{aligned} M_{k\tau k'\tau'\mu} &= \frac{1}{u} \sum_{ii'l'} A_{k\tau il}^* (\langle \chi_{kil}^{q\mu} | (H^{q\mu} - \varepsilon_F) | \chi_{k'i'l'}^{q\mu} \rangle \\ &\quad - (\langle \delta\chi_{kil}^{q\mu} | (H^{q\mu} - \varepsilon_F) | \chi_{k'i'l'} \rangle + \text{h.c.})) A_{k'\tau' i'l'}. \end{aligned} \quad (\text{A.7})$$

In the second term we can do the substitution  $H^{q\mu} \rightarrow H_0$  because the effect of doing this will be second order in  $u$  and we are interested in an expression that is accurate to first order. Then, this term will be

$$\begin{aligned} &\sum_{ii'l'} A_{k\tau il}^* (\langle \delta\chi_{kil} | (H - \varepsilon_F) | \chi_{k'i'l'} \rangle + \text{h.c.}) A_{k'\tau' i'l'} \\ &= \sum_{il} A_{k\tau il}^* \langle \delta\chi_{kil} | (H - \varepsilon_F) | \psi_{k'\tau'} \rangle + \text{h.c.} = 0. \end{aligned} \quad (\text{A.8})$$

So we finally have the expression

$$M_{k\tau k'\tau'\mu} = \frac{1}{u} \sum_{ii'l'} A_{k\tau il}^* \langle \chi_{kil}^{q\mu} | (H^{q\mu} - \varepsilon_F) | \chi_{k'i'l'}^{q\mu} \rangle A_{k'\tau' i'l'}. \quad (\text{A.9})$$

This expression can be computed by evaluating the tight-binding Hamiltonian and overlap matrices for the distorted lattice, evaluating the coefficients  $A_{k\tau il}$  and  $A_{k'\tau' i'l'}$

of the wave functions for the undistorted lattice, and performing the above sum. There is a slight technical problem with the above method because  $k$  and  $k'$  are not the same in the tight-binding matrix. However, it can be shown that the correct result will be obtained by using  $\langle \chi_{kil}^{q\mu} | H^{q\mu} | \chi_{ki'l'}^{q\mu} \rangle$  and  $\langle \chi_{kil}^{q\mu} | \chi_{ki'l'}^{q\mu} \rangle$  for the tight-binding and overlap matrices (or the similar expression with  $k \rightarrow k'$ ) in the limit of a large supercell. That is, when the distance over which neighboring atoms interact is small compared to the length of a unit cell, this method becomes exact. When we apply this method, we checked for convergence of the coupling as a function of the unit cell size.

## A.2 Isotropic Eliashberg equations in 1D

Obtaining quantitative parameters of superconductors described by the BCS theory like the transition temperature and the wave vector-dependent superconducting gap from microscopic models has developed into a powerful tool for understanding experimentally realized systems as well as even predicting new superconductors.[29] Though excellent review articles exist, [3, 130] we will establish the key results of the theory below in attempt to be as self-contained as possible. We will also show how to incorporate the electron-phonon coupling into the phonon parameters which become important in 1d due to the CDW instability.

In the following to simplify notation, we will consider a single band system only. The central ingredient which, in principle, allows one to calculate the superconducting transition temperature to high accuracy is Migdal's theorem [112] which allows one

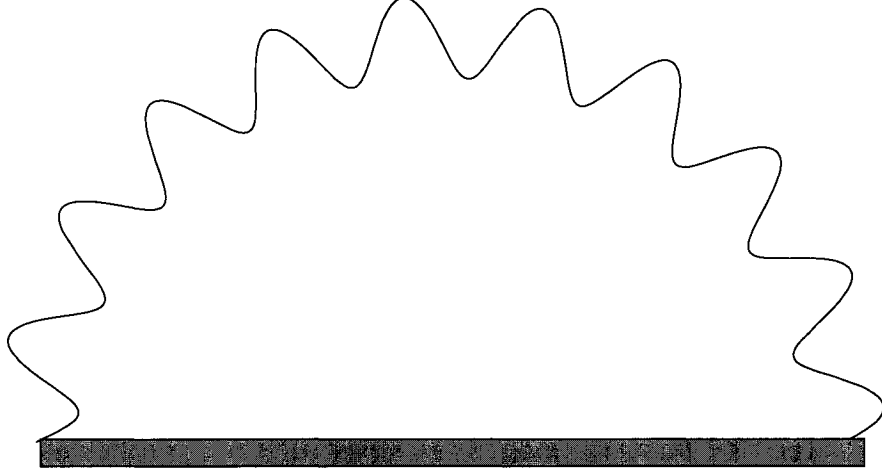


Figure A.1: Migdal's expression for the electronic self-energy. The thick line denotes the dressed electronic Green's function and the wavy line denotes the phonon Green's functions.

to evaluate the electron self-energy with small error as

$$\begin{aligned} \Sigma(k, i\omega_n) = & -\frac{1}{\beta} \sum_{k'n'\mu} \tau_3 \mathbf{G}(k', i\omega_{n'}) \tau_3 |g_{kk'\mu}|^2 \\ & \times D_{0\mu}(k - k', n - n'). \end{aligned} \quad (\text{A.10})$$

This expression for the self-energy is shown in Fig. A.1. In this equation,  $\beta$  is inverse temperature,  $\tau_i$  are Pauli matrices ( $i = 0$  gives the identity matrix while  $i = 1, 2, 3$  give the  $x, y, z$  Pauli matrices respectively),  $D_0$  is the noninteracting phonon Green's function, and  $\omega_n = \pi(2n + 1)/\beta$  are the fermionic Matsubara frequencies. The electronic Nambu-Green's function, a  $2 \times 2$  matrix, is given by  $\mathbf{G}(k, i\omega_n) = (i\omega_n \tau_0 - \varepsilon_k \tau_3 - \Sigma)^{-1}$ .

Now, we can expand  $\Sigma$  in terms of Pauli matrices

$$\Sigma = (1 - Z)i\omega_n \tau_0 + \phi \tau_1. \quad (\text{A.11})$$

We did not include the  $\tau_3$  term because this just shifts the quasiparticle energies and similarly we neglected the  $\tau_2$  term which can be eliminated by a proper choice of



phase for  $\phi$ . Written in terms of these parameters, the Green's function becomes

$$\mathbf{G} = -\frac{Zi\omega_n\tau_0 + \varepsilon_k\tau_3 + \phi\tau_1}{(Z\omega_n)^2 + \varepsilon_k^2 + \phi^2}. \quad (\text{A.12})$$

Inserting this into A.10 we obtain

$$\begin{aligned} \Sigma &= \frac{1}{\beta} \sum_{k'n'\mu} \frac{Z'i\omega_{n'}\tau_0 + \varepsilon_{k'}\tau_3 - \phi'\tau_1}{(Z'\omega_{n'})^2 + \varepsilon_{k'}^2 + \phi'^2} \\ &\times |g_{kk'\mu}|^2 D_{0\mu}(k - k', n - n'). \end{aligned} \quad (\text{A.13})$$

Now, we insert the identity  $\int d\varepsilon \delta(\varepsilon - \varepsilon'_k)$  into the above expression to obtain

$$\begin{aligned} \Sigma &= \frac{1}{\beta} \int d\varepsilon \sum_{k'n'\mu} \delta(\varepsilon - \varepsilon_k) \frac{Z'i\omega_{n'}\tau_0 + \varepsilon\tau_3 - \phi'\tau_1}{(Z'\omega_{n'})^2 + \varepsilon^2 + \phi'^2} \\ &\times |g_{kk'\mu}|^2 D_{0\mu}(k - k', n - n'). \end{aligned} \quad (\text{A.14})$$

The Lorentzian term in the integrand peaks very strongly at  $\varepsilon = \varepsilon_F = 0$  with width on the order of temperature. Assuming that the rest of the integrand doesn't vary as rapidly about  $\varepsilon = 0$ , we can replace  $\delta(\varepsilon - \varepsilon_{k'})$  with  $\delta(\varepsilon_{k'})$  and perform the  $\varepsilon$  integral to obtain

$$\Sigma = \frac{\pi}{\beta} \sum_{k'n'\mu} \delta(\varepsilon_{k'}) \frac{Z'i\omega_{n'}\tau_0 - \phi'\tau_1}{\sqrt{(Z'\omega_{n'})^2 + \phi'^2}} |g_{kk'\mu}|^2 D_{0\mu}(k - k', n - n'). \quad (\text{A.15})$$

This approximation can be seen to break down for small momentum (forward) scattering due to acoustic phonons. This case will be discussed in Appendix A.3. When close to  $T_{\text{SC}}$ ,  $\phi'$  will be small and can be neglected in the denominator of A.15.

Now we perform the so-called isotropic approximation. Multiply both sides of A.15 by  $\delta(\varepsilon_k)/\nu_\sigma(0)$  where  $\nu_\sigma(0)$  is the density of states at the Fermi level per spin and sum over  $k$ . In the right-hand side of A.15 we then replace  $Z(k', n')$  and  $\phi(k', n')$  with their Fermi-surface averages  $Z_{n'}$  and  $\phi_{n'}$ . This approximation is valid when the

Fermi-surface is fairly isotropic. Now by equating the coefficients of the matrices  $\tau_0$  and  $\tau_1$  we finally arrive at the equations

$$Z_n = 1 + f_n s_n \sum_{n'} \lambda(n - n') s_{n'} \quad (\text{A.16})$$

$$Z_n \Delta_n = \sum_{n'} (\lambda(n - n') - \mu_{\text{SC}}^*) f_{n'} \Delta_{n'} \quad (\text{A.17})$$

where  $f_n = 1/|2n + 1|$ ,  $s_n = \text{sgn}(2n + 1)$ ,  $\Delta_n = \phi_n/Z_n$ , and

$$\lambda(n - n') = -\frac{1}{\nu_\sigma(0)} \sum_{kk'\mu} \delta(\varepsilon_k) \delta(\varepsilon_{k'}) |g_{kk'\mu}|^2 D_{0\mu}(k - k', n - n'). \quad (\text{A.18})$$

The Coulomb pseudopotential  $\mu_{\text{SC}}^*$  was inserted to account for the bare electron-electron interaction that is not included in our original Hamiltonian Eq. (4.1). The superconducting transition temperature  $T_{\text{SC}}$  is the temperature at which nontrivial solutions for the gap  $\Delta_n$  begin to appear. Equations (A.16), (A.17), and (A.18) are known as the isotropic Eliashberg equations.[46] Input parameters have been calculated and the Eliashberg equations have been solved to calculate  $T_{\text{SC}}$  for a variety of superconductors described by the BCS theory. We also note that a generalization to the case where the Fermi surface is anisotropic is straightforward.[2]

Now, for typical three-dimensional solids the phonon frequencies are affected very little by the electron-phonon coupling. Therefore, the above formalism where we have used the non-interacting phonon Green's function  $D_{0\mu}$  works remarkably well in 3d. This is not the case, however, in 1d where one is encountered with the CDW instability. A more accurate phonon Green's function is given by

$$D_\mu(k, n) = \frac{2\Omega_{q\mu}^0}{(i\nu_n)^2 - (\Omega_{q\mu})^2} \quad (\text{A.19})$$

where  $\Omega_{q\mu}^0$  is the undressed frequency (without electron-phonon coupling) and  $\Omega_{q\mu}$  is the dressed frequency (which, as seen above can have strong temperature depen-

dence). Calculating the dressed phonon Green's function can be challenging because one needs both  $\Omega_{q\mu}^0$  and  $\Omega_{q\mu}$ . However, we notice that when we substitute Eq. (A.19) into Eq. (A.18) we have the fortuitous cancellation of  $\Omega_{q\mu}^0$  in the numerator of  $D_\mu(k, n)$  with that in the denominator of  $|g_{kk'\mu}|^2$ . Thus one sees that knowledge of the undressed frequencies (which are significantly more difficult to obtain) will not be necessary to construct the Eliashberg equations. By doing the substitution  $\Omega_q^0 \rightarrow \Omega_{q\mu}$  in Eqns. (A.16), (A.17), and (A.18), one can thereby construct the “dressed” Eliashberg equations which takes into account the influence of the electron-phonon coupling on the phonon frequencies which is important in 1d.

Note also that since some modes will have temperature dependence, the Eliashberg equations must be solved self consistently. That is, we must find a temperature such that the SC transition temperature determined from the Eliashberg equations is the same as the temperature used for the input dressed phonon frequencies. This can be done by iteration. Furthermore, this method allows us to tell which will be the dominant phase at low temperature of our system. If we find a self-consistent solution of the Eliashberg equations and  $T_{\text{SC}} > T_{\text{CDW}}$ , then superconductivity will be the dominant correlation. Otherwise, the system will prefer the CDW state.

Finally, we will write down an expression which approximately solves the Eliashberg equations, originally developed by McMillan

$$T_{\text{SC}} = \frac{\langle \Omega \rangle}{1.20} \exp \left[ -\frac{1.04(1 + \lambda_{\text{SC}})}{\lambda_{\text{SC}} - \mu_{\text{SC}}^*(1 + 0.62\lambda_{\text{SC}})} \right] \quad (\text{A.20})$$

where  $\lambda_{\text{SC}} \equiv \lambda(0)$ . From the above analysis, we see that to be self-consistent, one should use the dressed frequencies to evaluate  $\lambda_{\text{SC}}$ .

### A.3 Incorporating $q \approx 0$ scattering from acoustic phonons in the Eliashberg equations.

In this Appendix, we discuss in detail the role of acoustic phonons for small-radius nanotubes. Earlier theoretical analysis of the electron-phonon interactions in 1d systems suggested that acoustic phonons can play a dominant role in stabilizing the superconducting state.[102, 36] We will show, however, that since the dominant coupling comes from optical modes, that this effect is not important for the CNTs we study.

We now consider explicitly the contributions to  $q \approx 0$  scattering processes coupled to acoustic phonon modes which are not accounted for in the approximations leading to A.15. For the electron-phonon coupling to acoustic modes, we take

$$|g_{q\mu}|^2 = \frac{\gamma|q|/L}{1 + (q/q_0)^2} \quad (\text{A.21})$$

where  $q_0$  is a cut-off of order  $k_F$  and  $L$  is the system length. We also take  $\Omega_{q\mu} = c|q|$  and  $\varepsilon_k = v_F(|k| - k_F)$ . Inserting these quantities into A.10, setting  $Z = 1$  for simplicity, we obtain for the off-diagonal element

$$\begin{aligned} \Delta_n^{(q \approx 0)} &= \frac{1}{\beta} \sum_{n'} \frac{1}{2\pi} \int dq \frac{\Delta_{n'}}{\omega_{n'}^2 + (v_F q)^2} \\ &\times \frac{\gamma|q|}{1 + (q/q_0)^2} \cdot \frac{2c|q|}{(\omega_n - \omega_{n'})^2 + (c|q|)^2} \end{aligned} \quad (\text{A.22})$$

This integral can be evaluated to give

$$\begin{aligned} \Delta_n^{(q \approx 0)} &= \frac{\gamma}{v_F \beta} \sum_{n'} \frac{\Delta_{n'}}{|\omega_{n'}|c + |\omega_n - \omega_{n'}|v_F} \\ &\times \frac{q_0}{|\omega_n - \omega_{n'}|/c + q_0} \cdot \frac{q_0}{|\omega_n - \omega_{n'}|/v_F + q_0}. \end{aligned} \quad (\text{A.23})$$

One then sees that scattering from  $q \approx 0$  acoustic phonons gives an approximate contribution to  $\lambda_{\text{SC}}$  (when  $n = n'$ ) of  $\lambda_{\text{SC}}^{(q \approx 0)} = \gamma / (\pi v_F c)$ .

Now we consider the  $q \approx 2k_F$  scattering process from the same acoustic phonon. For this process we obtain

$$\begin{aligned} \Delta_n^{(q \approx 2k_F)} &\approx \frac{1}{\beta} \sum_{n'} |g_{q=2k_F, \mu}|^2 D(2k_F, n - n') \\ &\times \frac{L}{2\pi} \int dq \frac{\Delta_{n'}}{\omega_{n'}^2 + (v_F q)^2}. \end{aligned} \quad (\text{A.24})$$

This integral can be evaluated to give

$$\Delta_n^{(q \approx 2k_F)} = \frac{4\gamma c k_F^2}{\beta v_F} \sum_{n'} \frac{1}{(\omega_n - \omega_{n'})^2 + (c2k_F)^2} \frac{1}{|\omega_{n'}|}. \quad (\text{A.25})$$

One then finds that this gives a contribution of  $\lambda_{\text{SC}}^{(q \approx 2k_F)} = \gamma / (\pi v_F c)$  to  $\lambda_{\text{SC}}$  which is exactly the same as the  $q \approx 0$  scattering contribution. Thus one sees that  $q \approx 0$  scattering from acoustic phonons can be very important in one-dimensional electron-phonon systems. From such a process the so-called Wentzel-Bardeen instability [164, 9, 49] can occur which has recently been studied in the context of CNTs.[36] We also note that a similar analysis can be carried out for the optical phonons, and it is found that the  $q \approx 0$  processes are much smaller than the  $q \approx 2k_F$  process.

With the above method, we now see how to include the contribution from  $q \approx 0$  scattering into  $\lambda_{\text{SC}}$ . To do this, we simply double the contributions to  $\lambda_{\text{SC}}$  from  $2k_F$  processes which couple to acoustic phonons to include the  $q \approx 0$  contribution. In practice, we find that using this procedure actually changes  $\lambda_{\text{SC}}$  by only a small amount. For instance, for the (5,0) CNT,  $\lambda_{\text{SC}}$  only increases by less than 1%. This is because the dominant contributions to  $\lambda_{\text{SC}}$  are from coupling to the optical modes as discussed in Sec. 4.3.

We also point out that presence of the Wentzel-Bardeen singularity would significantly renormalize the acoustic phonon mode frequencies of the CNTs. The fact that the calculated phonon frequencies using the frozen-phonon approximation for the CNTs are quantitatively similar to the analogous modes of graphene as shown in Figs. 4.7, 4.9, and 4.11 further supports the notion that the Wentzel-Bardeen instability is unimportant in these systems.

## A.4 Limitations of non self-consistent method

In this Appendix, we will discuss the limitations of using a method in which the charge density is not evaluated self-consistently. For simplicity, we will neglect the contribution from the exchange-correlation energy  $E_{XC}$  in the Kohn Sham energy functional.

First we will consider the case of the equilibrium lattice structure. For this, the self-consistent total energy is given by

$$E_{SC}^{eq} = \sum_i \langle \psi_i | \left( \frac{\mathbf{p}^2}{2m} + V_{ion}^{eq}(\mathbf{r}) + \frac{1}{2} \int d^3r' \frac{n(\mathbf{r}')}{|\mathbf{r} - \mathbf{r}'|} \right) | \psi_i \rangle + E_{ion-ion}^{eq} \quad (A.26)$$

where the charge-density is given by  $n(\mathbf{r}) = \sum_i |\psi_i(\mathbf{r})|^2$ ,  $V_{ion}^{eq}$  is the ionic potential, and  $E_{ion-ion}^{eq}$  is the ion-ion interaction. In the above and in what follows, the  $i$  summation is carried out only over occupied electronic states. Applying the variational principle to Eq. A.26 gives the equation for the wave functions  $|\psi_i\rangle$  and therefore the charge-density  $n(\mathbf{r})$

$$\mathcal{H}^{eq}[n] |\psi_i\rangle = \varepsilon_i |\psi_i\rangle \quad (A.27)$$

where

$$\mathcal{H}^{\text{eq}}[n] = \frac{\mathbf{p}^2}{2m} + V_{\text{ion}}(\mathbf{r}) + \int d^3r' \frac{n(\mathbf{r}')}{|\mathbf{r} - \mathbf{r}'|}. \quad (\text{A.28})$$

In solving this equation, the charge density  $n(\mathbf{r})$  entering  $\mathcal{H}^{\text{eq}}[n]$  must be determined self-consistently to agree with the eigenfunctions  $\psi_i$ . Using this, the self-consistent total energy for the equilibrium lattice is determined to be

$$E_{\text{SC}}^{\text{eq}} = \sum_i \langle \psi_i | \mathcal{H}^{\text{eq}}[n] | \psi_i \rangle + F^{\text{eq}}[n] \quad (\text{A.29})$$

where

$$F^{\text{eq}}[n] = -\frac{1}{2} \int d^3r d^3r' \frac{n(\mathbf{r})n(\mathbf{r}')}{|\mathbf{r} - \mathbf{r}'|} + E_{\text{ion-ion}}^{\text{eq}}. \quad (\text{A.30})$$

to be essentially the same as for non-interacting atoms. In the tight-binding limit we expect the equilibrium electron density to be essentially the same as for non-interacting atoms. If we denote the latter as  $n_0(\mathbf{r})$ , we can replace  $n(\mathbf{r})$  by  $n_0(\mathbf{r})$  in  $E_{\text{SC}}^{\text{eq}}$  and expect the resulting non-self-consistent total energy  $E_{\text{NSC}}^{\text{eq}}$  to be quite close to the self-consistent total energy for the equilibrium lattice structure:

$$E_{\text{NSC}}^{\text{eq}} \approx E_{\text{SC}}^{\text{eq}}. \quad (\text{A.31})$$

This approach is the basis for using an effective tight-binding model to calculate band structures.

Such a method, however, breaks down when we consider a lattice perturbed by a phonon. In the presence of a lattice distortion, the ionic potential changes to  $V_{\text{ion}}^{\text{dist}} = V_{\text{ion}}^{\text{eq}} + \delta V_{\text{ion}}$  which, in turn, makes the charge-density non-uniform  $n = n_0 + \delta n$ .

The energy of the distorted structure is then

$$\begin{aligned} E_{\text{SC}}^{\text{dist}} &= \sum_i \langle \psi_i | \left( \frac{\mathbf{p}^2}{2m} + V_{\text{ion}}^{\text{dist}}(\mathbf{r}) + \frac{1}{2} \int d^3r' \frac{n(\mathbf{r}')}{|\mathbf{r} - \mathbf{r}'|} \right) | \psi_i \rangle \\ &+ E_{\text{ion-ion}}^{\text{dist}}. \end{aligned} \quad (\text{A.32})$$

Now replacing  $n$  with  $n_0 + \delta n$ , this can be written as

$$E_{\text{SC}}^{\text{dist}} = \sum_i \langle \psi_i | \mathcal{H}^{\text{dist}}[n_0] | \psi_i \rangle + F^{\text{dist}}[n_0] \quad (\text{A.33})$$

$$+ \frac{1}{2} \int d^3r d^3r' \left( \frac{1}{|\mathbf{r} - \mathbf{r}'|} \right) \delta n(\mathbf{r}) \delta n(\mathbf{r}')$$

where  $\mathcal{H}^{\text{dist}}$  and  $F^{\text{dist}}$  are given by  $\mathcal{H}^{\text{eq}}$  and  $F^{\text{eq}}$  defined above with  $V_{\text{ion}}^{\text{eq}}$  and  $E_{\text{ion-ion}}^{\text{eq}}$  replaced by  $V_{\text{ion}}^{\text{dist}}$  and  $E_{\text{ion-ion}}^{\text{dist}}$ . The first two terms on the right of Eq. A.33 can be seen to be the total energy of the distorted structure computed with the non-self-consistent method. We therefore obtain

$$E_{\text{SC}}^{\text{dist}} = E_{\text{NSC}}^{\text{dist}} + \frac{1}{2} \int d^3r d^3r' \left( \frac{1}{|\mathbf{r} - \mathbf{r}'|} \right) \delta n(\mathbf{r}) \delta n(\mathbf{r}'). \quad (\text{A.34})$$

Subtracting Eq. A.31 from this then gives

$$\Delta E_{\text{SC}} = \Delta E_{\text{NSC}} + \frac{1}{2} \int d^3r d^3r' \left( \frac{1}{|\mathbf{r} - \mathbf{r}'|} \right) \delta n(\mathbf{r}) \delta n(\mathbf{r}') \quad (\text{A.35})$$

where  $\Delta E_{\text{SC,NSC}} = E_{\text{SC,NSC}}^{\text{dist}} - E_{\text{SC,NSC}}^{\text{eq}}$ . Rewriting the second term in momentum space gives

$$\Delta E_{\text{SC}} = \Delta E_{\text{NSC}} + \frac{1}{2} \int \frac{d^3q}{(2\pi)^3} V(q) |\delta n_{\mathbf{q}}|^2. \quad (\text{A.36})$$

which then makes it clear that  $\Delta E_{\text{SC}} > \Delta E_{\text{NSC}}$ . So we see that using the a non-self-consistent method to calculate phonon frequencies by the frozen-phonon approximation will underestimate the phonon frequencies. More specifically, in a non-self-consistent method, the Hartree term displayed in Eq. (A.36) is not accounted for. This should be particularly important in the vicinity of a CDW instability, where there will be a larger response of the charge distribution to a lattice distortion.



## A.5 Derivation of Eq. (4.31)

In this Appendix, we will derive Eq. (4.31) by evaluating the integral appearing in Eq. (4.30). To estimate this Coulomb interaction integral, we will take the tight-binding wave function of graphene

$$\psi_{\mathbf{k}\gamma}(\mathbf{r}) = \frac{1}{\sqrt{N}} \sum_n e^{i\mathbf{k}\cdot\mathbf{R}_n} \frac{1}{\sqrt{2}} \left( \gamma \frac{f(\mathbf{k})}{|f(\mathbf{k})|} \phi_{n1}(\mathbf{r}) + \phi_{n2}(\mathbf{r}) \right). \quad (\text{A.37})$$

Now  $\mathbf{k}$  is a two dimensional vector in reciprocal space of the graphene lattice and  $\gamma = \pm 1$  corresponds to the conduction and valence bands. Orbitals centered on the first and second carbon atoms respectively in the  $n$ th unit cell are given by  $\phi_{n1}(\mathbf{r})$  and  $\phi_{n2}(\mathbf{r})$  respectively, and  $f(\mathbf{k})$  is given by  $f(\mathbf{k}) = 1 + e^{-i\mathbf{k}\cdot\mathbf{a}_1} + e^{-i\mathbf{k}\cdot\mathbf{a}_2}$  where  $\mathbf{a}_1$  and  $\mathbf{a}_2$  are the lattice vectors of graphene. For metallic large radius CNTs, the Fermi points correspond to  $\mathbf{K} = \frac{1}{3}(\mathbf{b}_1 - \mathbf{b}_2)$  and  $\mathbf{K}' = \frac{2}{3}(\mathbf{b}_1 - \mathbf{b}_2)$  where  $\mathbf{b}_1$  and  $\mathbf{b}_2$  are the reciprocal lattice vectors corresponding to  $\mathbf{a}_1$  and  $\mathbf{a}_2$ . For these points, we have  $f(\mathbf{K}) = f(\mathbf{K}') = 0$ . However, for the smaller radius CNTs we study, as indicated by the failure of the zone-folding method, the Fermi points are shifted away from  $\mathbf{K}$  and  $\mathbf{K}'$ . We denote the Fermi points of the inner band  $\tau_a$  of the (5,0) CNT by  $\mathbf{k}_{\tau_{a+}} = \mathbf{K} + k_x \hat{\mathbf{x}} - k_y \hat{\mathbf{y}}$  and  $\mathbf{k}_{\tau_{a-}} = \mathbf{K} - k_x \hat{\mathbf{x}} - k_y \hat{\mathbf{y}}$  and for the other inner band  $\tau_b$  by  $\mathbf{k}_{\tau_{b+}} = \mathbf{K}' + k_x \hat{\mathbf{x}} + k_y \hat{\mathbf{y}}$  and  $\mathbf{k}_{\tau_{b-}} = \mathbf{K}' - k_x \hat{\mathbf{x}} + k_y \hat{\mathbf{y}}$  where the  $x$ -direction is still along the CNT axis and the  $y$ -direction is along the perimeter.

For backward scattering, we take  $q \approx 2k_F$ ,  $k \approx -k_F$ ,  $k' \approx k_F$ . Keeping only products of Carbon orbitals centered on the same atom, we obtain

$$\begin{aligned} \psi_{\mathbf{k}+q\tau_a}^*(\mathbf{r})\psi_{\mathbf{k}\tau_a}(\mathbf{r}) &\approx \frac{1}{N} \sum_n e^{-iq\hat{\mathbf{x}}\cdot\mathbf{R}_n} \frac{1}{2} \\ &\times \left( \frac{f^*(\mathbf{k}_{\tau_{a+}})f(\mathbf{k}_{\tau_{a-}})}{|f^*(\mathbf{k}_{\tau_{a+}})f(\mathbf{k}_{\tau_{a-}})|} |\phi_{n1}(\mathbf{r})|^2 \right) \end{aligned} \quad (\text{A.38})$$

$$+ |\phi_{n2}(\mathbf{r})|^2 \Big).$$

Now we make use of the slow variation of  $e^{-iqx}$  compared to the localized orbitals to write

$$\begin{aligned} \psi_{\mathbf{k}+q\tau}^*(\mathbf{r})\psi_{\mathbf{k}\tau}(\mathbf{r}) &\approx e^{-iqx} \frac{1}{N} \sum_n \frac{1}{2} \\ &\times \left( \frac{f^*(\mathbf{k}_{\tau a+})f(\mathbf{k}_{\tau a-})}{|f^*(\mathbf{k}_{\tau a+})f(\mathbf{k}_{\tau a-})|} |\phi_{n1}(\mathbf{r})|^2 \right. \\ &\left. + e^{iq\hat{\mathbf{x}}\cdot\mathbf{t}} |\phi_{n2}(\mathbf{r})|^2 \right) \end{aligned} \quad (\text{A.39})$$

where  $\mathbf{t} = \frac{1}{\sqrt{3}}a\hat{\mathbf{x}}$  is the basis vector for the second Carbon atom in the primitive unit cell. Finally, in evaluating the integral in Eq. (4.30) it is sufficient to replace the functions  $\frac{1}{N} \sum_n |\phi_{n1,2}(\mathbf{r})|^2$  which vary more rapidly than  $V(\mathbf{r})$  by their average values. That is, we substitute

$$\begin{aligned} \psi_{\mathbf{k}+q\tau}^*(\mathbf{r})\psi_{\mathbf{k}\tau}(\mathbf{r}) &\rightarrow \\ \frac{1}{2\pi RL} e^{-iqx} &\frac{1}{2} \left( \frac{f^*(\mathbf{k}_{\tau a+})f(\mathbf{k}_{\tau a-})}{|f^*(\mathbf{k}_{\tau a+})f(\mathbf{k}_{\tau a-})|} + e^{iq\hat{\mathbf{x}}\cdot\mathbf{t}} \right). \end{aligned} \quad (\text{A.40})$$

Using the same approximations for the factor  $\psi_{\mathbf{k}'-q}(\mathbf{r}')\psi_{\mathbf{k}'}(\mathbf{r}')$ , we obtain for the Coulomb interaction

$$V_{q\tau a\tau a} \approx \frac{1}{4} \left| \frac{f^*(\mathbf{k}_{\tau a+})f(\mathbf{k}_{\tau a-})}{|f^*(\mathbf{k}_{\tau a+})f(\mathbf{k}_{\tau a-})|} + e^{iq\hat{\mathbf{x}}\cdot\mathbf{t}} \right|^2 \quad (\text{A.41})$$

$$\begin{aligned} &\times \frac{1}{L^2} \int dx dx' e^{-iq(x-x')} \\ &\times \int_0^{2\pi R} \frac{dy}{2\pi R} \int_0^{2\pi R} \frac{dy'}{2\pi R} V(\mathbf{r} - \mathbf{r}'). \end{aligned} \quad (\text{A.42})$$

We will now evaluate the prefactor in this equation for the inner band of the (5,0) and (6,0) CNTs. Using the calculated Fermi points along with the zone-folding

method, we obtain  $k_x = \pm \frac{0.11}{\sqrt{3}} \frac{2\pi}{a}$  and  $k_y = \frac{1}{15} \frac{2\pi}{a}$  for the (5,0) CNT. From this we obtain

$$\frac{1}{4} \left| \frac{f^*(\mathbf{k}_{\tau_{a+}})f(\mathbf{k}_{\tau_{a-}})}{|f^*(\mathbf{k}_{\tau_{a+}})f(\mathbf{k}_{\tau_{a-}})|} + e^{iq\hat{\mathbf{x}}\cdot\mathbf{t}} \right|^2 = 0.59 \quad (\text{A.43})$$

For the (6,0) CNT the Fermi points are  $k_x = \pm \frac{0.076}{\sqrt{3}} \frac{2\pi}{a}$  and  $k_y = 0$ . This gives

$$\frac{1}{4} \left| \frac{f^*(\mathbf{k}_{\tau_{a+}})f(\mathbf{k}_{\tau_{a-}})}{|f^*(\mathbf{k}_{\tau_{a+}})f(\mathbf{k}_{\tau_{a-}})|} + e^{iq\hat{\mathbf{x}}\cdot\mathbf{t}} \right|^2 = 0.0016 \quad (\text{A.44})$$

which is smaller due to the different symmetry of the wave functions at the Fermi points. These are the values of the prefactor  $\gamma$  appearing in Eq. (4.31).

# Bibliography

- [1] A. A. Abrikosov, L. P. Gorkov, and I. E. Dzyaloshinski. *Methods of Quantum Field Theory in Statistical Physics*. Dover Publications, 1977.
- [2] P. B. Allen. *Phys. Rev. B*, 13:1416, 1976.
- [3] P. B. Allen and B. Mitrovic. In F. Seitz, D. Turnbull, and H. Ehrenreich, editors, *Solid State Physics*, volume 37. Academic Press, New York, 1982.
- [4] E. Altman, E. Demler, and M. Lukin. *Phys. Rev. A*, 70:013603, 2004.
- [5] E. Altman, W. Hofstetter, E. Demler, and M. Lukin. *New Journal of Physics*, 5:113, 2003.
- [6] M. H. Anderson, J. R. Ensher, M. R. Matthews, C. E. Wiemann, and E. A. Cornell. *Science*, 269:198, 1995.
- [7] P. W. Anderson. *Phys. Rev.*, 109:1492, 1958.
- [8] V. P. Antropov, O. Gunnarsson, and O. Jepsen. *Phys. Rev. B*, 46:13647, 1992.
- [9] J. Bardeen. *Rev. Mod. Phys.*, 23:261, 1951.
- [10] C. C. Bardley, C. A. Sackett, J. J. Tollett, and R. G. Hulet. *Phys. Rev. Lett.*, 75:1687, 1995.
- [11] C. Bena, S. Chakravarty, J. Hu, and C. Nayak. *Phys. Rev. B*, 63:134517, 2004.
- [12] L. X. Benedict, V. H. Crespi, S. G. Louie, and M. L. Cohen. *Phys. Rev. B*, 52:14935, 1995.
- [13] L. X. Benedict, S. G. Louie, and M. L. Cohen. *Phys. Rev. B*, 52:8541, 1995.
- [14] P. Blaha, K. Schwarz, G. K. H. Madsen, D. Kvasnicka, and J. Luitz. **WIEN2k**, *An Augmented Plane Wave + Local Orbitals Program for Calculating Crystal Properties*. Karlheinz Schwarz Techn. Universität, Wien Austria, 2001.
- [15] P. Blaha and *et al.* *Comput. Phys. Commun.*, 147:71, 2002.

- [16] X. Blase, L. X. Benedict, E. L. Shirley, and S. G. Louie. *Phys. Rev. Lett.*, 72:1878, 1994.
- [17] I. Bloch. *Nature Physics*, 1:23, 2005.
- [18] N. N. Bogoliubov. *J. Phys. (USSR)*, 11:23, 1947.
- [19] E. Braun, Y. Eichen, U. Sivan, and G. Ben-Yoseph. *Nature*, 391:775–778, 1998.
- [20] K. Byczuk. cond-mat/0206086.
- [21] R. A. Caetano and P. A. Schulz. *Phys. Rev. Lett.*, 95:126601, 2005.
- [22] L. Cai, H. Tabata, and T. Kawai. *Applied Physics Letters*, 77(19):3105–6, 2000.
- [23] L. Capriotti, D. J. Scalapino, and R. D. Sedgewick. *Phys. Rev. B*, 68:014508, 2003.
- [24] L. G. Caron. In Jean-Pierre Farges, editor, *Organic Conductors: Fundamentals and Applications*. Marcel Dekker, New York, 1994.
- [25] A. H. CastroNeto. *Phys. Rev. Lett.*, 86:4382, 2001.
- [26] P. Chen, J. Gu, E. Grandin, Y.-R. Kim, Q. Wang, and D. Branton. *Nano Letters*, 4:2293, 2004.
- [27] P. Cluzel, A. Lebrun, C. Heller, R. Lavery, J. L. Viovy, D. Chatenay, and F. Caron. *Science*, 271:792–794, 1996.
- [28] H. Cohen, C. Nogues, R. Naaman, and D. Porath. *Proc. Natl. Acad. Sci.*, 102:11589, 2005.
- [29] M. L. Cohen. *Science*, 234:549, 1986.
- [30] R. V. Coleman, B. Giambattista, P. K. Hansma, A. Johnson, W. W. McNairy, and C. G. Slough. *Adv. Phys.*, 37:559, 1988.
- [31] M. M. Dacorogna, K. J. Chang, and M. L. Cohen. *Phys. Rev. B*, 32:1853, 1985.
- [32] B. Damski, H. U. Everts, A. Honecker, H. Fehrmann, L. Santos, and M. Lewenstein. *Phys. Rev. Lett.*, 95:060403, 2005.
- [33] K. B. Davis, M.-O. Mewes, M. R. Andrews, N. J. van Druten, D. S. Durfee, D. M. Kurn, and W. Ketterle. *Phys. Rev. Lett.*, 75:3969, 1995.
- [34] P.J. de Pablo, F. Moreno-Herrero, J. Colchero, J.G. Herrero, P. Herrero, A.M. Baro, P. Ordejon, J.M. Soler, and E. Artacho. *Phys. Rev. Lett.*, 85(23):4992–5, 2000.

- [35] C. Dekker and M. A. Ratner. *Physics World*, 14:29, 2001.
- [36] A. DeMartino and R. Egger. *Phys. Rev. B*, 67:235418, 2003.
- [37] D. DeMille. *Phys. Rev. Lett.*, 88:067901, 2002.
- [38] X.-L. Deng, D. Porras, and J. I. Cirac. cond-mat/0509197.
- [39] J. Doyle, B. Friedrich, R. V. Krems, and F. Masnou-Seeuws. *Eur. Phys. J. D*, 31:149, 2004.
- [40] M. S. Dresselhaus and G. Dresselhaus. *Adv. Phys.*, 30:139, 1981.
- [41] L.-M. Duan, E. Demler, and M. Lukin. *Phys. Rev. Lett.*, 91:090402, 2003.
- [42] O. Dubay, G. Kresse, and H. Kuzmany. *Phys. Rev. Lett.*, 88:235506, 2002.
- [43] R. Egger, A. Bachtold, M. Fuhrer, and M. Bockrath. Luttinger liquid behavior in metallic carbon nanotubes. In R. Haug and H. Schoeller, editors, *Interacting Electrons in Nanostructures*. Springer Verlag, 2001.
- [44] R. Egger and A. O. Gogolin. *Eur. Phys. J. B*, 3:281, 1998.
- [45] D. D. Eley and D. I. Spivey. Semiconductivity of organic substances, part 9. nucleic acid in the dry state. *Trans. Faraday Soc.*, 58:411–415, 1961.
- [46] G. M. Eliashberg. *Zh. Eksp. Teor. Fiz. [Sov. Phys. JETP]*, 11:696, 1960.
- [47] M. Elstner, D. Porezag, G. Jungnickel, J. Elsner, M. Haugk, T. Frauenheim, S. Suhai, and G. Seifert. *Phys. Rev. B*, 58(11):7260–8, 1998.
- [48] R. G. Endres, D. L. Cox, and R. R. P. Singh. *Rev. Mod. Phys.*, 76:195, 2004.
- [49] S. Engelsberg and B. B. Varga. *Phys. Rev.*, 136:A1582, 1964.
- [50] H.-W. Fink and C. Schonberger. Electrical conduction through dna molecules. *Nature*, 398(6726):407–10, 1999.
- [51] A. Georges, B. Kotliar, W. Krauth, and M. Rozenberg. *Rev. Mod. Phys.*, 68:13, 1996.
- [52] T. Giamarchi. *Quantum Physics in One Dimension*. Oxford University Press, 2004.
- [53] V. L. Ginzburg and D. A. Kirzhnits, editors. *High Temperature Superconductivity*. The Consultants Bureau, New York, 1982.
- [54] J. Gonzalez. *Phys. Rev. Lett.*, 88:76403, 2002.

- [55] K. Goral, K. Rzazewski, and T. Pfau. *Phys. Rev. A*, 61:051601, 2000.
- [56] K. Goral, L. Santos, and M. Lewenstein. *Phys. Rev. Lett.*, 88:170406, 2002.
- [57] M. Greiner, O. Mandel, T. Esslinger, T. Hansch, and I. Bloch. *Nature*, 415:39, 2002.
- [58] S. Grenier, J. P. Hill, V. Kiryukhin, W. Ku, Y.-J. Kim, K. J. Thomas, S-W. Cheong, Y. Tokura, Y. Tomioka, D. Casa, , and T. Gog. *Phys. Rev. Lett*, 94:047203, 2005.
- [59] G. S. Grest, E. Abrahams, S.-T. Chui, P. A. Lee, and A. Zawadowski. *Phys. Rev. B*, 14:1225, 1976.
- [60] E. P. Gross. *Nuovo Cimento*, 20:454, 1963.
- [61] G. Grüner. *Density Waves in Solids*. Perseus Publishing, 1994.
- [62] O. Gülseren, T. Yildirim, and S. Ciraci. *Phys. Rev. B*, 65:153405, 2002.
- [63] A. J. Heeger. In J. T. Devreese, R. P. Evrard, and V. E. van Doren, editors, *Highly Conducting One-Dimensional Solids*. Plenum Press, New York, 1979.
- [64] T. Heim, T. Melin, D. Deresmes, and D. Vuillaume. *Appl. Phys. Lett.*, 85:2637, 2004.
- [65] T. Hertel and G. Moos. *Phys. Rev. Lett.*, 84:5002, 2000.
- [66] J. E. Hoffman, K. McElroy, D. H. Lee, L. M. Kang, H. Eisaki, S. Uchida, and J. C. Davis. *Science*, 297:1148, 2002.
- [67] P. Hohenberg and W. Kohn. *Phys. Rev.*, 136:B864, 1964.
- [68] C. Howald, H. Eisaki, N. Kaneko, and A. Kapitulnik. *Phys. Rev. B*, 67:014533, 2003.
- [69] K. Huang. *Statistical Mechanics*. John Wiley and Sons, 1987.
- [70] Y. Huang, M. Okada, K. Tanaka, and T. Yamabe. *Solid State Commun.*, 97:303, 1996.
- [71] K. Iguchi. *Int. J. mod. Phys. B*, 18:1845, 2004.
- [72] S. Ijima. *Nature*, 54:56, 1991.
- [73] A. Imambekov, M. Lukin, and E. Demler. *Phys. Rev. A*, 68:063602, 2003.
- [74] T. Inoshita, K. Nakao, and H. Kamimura. *J. Phys. Soc. Jpn.*, 43:1237, 1977.

- [75] S. Inouye, J. Goldwin, M. L. Olsen, C. Ticknor, J. L. Bohn, and D. S. Jin. *Phys. Rev. Lett.*, 93:183201, 2004.
- [76] A. Isacsson, M.-C. Cha, K. Sengupta, and S. M. Girvin. *Phys. Rev. B*, 72:184507, 2005.
- [77] D. Jaksch, C. Bruder, J. I. Cirac, C. W. Gardiner, and P. Zoller. *Phys. Rev. Lett.*, 81:3108, 1998.
- [78] R. A. Jishi, L. Venkataraman, M. S. Dresselhaus, and G. Dresselhaus. *Chem. Phys. Lett.*, 209:77, 1993.
- [79] M. D. Johannes, I. I. Mazin, and C. A. Howells. cond-mat/0510390.
- [80] K. Kamide, T. Kimura, M. Nishida, and S. Kurihara. cond-mat/0301115.
- [81] K. Kanamitsu and S. Saito. *J. Phys. Soc. Jpn.*, 71:483, 2002.
- [82] A.Y. Kasumov, R. Deblock, M. Kociak, B. Reulet, H. Bouchiat, I.I. Khodos, Y.B. Gorbatov, V.T. Volkov, C. Journet, , and M. Burghard. *Science*, 284:1508, 1999.
- [83] A.Yu. Kasumov, M. Kociak, S. Gueron, B. Reulet, V.T. Volkov, D.V. Klinov, and H. Bouchiat. *Science*, 291(5502):280–2, 2001.
- [84] E. Kaxiras. *Atomic and Electronic Structure of Solids*. Cambridge University Press, 2003.
- [85] T. Kinoshita, T. R. Wenger, and D. S. Weiss. *Science*, 305:1125, 2004.
- [86] M. Kociak, A. Y. Kasumov, S. Guéron, B. Reulet, I. I. Khodos, Y. B. Gorbatov, V. T. Volkov, L. Vaccarini, and H. Bouchiat. *Phys. Rev. Lett.*, 86:2416, 2001.
- [87] W. Kohn. *Phys. Rev. Lett.*, 2:393, 1959.
- [88] W. Kohn and L. Sham. *Phys. Rev.*, 140:A1133, 1965.
- [89] G. Kotliar, S. Y. Savrasov, K. Haule, V. S. Oudovenko, O. Parcollet, and C. A. Marianetti. cond-mat/0511085.
- [90] Wei Ku, W. E. Pickett, and R.T. Scalettar. to be published.
- [91] Wei Ku, H. Rosner, W. E. Pickett, and R. T. Scalettar. *Phys. Rev. Lett*, 89:167204, 2002.
- [92] A. Kuklov, N. Prokof'ev, and B. Svistunov. *Phys. Rev. Lett.*, 92:050402, 2004.
- [93] P. K. Lam, M. M. Dacorogna, and M. L. Cohen. *Phys. Rev. B*, 34:5065, 1986.



- [94] J. S. Langer and V. Ambegaokar. *Phys. Rev.*, 164:498, 1967.
- [95] A. Lanzara, P. V Bogdanov, X. J. Zhou, S. A. Kellar, D. L. Feng, E. D. Lu, Y. Yoshida, H. Eisaki, A. Fujimori, K. Kishio, J. I. Shimoyama, T. Noda, S. Uchida, Z. Hussain, and Z. X. Shen. *Nature*, 412:510, 2001.
- [96] Anne Lebrun and Richard Lavery. Modelling extreme stretching of dna. *Nucleic Acids Research*, 24(12):2260–2267, 1996.
- [97] K. Levin, D. L. Mills, and S. L. Cunningham. *Phys. Rev. B*, 10:3821, 1974.
- [98] Z. M. Li, Z. K. Tang, H. J. Liu, N. Wang, C. T. Chan, R. Saito, S. Okada, G. D. Li, J. S. Chen, N. Nagasawa, and S. Tsuda. *Phys. Rev. Lett.*, 87:127401, 2001.
- [99] H. J. Liu and C. T. Chan. *Phys. Rev. B*, 66:115416, 2002.
- [100] R. Liu, C. G. Olson, W. C. Tonjes, and R. F. Frindt. *Phys. Rev. Lett.*, 80:5762, 1998.
- [101] R. Liu, W. C. Tonjes, V. A. Greanya, C. G. Olson, and R. F. Frindt. *Phys. Rev. B*, 61:5212, 2000.
- [102] D. Loss and T. Martin. *Phys. Rev. B*, 50:12160, 1994.
- [103] J. M. Luttinger and L. Tisza. *Phys. Rev.*, 70:954, 1946.
- [104] M. Machón, S. Reich, C. Thomsen, D. Sánchez-Portal, and P. Ordejón. *Phys. Rev. B*, 66:155410, 2002.
- [105] O. Mandel, M. Greiner, A. Widera, T. Rom, T. Hansch, and I. Bloch. *Nature*, 425:937, 2003.
- [106] P. Maragakis, R. L. Barnett, E. Kaxiras, M. Elstner, and T. Frauenheim. *Phys. Rev. B*, 66:241104(R), 2002.
- [107] D. E. McCumber and B. I. Halperin. *Phys. Rev. B*, 1:1054, 1970.
- [108] K. McElroy, R. W. Simmonds, J. E. Hoffman, D. H. Lee, J. Orenstein, H. Eisaki, S. Uchida, and J. C. Davis. *Nature*, 422:592, 2003.
- [109] W. L. McMillan. *Phys. Rev.*, 167:1967, 1967.
- [110] M. J. Mehl and D. A. Papaconstantopoulos. *Phys. Rev. B*, 54:4519, 1996.
- [111] A. Micheli, G.K. Brennen, and P. Zoller. quant-ph/0512222.
- [112] A. B. Migdal. *Zh. Eksp. Teor. Fiz. [Sov. Phys. JETP]*, 34:1438, 1958.

- [113] J. W. Mintmire, B. I. Dunlap, and C. T. White. *Phys. Rev. Lett.*, 68:631, 1992.
- [114] R. Moessner and S. L. Sondhi. *Phys. Rev. B*, 68:054405, 2003.
- [115] D. E. Moncton, J. D. Axe, and F. J. DiSalvo. *Phys. Rev. B*, 16:801, 1977.
- [116] H. J. Monkhorst and J. D. Pack. *Phys. Rev. B*, 13:5188, 1976.
- [117] M. G. Moore and H. R. Sadeghpour. *Phys. Rev. A*, 67:041603, 2003.
- [118] A.F. Morpurgo, J. Kong, C.M. Marcus, and H. Dai. *Science*, 286:263, 1999.
- [119] C. J. Murphy, M. R. Arkin, Y. Jenkins, N. D. Ghatlia, S. H. Bossmann, N. J. Turro, and J. K. Barton. *Science*, 262:1025–1029, 1993.
- [120] B. Paredes, A. Widera, V. Murg, O. Mandel, S. Fölling, I. Cirac, G. V. Shlyapnikov, T. Hansch, and I. Bloch. *Nature*, 429:277, 2004.
- [121] G. B. Partridge, W. Li, R. I. Kamar, Y. Liao, and R. G. Hulet. *Science*, 311:503, 2006.
- [122] M. C. Payne, M. P. Teter, D.C. Allan, T. A. Arias, and J. D. Joannopoulos. *Rev. Mod. Phys.*, 64:1045, 1992.
- [123] R. E. Peierls. *Quantum Theory of Solids*. Oxford University, 1955.
- [124] L. M. Peng, Z. L. Zhang, Z. Q. Xue, Q. D. Wu, Z. N. Gu, and D. G. Pettifor. *Phys. Rev. Lett.*, 85:3249, 2000.
- [125] C. J. Pethick and H. Smith. *Bose-Einstein Condensation in Dilute Gases*. Cambridge University Press, 2002.
- [126] L. P. Pitaevskii. *Zh. Eksp. Teor. Fiz.*, 40:646, 1961.
- [127] D. Podolsky, E. Demler, K. Damle, and B. I. Halperin. *Phys. Rev. B*, 67:094514, 2003.
- [128] A. Polkovnikov, S. Sachdev, and M. Vojta. *Physica C*, 388-389:19, 2003.
- [129] D. Porath, A. Bezryadin, S. De Vries, and C. Dekker. *Nature*, 403(6770):635–8, 2000.
- [130] D. Rainer. *Prog. in Low Temp. Phys.*, 10:371, 1986.
- [131] C. A. Regal, M. Greiner, and D. S. Jin. *Phys. Rev. Lett.*, 92:040403, 2004.
- [132] T. M. Rice and G. K. Scott. *Phys. Rev. Lett.*, 35:120, 1975.

- [133] K. Rossnagel, O. Seifarth, L. Kipp, M. Skibowski, D. Voss, P. Kruger, A. Mazur, and J. Pollmann. *Phys. Rev. B*, 64:235119, 2001.
- [134] J. M. Sage, S. Sainis, T. Bergeman, and D. DeMille. *Phys. Rev. Lett.*, 94:203001, 2005.
- [135] R. Saito, G. Dresselhaus, and M. S. Dresselhaus. *Physical Properties of Carbon Nanotubes*. Imperial College Press, London, 1998.
- [136] D. Sánchez-Portal, E. Artacho, J. M. Soler, A. Rubio, and P. Ordejon. *Phys. Rev. B*, 59:12678, 1999.
- [137] L. Santos, G. V. Shlyapnikov, P. Zoller, and M. Lewenstein. *Phys. Rev. Lett.*, 85:1791, 2000.
- [138] J. A. Sauer. *Phys. Rev.*, 57:142, 1940.
- [139] J. R. Schrieffer. *Theory of Superconductivity*. Perseus Books, 1963.
- [140] A. Sédéki, L. G. Caron, and C. Bourbonnais. *Phys. Rev. B*, 62:6975, 2000.
- [141] A. Sédéki, L. G. Caron, and C. Bourbonnais. *Phys. Rev. B*, 65:140515, 2002.
- [142] C. G. Slough, W. W. McNairy, R. V. Coleman, B. Drake, and P. K. Hansma. *Phys. Rev. B*, 34:994, 1986.
- [143] S. B. Smith, Y. J. Cui, and C. Bustamante. *Science*, 271:795–799, 1996.
- [144] D. Stamper-Kurn and W. Ketterle. cond-mat/0005001.
- [145] C. A. Stan, M. W. Zwierlein, C. H. Schunck, S. M. F. Raupach, and W. Ketterle. *Phys. Rev. Lett.*, 93:143001, 2004.
- [146] A. J. Storm, J. van Noort, S. de Vries, and C. Dekker. *Appl. Phys. Lett.*, 79:3881, 2001.
- [147] Th. Straub, Th. Finteis, R. Claessen, P. Steiner, S. Hufner, P. Blaha, C. S. Oglesby, and E. Bucher. *Phys. Rev. Lett.*, 82:4504, 1999.
- [148] T. R. Strick, J. F. Allemand, D. Bensimon, and V. Croquette. *Annu. Rev. Biophys. Biomolec. Struct.*, 29:523–543, 2000.
- [149] J. Stuhler, A. Griesmaier, T. Koch, M. Fattori, T. Pfau, S. Giovanazzi, P. Pedri, and L. Santos. *Phys. Rev. Lett.*, 95:150406, 2005.
- [150] G. Sun, J. Kürti, M. Kertesz, and R. Baughman. *J. Phys. Chem. B*, 107:6924, 2003.

- [151] I. Takesue, J. Haruyama, N. Kobayashi, S. Chiashi, S. Maruyama, T. Sugai, and H. Shinohara. *Phys. Rev. Lett.*, 96:057001, 2006.
- [152] Z. Tang, L. Zhang, N. Wang, X. Zhang, G. Wen, G. Li, J. Wang, C. Chan, and P. Sheng. *Science*, 292:2462, 2001.
- [153] D. J. Thouless. *J. Phys. C*, 5:77, 1972.
- [154] W. C. Tonjes, V. A. Greanya, R. Liu, C. G. Olson, and P. Molinie. *Phys. Rev. B*, 63:235101, 2001.
- [155] P. Tran, B. Alavi, and G. Gruner. *Phys. Rev. Lett.*, 85(7):1564–7, 2000.
- [156] B. Uchoa, G. G. Cabrera, and A. H. Castro Neto. *Phys. Rev. B*, 71:184509, 2005.
- [157] T. Valla, A. V. Fedorov, P. D. Johnson, P. A. Glans, C. McGuinness, K. E. Smith, E. Y. Andrei, and H. Berger. *Phys. Rev. Lett.*, 92:086401, 2004.
- [158] T. Valla, A. V. Fedorov, P. D. Johnson, J. Xue, K. E. Smith, and F. J. DiSalvo. *Phys. Rev. Lett.*, 85:4759, 2000.
- [159] J. Voint, L. Perfetti, F. Zwick, H. Berger, G. Margaritondo, G. Grüner, H. Hochst, and M. Grioni. *Science*, 290:501, 2000.
- [160] J. Voit and H. J. Schulz. *Phys. Rev. B*, 36:968, 1987.
- [161] J. Voit and H. J. Schulz. *Phys. Rev. B*, 37:10068, 1988.
- [162] C. Wang, B. Giambattista, C. G. Slough, and R. V. Coleman. *Phys. Rev. B*, 42:8890, 1990.
- [163] J. D. Watson and F. H. C. Crick. *Nature*, 171:737, 1953.
- [164] G. Wentzel. *Phys. Rev.*, 83:168, 1951.
- [165] J. A. Wilson. *Phys. Rev. B*, 17:3880, 1978.
- [166] J. A. Wilson, F. J. Di Salvo, and S. Mahajan. *Phys. Rev. Lett.*, 32:882, 1974.
- [167] R. L. Withers and J. A. Wilson. *J. Phys. C*, 19:4809, 1986.
- [168] Y. Yamada. *Int. J. Mod. Phys. B*, 18:1697, 2004.
- [169] S. Yi and L. You. *Phys. Rev. Lett.*, 61:041604, 2000.
- [170] S. Yi and L. You. *Phys. Rev. Lett.*, 92:193201, 2004.

- 
- [171] M. T. Yin and M. L. Cohen. *Phys. Rev. B*, 26:5668, 1982.
- [172] T. Yokoya, T. Kiss, A. Chainani, S. Shin, M. Nohara, and H. Takagi. *Science*, 294:2518, 2001.
- [173] Y. Zhang, R. H. Austin, J. Kraeft, E. C. Cox, and N. P. Ong. *Phys. Rev. Lett.*, 89:198102, 2002.
- [174] V. Zólyomi and J. Kúrti. *Phys. Rev. B*, 70:085403–1, 2004.
- [175] M. W. Zwierlein, A. Schirotzek, C. H. Schunck, and W. Ketterle. *Science*, 311:492, 2006.